Effect of impurity doping and local structural disorder on the martensitic transformation in shape memory alloys

A Thesis submitted in partial fulfillment for the Degree of

DOCTOR OF PHILOSOPHY

in the School of Physical and Applied Sciences
Goa University

By

Rukma G. Nevgi
School of Physical and Applied Sciences
Goa University
Goa

December *2021*

DECLARATION

I, Rukma G. Nevgi hereby declare that this thesis represents work which has been carried out by me and that it has not been submitted, either in part or full, to any other University or Institution for the award of any research degree.

Place: Taleigao Plateau.
Date : -12-2021 Rukma G. Nevgi

CERTIFICATE

I hereby certify that the work was carried out under my supervision and may be placed for evaluation.

Prof. K. R. Priolkar
School of Physical and Applied Sciences

Acknowledgment

First and foremost, I would like to thank my esteemed supervisor, Prof K. R. Priolkar for his guidance, assistance and tutelage during the course of my PhD work. His immense knowledge and plentiful experience have encouraged me all along my academic research life. It was a wonderful experience working under his supervision and I am extremely grateful for giving me this opportunity.

A very special thanks to Dr Lara Righi for training me in her expertise and providing me the facilities to carry out diffraction experiments. I am deeply indebted to her generous hospitality during my six months stay in Parma - Italy.

My sincere gratitude to Prof Mehmet Acet, Dr. Massimo Solzi, and Dr. Francesco Cugini, for their collaboration in magnetization measurements and for their insightful comments and suggestions. I am very much thankful to Dr. Fabio Orlandi for carrying out neutron diffraction experiments and assisting me in performing magnetic refinement. I am deeply grateful to Prof A. K. Nigam and Dr. Elaine T. Dias for their experimental cooperation at every stage of this research work.

For assistance at XAFS beamlines, I extend my sincere thanks to Dr. Edmund Welter and Dr. Ruidy Nemausat at P65, PETRA III Synchrotron source, DESY - Hamburg; and Dr. Giuliana Aquilanti and Dr. Simone Pollastri at Elettra Synchrotron source. Further, I am grateful to Dr. Gangadhar Das for his help in carrying experiments at Indian beamline, Photon factory, KEK.

I very much acknowledge the funding received from Science and Engineering Board, Govt. of India and Council of Scientific and Industrial Research, Govt. of India (SRF-Direct) during the course of my PhD along with MAECI, Govt. of Italy amid my stay in Parma. A generous financial support from Department of Science and Technology, Govt. of India for travel under DST-DESY, Indo-Japan and Indo-Italy Programme of co-operation is greatly appreciated.

I am thankful to PETRA III Synchrotron source – DESY, Hamburg - Germany; XAFS beamline – Elletra, Italy; and Photon factory – KEK, Japan for providing us the beamline facility to carry out experiments.

I express my sincere gratitude to Goa University for allowing me to perform research work. Entire teaching staff of the School of Physical and Applied Sciences in particular, the members of the DRC committee, Prof P. R. Sarode and Prof R. V. Pai are thanked for their guidance and resourceful suggestions. Further, I am thankful to all the non-teaching staff for their assistance during the course of this work.

I thank all the fellow research students of the School of Physical and Applied Sciences for their support and the amazing times shared.

Last, but not the least, my warm and heartfelt thanks to my family members for their moral support and constant encouragement without which this thesis would not have been possible.

Dedicated to, my father

Late Gurudas Ramchandra Nevgi

Contents

List of Tables

List of Figures

Chapter 1

Introduction

1.1 Ferroic Materials

Ferroic crystals are those crystals that undergo at least one phase transition involving a change in the directional symmetry. The materials exhibiting ferromagnetic, ferroelectric, and ferroelastic properties are coined as primary ferroics and are generally termed as 'ferroic materials'. A crystal possessing two or more of these properties is called a multiferroic. These materials display various common features including the existence of domain states (different orientation states in crystal) which is a direct consequence of spontaneous symmetry breaking and the resultant hysteretic behaviour. The crystals displaying ferromagnetic behaviour encounter spontaneous magnetization and the associated domain structure and hysteresis (Fig. 1.1). The electric analogue of ferromagnetism is ferroelectricity which is seen in crystals possessing spontaneous polarization whose direction can be reversed by applying strong electric field. Likewise, the mechanical or the elastic analogue is the property called ferroelasticity. The ferroelastic materials acquire spontaneous strain and the concomitant domain states while hysteresis is observed when directional stress is applied to the bulk spontaneous strain.[1–3]

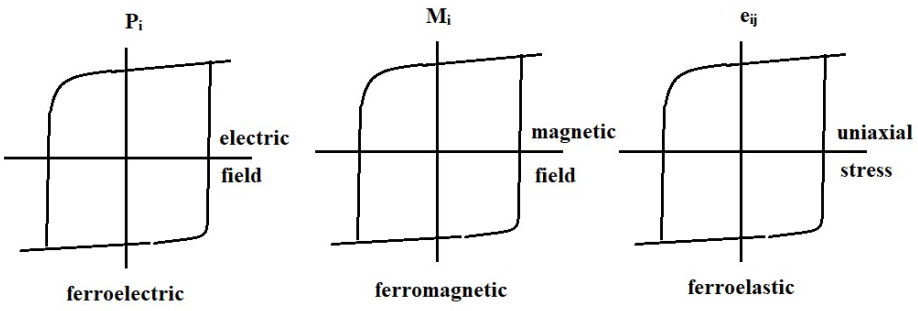

Figure 1.1: Hysteresis exhibited by primary ferroic materials. Typical hysteresis curves are seen for a ferroelectric, a ferromagnetic, and a ferroelastic material.[1]

1.1.1 Phase transition

Ferroic phase transitions can be first or second order depending upon the applied external fields. First order phase transition involves a discontinuous jump in properties; for example, a sudden development of polarization when a ferroelectric material is cooled down across its Curie temperature.[6] Nonetheless, in certain cases, the nature of the transition can be changed from discontinuous (first order) to continuous (second order) by applying an external field that is conjugate to the order parameter that governs the transition; such as an electric or a magnetic fields in ferroelectrics[7] and ferromagnetics respectively.

A phase transition is identified by a change in certain symmetry gauged by an order parameter.[8] The order parameter is zero above the transition and attains a non-zero value below the phase transition, which can be modeled at the mesoscopic level by expressing the Landau free energy as a polynomial expansion.[9]

Assume x to be the order parameter that differentiates between the disordered and

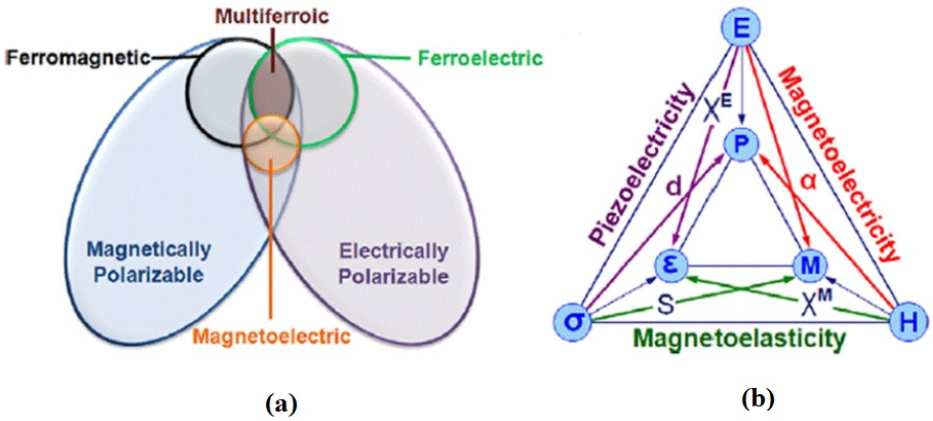

Figure 1.2: (a) Interrelation between magnetic, ferroelectric, multiferroic and magnetoelectric materials. (b) Illustrates different types of coupling present in materials.[4]

the ordered phase such that,

$$x = \begin{cases} \sim (1-t)^{\beta} & t < 1 \quad \text{viz} \quad T < T_C \\ 0 & t > 1 \quad \text{viz} \quad T > T_C \end{cases}, \quad t = \frac{T}{T_C}, \tag{1.1}$$

where T_C is the transition temperature and β is the critical exponent corresponding to the scaling of various observables close to a phase transition.

The Landau model assumes free energy to be function of temperature T, pressure P, an external field y and order parameter x such that

$$G = G(T, P, y; x) \tag{1.2}$$

From the Principle of minimum Gibbs energy, $G(T, P, y; x)$ is minimum for a irreversible process when T and P are constant. Therefore, the thermodynamic state is resolved by minimizing $G(T, P, y; x)$ with respect to x, the order parameter.

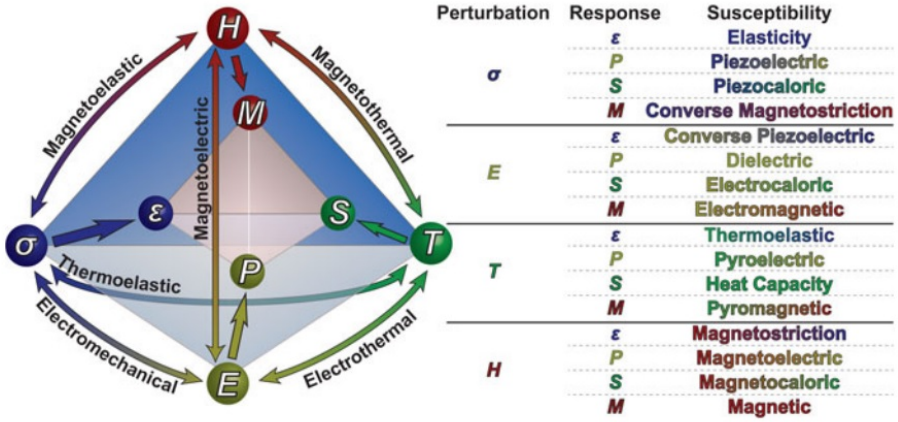

Figure 1.3: Various susceptibilities exhibited by multi-ferroic materials as seen by the adapted Heckmann diagram.[5]

Expanding free energy with respect to the order parameter x at constant P,

$$G(T, y; x) = G_0(T, y) - yx + ax^2 + bx^4 + \dots \tag{1.3}$$

Eqn.1.3 describes the Ginzburg-Landau functional. The temperature, pressure or field derivatives of the free energy present the thermodynamic information about the phase transition wherein the free energy should remain invariant under the relevant symmetry operation of the crystal/material. The domain walls and microstructure is studied by expressing the free energy as the square of the gradient of order parameter called as the Ginzburg term. The Ginzburg-Landau like free energies are also attributed to phase field models in materials science.[10]

Ferroic crystals have two or more orientation states of a physical property or an order parameter related to the same energy and can be switched by applying an external parameter like electric field, magnetic field or stress based on the ferroic property.[1,11] Apart

from the existence of domain structure, the ferroic materials also exhibit some important features in the vicinity of phase transition which include achievement of the high value certain response functions and the large temperature dependence of certain macroscopic properties. These properties form the basis of a variety of device applications in these materials. Also, the booming interest is due to the ability of ferroic and multi-ferroic materials to exhibit spontaneous polarization coupled to mechanical and thermal responses as shown in Fig. 1.2. This involves a change in symmetry as a result of first order transition as seen in materials related to energy conversion technologies exhibiting different caloric effects (Fig. 1.3), smart materials exhibiting large magnetic field induced strains, superelasticity, etc.

1.1.2 Order-disorder transition and ergodicity breaking

The order-disorder transformation of a liquid phase into a crystalline solid below its freezing temperature is driven by the thermodynamic requirement of reducing the entropy in the corresponding thermodynamic potential of the system. The third law of thermodynamics requires all matter to assume a long range ordered form at low temperature to approach a zero-entropy state.[12] Nonetheless, due to the complex nature of the interatomic interactions, some liquids do not crystallize. For instance, the heterogenous nucleation during cooling from the liquid to solid phase in a multi-atom metallic material can be reduced by influencing the strain rates thereby modifying the viscosity.[13,14] This gives rise to non-crystalline materials with convoluted potential energy landscape affecting their elastic properties.[15]

Glass is a frozen disordered metastable state, which occurs when a high temperature dynamically disordered state fails to attain a thermodynamically ordered state. The glass transition occurs due to slowing down of kinetics, i.e. the relaxation time essential for the system to transit from one state to another dramatically increases to an experimentally unattainable time scale[16–19] resulting in the freezing of the system into a certain metastable state. This slowing down process challenges the basic assumption of statistical physics, the fundamental 'hypothesis of ergodicity'. According to this, a system can attain all its possible states on the experimental time scale.[20,21] This statement becomes invalid in a frozen glass state. The loss of ergodicity necessitates a new archetype beyond equilibrium statistical mechanics and has attracted much interest in condensed matter physics for decades.[22]

1.2 Ferroic glass

Ferroic materials undergo disorder-order phase transitions exhibiting long range ordering of magnetic moment in ferromagnets, electric dipole in ferroelectrics, and lattice strain in ferroelastics below critical temperature T_C. Ferroic glass originates from a gradual freezing process of the disordered ferroic state which appears because of the frustration in the ferroic property such as magnetization, polarization, or strain, due to quenched-in (frozen) disorder or defects.[24] This aspect characterizes a relaxor ferroelectric to be a polar glass, a cluster-spin glass as a ferromagnetic glass, and a low-anisotropy martensite and shape memory alloy, a strain glass. A ferroic glass is associated with a precursor phenomenon

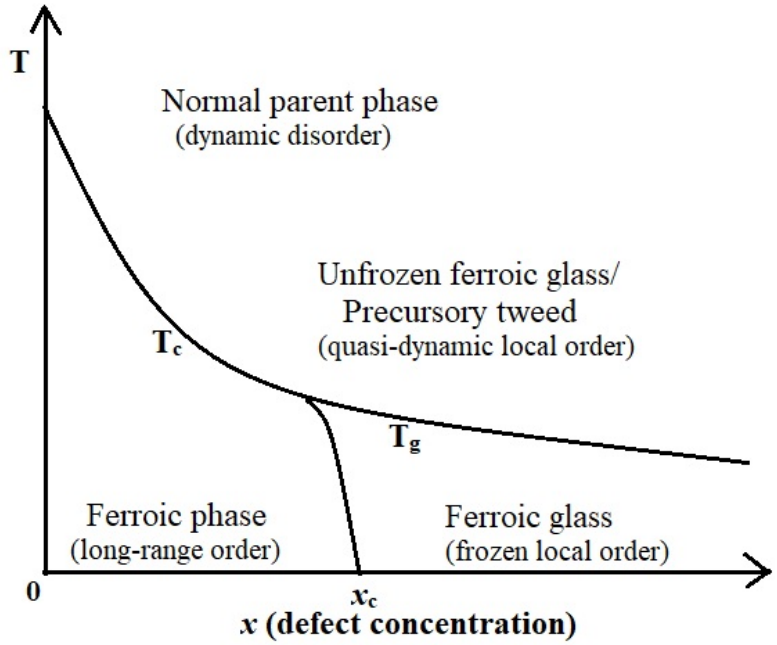

Figure 1.4: Generic phase diagram depicting a crossover from a ferroic transition to a ferroic glass transition as seen in a defect-containing ferroic system at a critical defect concentration x_c. T_C and T_g are the transition temperatures of normal ferroic transition and glass transition respectively.[23]

termed ferroic tweed.[25,26] Such precursor structures are noticed in ferroelectrics, with modulations in the polarization, and in magnetoelastic materials with modulations in the magnetization and/or the strain.[27,28] However, a ferroic tweed needs a small amount of disorder while maintaining the symmetry of the parent phase. In contrast, the ferroic glass requires a strong disorder and transpires in the low symmetry product phase. It has been observed that the ferroic glass appears below a critical anisotropy and above a critical defect density. Usually, there is a distribution of 'droplets' of nanodomains in the glassy materials due to which there is no strong enough anisotropy to create directional domains. This results in phase separated domains as seen in a relaxor ferroelectric or a strain glass.

1.2.1 Characteristics of ferroic glass transition

In a first order thermodynamic transition, there is a change in the average structure due to the formation of long-range order (in atomic arrangement, spin, lattice strain, etc) at a critical temperature in a discontinuous manner. This corresponds to a latent heat or heat capacity peak in thermal measurements which is absent in a glass transition due to suppression of long range order. A glassy transition occurs due to slowing down of the dynamics[13] eventually transforming into a frozen disordered state without a change in average structure. The experimental measurements carried out in identifying a glass are based on the detection of its drastic slowing-down of dynamics with the lowering of temperature. Some of the measurements carried out to confirm the presence of ferroic glasses are listed below.[24]

1. A frequency dependence of AC modulus/loss anomaly at glass transition temperature T_g following Vogel-Fulcher law:

   One of the interesting properties featured in a glass transition that is not seen in a thermodynamic disorder-order transition is the existence of a frequency-dependent anomaly in a relevant dynamic property at glass transition temperature T_g following a Vogel-Fulcher relation. In ferroic glasses, the frequency-dependent anomaly is in the dielectric permittivity of a ferroelectric relaxor (freezing of local electric dipoles),[29] AC magnetic susceptibility of a cluster spin glass (freezing of magnetic moments)[30] and AC storage modulus/loss of a strain glass

(freezing of lattice strain).[31] The Vogel-Fulcher relation is given by the equation, $\omega = \omega_0 \exp[-E_a/k_B(T_g - T_0)]$. Here, T_g is the peak/dip temperature at frequency ω, T_0 is T_g at 0 Hz, or the ideal freezing temperature, E_a is the activation energy and k_B, the Boltzmann constant.

2. Non-ergodic behaviour or history dependence of physical properties in ZFC/FC (zero field cooled/field cooled) experiment:

   The slowing down mechanism in a glass transition is characterized by the ergodicity breaking or history dependence of physical properties in the glassy state. In ferroic glasses, these physical properties are polarization (in ferroelectric relaxor), magnetization (in cluster-spin glass) and strain (in strain glass).[29–31] The history dependence is detected through ZFC/FC experiment wherein the system is cooled below T_g without applying the corresponding field and the warming curve is recorded in the field to obtain ZFC data. Likewise, FC curve is recorded by cooling the system in field. The system is said to be non-ergodic if there is a deviation in the ZFC and FC curves below T_g proving the glassy transition. Generally, at T > T_g, even though the system is said to be ergodic, deviation begins slightly above T_g indicating the onset of ergodicity breaking. Experiments have shown that the three ferroic glasses exhibit similar behaviour in their corresponding AC and DC properties.

3. Invariance of the average structure during glass transition:

As discussed in the previous section, a glass transition is characterized by freezing of a certain disorder and hence the long range order or average structure remains unchanged during the transition. This is in contrast to the normal thermodynamic transition wherein the change in the average structure is inevitable.

4. Presence of local or short-range order in the glassy state:

   Even though the average structure remains invariant, the local order in the order parameter of the transition exists in a glassy state in the form of nano-size domains. These nano-size domains continuously grow and are eventually frozen below T_g with a complete absence in long range ordering. Due to this, the evolutions of nano-size domains is not compatible with any thermodynamic transition.

1.3 Martensitic transformation

A martensitic transformation is a first-order solid-state structural transformation that does not occur by diffusion of atoms but by a shear lattice distortion. It can be induced by the application of external stress or by lowering the temperature. Normally, the transformation is adiabatic, athermal, displays hysteresis, and shows a lattice correspondence between the parent and product structures.[32] During the transformation, the net macroscopic distortion of the crystal remain invariant, which means, the plane between the parent and the martensite phase is a plane of zero average distortion. The invariant strain plane is considered as the superposition of a lattice (Bain) strain, a lattice-invariant shear, a rotation, and a dilation.[33,34] The martensite units exhibit different orientation di-

rections or variants formed from parent crystal arranged in self accommodating groups in such a way that the total macroscopic strains are minimized. The assembly of martensitic variants appear in two forms. One is 'twinned martensite' which constitutes a combination of "self-accommodated" martensite variants while the second one exhibits a specific variant as dominant, termed as the 'detwinned martensite'.

1.4 Shape Memory alloys

The invention of martensite in steel by Adolf Martens in the 1890s lead to the eventual discovery of Shape Memory Alloys (SMAs) when the martensitic transformation was a widely studied phenomenon in metallurgy. The discovery of NiTi alloys lead to the breakthrough for engineering applications mainly because of the shape recovery capability termed as 'Shape Memory Effect' in addition to good mechanical properties.[35] NiTi, also labeled as Nitinol spearheaded active research interest into shape memory alloys as investigations of the effect of heat treatment, composition and microstructure began during this period. Improvement in the functional properties was carried out by the addition of third alloying elements to the existing NiTi and development of other low cost shape memory materials were employed with higher transition temperatures, improved fatigue life suitable for a wide variety of engineering applications particularly in aerospace and medical field.[36] In recent years, alloys exhibiting shape change in the presence of magnetic field have been investigated called the Magnetic Shape Memory alloys (MSMAs), first observed in Heusler alloy Ni_2MnGa.[37,38] These alloys are explored as strong candidates for

high frequency actuation devices due to their large strains and high actuation frequencies and also as magnetic refrigerants.[39–41]

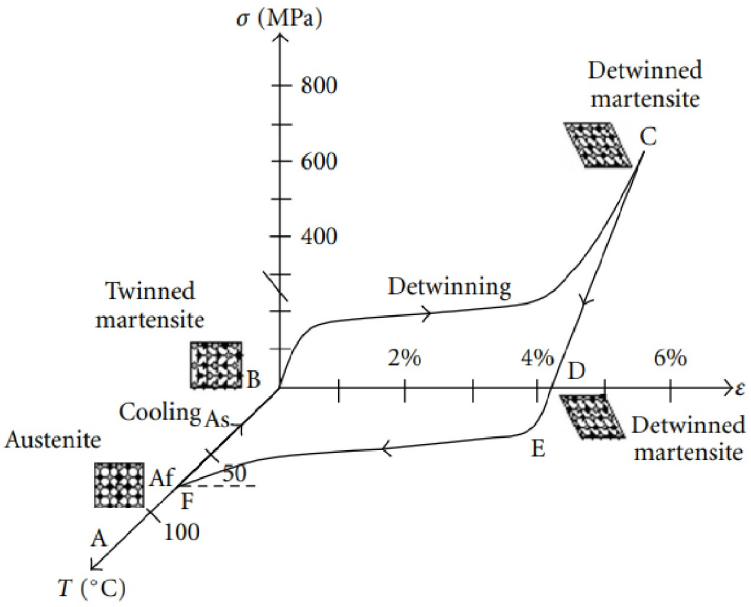

Figure 1.5: Schematic diagram displaying the shape memory effect for a NiTi SMA.[36]

The unique behaviour of SMAs is manifested in their ability to undergo a reversible phase transformation from austenite to martensite and vise versa. The thermochemical loading path in a combined stress-strain-temperature space for a typical NiTi specimen is presented in Fig. 1.5. The uniaxial stress on the alloy due to an applied load is given by σ while the change in the length of alloy in the direction of the applied load normalized by the original length is represented by strain ε. In the stress-free cooling from the parent austenitic phase (point A), the alloy attains a twinned martensitic state (point B). Stress is applied to the twinned martensite and once the stress level exceeds the start stress (σ_s), the detwinning process begins due to the growth of certain favorably oriented

martensitic variant to achieve detwinned martensite (point C). Next, the alloy is elastically unloaded from C to D wherein the detwinned martensitic state is retained. A reverse transformation is commenced upon heating in a stress-free environment at austenitic start temperature A_s (D to E), which is completed at austenitic finish temperature A_f above which parent austenite is regained. The stain recovered during the whole transformation process is called the transformation strain ε^t and the process is termed as the shape memory effect.[42,43]

1.5 Glassy martensite : Strain glass

As mentioned in section 1.1.2, all disorder-order transitions in nature are driven by the thermodynamic requirement of reducing the entropy which stipulates that all matter has to take a long-range ordered form at low temperature. The three ferroic transitions, ferromagnetic, ferroelectric, and ferroelastic/martensitic transition are all characterized by long range ordering of a certain order parameter such as magnetic moment, polarization, and lattice strain respectively. The corresponding high temperature phases of these transitions are featured by a dynamically disordered configuration in the magnetic moment, electric dipole, and unit cell distortions termed as spin liquid, dipole liquid, and strain liquid respectively.

In contrast to the disorder-order transitions, there exist glass transitions described by the freezing of dynamically disordered state into a statistically disordered state of local order only.[13] Generally, the glass transition is seen when the long-range ordering

is suppressed due to doping of sufficient point defects or inhomogeneity into the system exhibiting disorder-order transition. In ferroic materials, this is observed in cluster spin glass by doping non-magnetic defects into a ferromagnetic system like in ferrite,[44] a relaxor is formed by doping point defects in the ferroelectric system (e.g. $PbTiO_3$ / $BaTiO_3$)[45] and a strain glass is witnessed due to impurity addition in a ferroelastic/martensitic system.[46]

The strain glass transition is therefore a transformation from a dynamically disordered lattice strain state into a frozen disordered strain state. In the past, two theoretical studies suggested premartensitic tweed as strain glass.[47–49] A premartensitic tweed is a precursor effect that appears before martensitic transition.[50] However, the existence of a frozen strain state is not confirmed in the tweed temperature region.[51] The strain glass transition was first reported in Ni-rich NiTi shape memory alloys $Ni_{50+x}Ti_{50-x}$.[46] The system undergoes a martensitic transition in lower Ni doping level ($0 \leq x < 1.2$) and when the critical dopant concentration exceeds x = 1.5, it transits into a glassy state down to 0 K. The strain glassy state consists of non-martensitic nano sized strain domains which display characteristics signatures of a glass transition.[31,52–56] Strain glass is reported in various defect doped martensitic systems and is considered more likely to be a general phenomenon just like spin glass or relaxor in other ferroic systems.[55,57–62]

Fig. 1.6 depicts the crossover from martensite to strain glass when the defect concentration exceeds the critical value x_c. The system has a parent phase termed as strain liquid state at a very high temperature constituting of dynamic distortions/thermal vibration of each unit cell with average parent structure. With the lowering of temperature, the

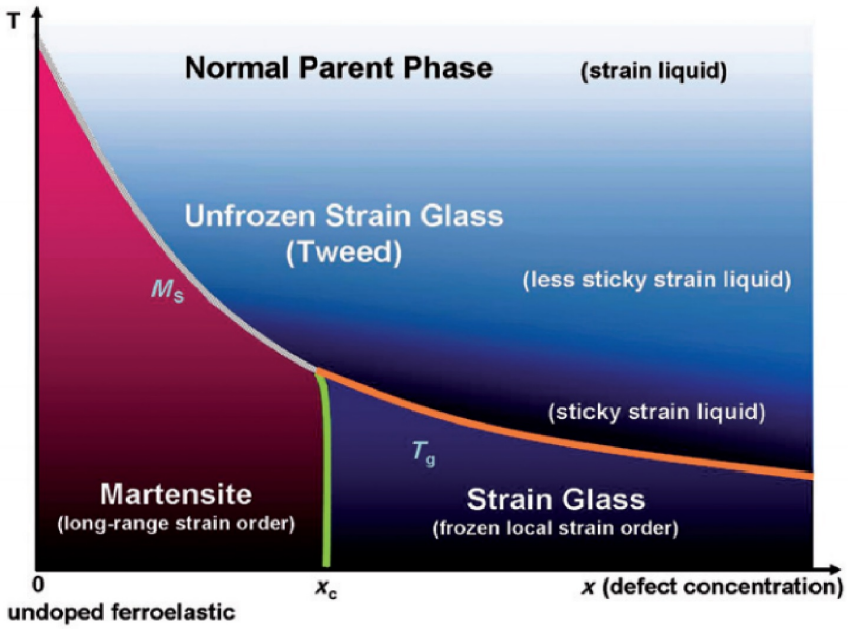

Figure 1.6: The phase diagram for the impurity doped ferroelastic system illustrating the four strain states and the crossover from martensite to strain glass.[51]

'precursor' or premartensitic state appears which is characterized by the 'sticky' strain liquid due to the growth of quasi-static strain domains due to defect doping. There is an increase in the 'stickiness' of the strain liquid with further cooling and based on the dopant concentration follow two different routes. If the dopant concentration x is less than the critical concentration x_c, the strain liquid transforms into a martensite, also termed as strain crystal. On the contrary, if the dopant content is higher than x_c, the strain liquid becomes more sticky so much so that instead of transforming into a long range strain-ordered martensite, it gets frozen into strain glass or a frozen strain liquid.[51]

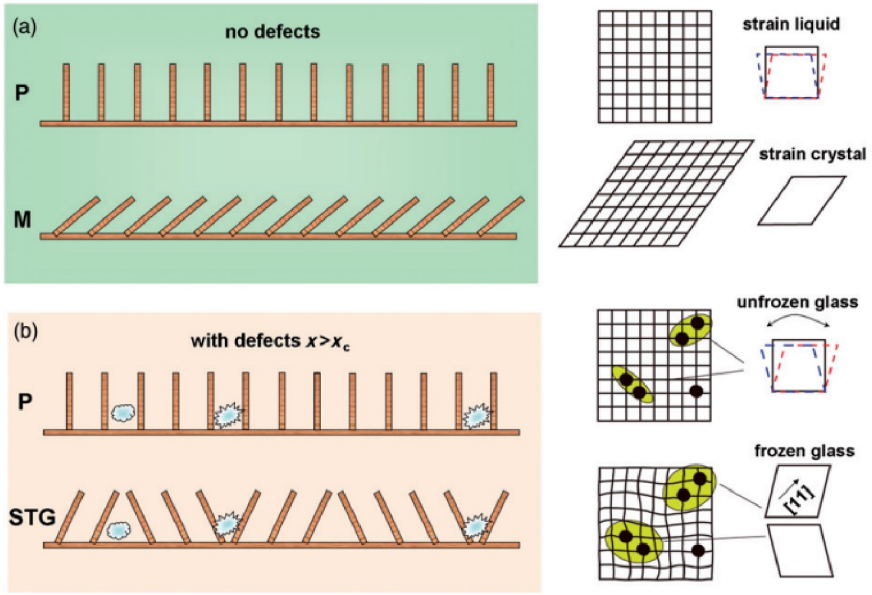

Figure 1.7: Origin of strain glass due to suppression of long-range ordering of strain by point defects. (a) The long-range strain ordering in a martensitic transition with the parent (P) and martensite (M) state represented by an array of dominos. (b) Appearance of frozen short range ordering or strain glass transition at high defect content pictured by presence of irregular stones into the domino array.[51]

1.5.1 Theoretical model for the origin of strain glass

With the sufficient amount of doping of point defects into a ferroelastic system, the strain glass appears, and hence understanding the role of point defects becomes vital for studying the origin of strain glass. One of the models proposed is referred to as the 'domino and stone' model[51] which gives an intuitive description about the formation of martensite and strain glass depending on different defect concentrations and is described in form of a cartoon in Fig. 1.7. A normal martensitic transition in a defect free system with long range ordering of domino blocks is depicted in Fig. 1.7 a. With sufficient defect concentration which are represented by irregular stones in the array (Fig. 1.7 b), the fall

of the dominos is blocked because different stones have different local preferences. Hence dominos cannot fall in a long range ordered manner and instead a local ordered pattern appears. This is the source of frustration resulting in a strain glassy state.

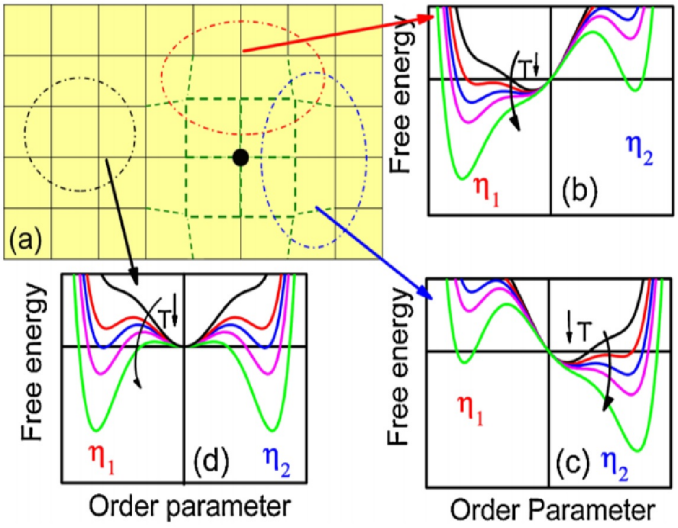

Figure 1.8: The schematic diagram of the Landau potential around point defect. The black dot depicts the lattice distortions at local level created by a doped point defect (a) and the corresponding alteration of Landau potential at three different locations (b), (c) and (d).[63]

A phase field model has been also suggested based on the local anisotropic stress effect of point defects which reproduces important features of a strain glass system.[63] For a crystal undergoing a 2-D martensitic transition, the Landau free energy in the absence of point defects is given by the equation,

$$f_{ch}(\eta_{i=1,2}) = \frac{A_1}{2}\sum_{i=1,2}\eta_i^2 - \frac{A_2}{4}\sum_{i=1,2}\eta_i^4 + \frac{A_3}{4}\left(\sum_{i=1,2}\eta_i^2\right)^2 + \frac{A_4}{6}\left(\sum_{i=1,2}\eta_i^2\right)^3 \qquad (1.4)$$

Here, $\eta_i(r)$ $(i = 1, 2)$ are parameters corresponding to long range ordering related

to the two orientation variants of the martensitic phase and A_1, A_2, A_3 and A_4 are the expansion coefficients. The Landau potential or the local field effect due to point defects is described by,

$$f_L(r) = \sum_{i,j=1,2;m=1,3,5} \eta_i^{local}(r)\eta_j^m(r) \tag{1.5}$$

where, $\eta_i^{local}(r)$ constitute the local fields associated with the static point defects. A schematics of the possible origin of the Landau potential is given in Fig. 1.8 (a) and the related effects on Landau free energy curve are depicted in Fig. 1.8 (b) and Fig. 1.8 (c). Fig. 1.8 (d) compares the temperature dependence of Landau free energy in the zero-defect crystal as described by Eqn. 1.4. A local symmetry breaking of the Landau free energy curve is seen in Fig. 1.8 (b) and Fig. 1.8 (c) when the local field effect is induced. Through computer simulations based on this model, it has been shown that there is local symmetry-breaking at all temperatures due to presence of point defects which ultimately lead to the appearance of premartensitic tweed and strain glass state.

A few more theories on the effect of point defects on elastic anisotropy and the appearance of strain glass have been proposed.[49,64–66] Attempts have also been made to apply the concepts from spin glass theories to strain glass and collectively study the different types of ferroic glasses.[67,68]

1.6 Objective of the current work

The study of the martensitic transition is mainly focused on manipulating the martensitic properties of shape memory alloys by introducing impurity atoms in their crystal structure. The recent disclosure on the existence of strain glass has provided scope for the extension of the martensite study to understanding the nano-sized martensite domains to achieve novel properties that may lead to new applications in the future. Even though there is an apparent absence of martensitic transition in the strain glass state, the nano-domains do respond to temperature and stress in a way that differ from that of a martensite.[52] Some of the properties related to this effect include superelasticity with narrow hysteresis, presence of broad damping peak over a wide temperature range, Invar and Elinvar effect in cold rolled $\beta - Ti$ alloys, and so on.[69]

Some of the examples of shape memory alloys undergoing strain glass transition are presented in the table 3.1 below.[46,55,57–59,70,71] The data listed in table 3.1 suggests that a strain glass can be induced in a martensitic alloy with a dopant concentration of $\leqslant 10\%$. The strain glassy state proceeds via gradual percolation of strain clusters that expands to attain percolating state when a minor fraction of impurity is doped to a ferroelastic/martensitic material.[72] Similar observations can be made in other ferroic materials in which a small amount of impurity dopant derives the ground state to be non-ergodic.[73–78] The structural modifications caused by the minority impurity atoms in the ferroic materials are yet to be understood. One needs to identify the structural defects

induced by the doped atoms/ions to precipitate a nonergodic ground state in such ferroic materials. It is important to note that the nature of structural defects and their ability to keep the crystal structure invariant despite the presence of martensitic domains is still not clearly understood.

Table 1.1: Examples of shape memory alloys with the critical concentration x_c of the dopants for the strain glass transitions.

Martensite	**Dopant**	x_c
$Ni_{50+x}Ti_{50-x}$	Ni	$x \geq 2$
$Ti_{50}Ni_{50-x}D_x$	D = Fe	$x \geq 6$
	D = Co	$x \geq 9$
	D = Cr	$x \geq 4.5$
	D = Mn	$x \geq 5.5$
$Ti_{50}Pd_{50-x}D_x$	D = Cr	$x \geq 9$
	D = Fe	$x > 14$
	D = Mn	$x > 13$
$Ni_{55-x}Co_xFe_{18}Ga_{27}$	Co	$x \geq 10$
$Ni_{55-x}Co_xMn_{20}Ga_{25}$	Co	$x \geq 10$

The strain glass phase is expected to occur in all ferroelastic/martensitic alloys beyond a critical dopant concentration. Latterly, studies have shown the emergence of strain glass in Co doped Ni-Mn-Ga magnetic shape memory alloys.[71] Likewise, a small amount of Fe doping in the martensitic compositions of Ni-Mn-In alloys causes a drastic reduction of martensitic transformation temperature[79] compelling one to think whether Fe atoms act like an impurity that impedes the long range ordering of elastic strain vector.

In Ni-Mn based alloys, the martensitic transition is predominantly controlled by impurity addition and largely depends on the type and concentration of dopants resulting in fascinating properties. Some of these include large magnetoresistance,[80–82] large mag-

netocaloric effect,[83,84] giant barocaloric effect,[85] and magnetic field induced strains.[86] The Ni-Mn-Z (Z = In, Sn, Sb) Heusler alloys undergo a solid-solid transformation from high temperature cubic $L2_1$ (austenitic) to low temperature, lower symmetry, orthorhombic/monoclinic (martensitic) state, or vice-versa when the dopant content exceeds a critical value.[87] This alters the magnetic ground state[88,89] resulting in some interesting phenomena like exchange bias,[90] kinetic arrest,[91,92] along with emergence of non-ergodic states like magnetic cluster glass.[93] The sudden appearance/disappearance of martensitic transition at a critical dopant concentration indicates the possibility of the existence of pre-transition phenomena like strain glass in these alloys. Further, the presence of local structural disorder in the austenitic phase seen through EXAFS investigations lends weight to the above probability.[94,95] In addition to this, recent studies have shown that the Ni-Mn-Z alloys are prone to phase separation upon temper annealing resulting in the disintegration of the martensitic structure into ferromagnetic Heusler $L2_1$ and antiferromagnetic tetragonal $L1_0$ phases.[96–100] It appears that the presence of the ferromagnetic and antiferromagnetic clusters could be due to the local segregation of different structural variants. Understanding this aspect requires a thorough investigation of the structural, magnetic, and mechanical properties of these alloys.

Hence, an attempt is made to further examine the underlying phenomena of strain glass in shape memory alloys by first trying to understand the nature of structural defects in the well-known system of Ni rich NiTi alloys wherein the strain glass was discovered. Since Fe is known to suppress the martensitic transition, the martensitic composition of

Ni-Mn-In alloys is studied by doping Fe element at the expense of Ni and Mn to testify the presence of strain glass phase. Furthermore, Ni-Mn-Z (Z = In) based magnetic shape memory alloys are investigated for the possible existence of strain glass as a pre-transition phase. As an extension to this study, these alloys are further studied as Z (Z = In) doped Ni-Mn alloys by temper annealing to explore the possible implications of structural distortions on the phase separation. Thus, the entire work is carried out keeping in mind the objectives listed below.

- To investigate the nature of structural defects which are responsible for impeding the long-range ordering of the elastic strain vector thus driving martensite into a strain glassy phase.

- To check the universality of strain glass phase. This is to inspect whether any ferroelastic/martensitic composition when doped with impurity elements that lead to the suppression of martensite has the ability to undergo strain glassy dynamics beyond a critical dopant concentration.

The successive chapters assimilated into this theses are outlined below.

- Chapter 2: Explains the preparation of alloys, various methods used for characterization along with a brief description of the instrumentation used for analytical study.

- Chapter 3: Details the study of local structural changes in Ni rich NiTi alloys as they transit from the martensitic ground state to strain glassy phase. The defect

phase responsible for the obstruction of long-range ordering has been identified to be BCC (body centered cubic) Ni and its implication on the overall structure is discussed.

- Chapter 4: The effect of Fe doping in the antiferromagnetic martensitic alloy $Ni_2Mn_{1.5}In_{0.5}$ is probed by replacing Fe in place of Mn and Ni to realise $Ni_2Mn_{1.5-x}Fe_xIn_{0.5}$ and $Ni_{2-y}Fe_yMn_{1.5}In_{0.5}$ respectively. It has been shown that when Fe is doped at the expense of Mn, the suppression of martensite occurs via strain glassy phase along with the segregation of a defect phase identified to be γ - (FeNi). On the other hand, replacement of Ni by Fe promotes $A2$ type antisite disorder resulting in a ferromagnetic austenitic state.

- Chapter 5: The Ni-Mn-In alloys are investigated near the critical concentration region for the possible existence of pre-transition phases like strain glass. Interestingly, with an increase in Mn content, the magnetic ground state becomes non-ergodic while the ferroelastic ground state retains its ergodicity. Despite the presence of structural disorder, the absence of strain glassy phase is explained to be due to the ability of the Heusler structure to accommodate strain caused by doping.

- Chapter 6: The Ni-Mn-In alloys are explored as $Ni_2Mn_{2-y}In_y$ over the entire range $0 \leq y \leq 1$, as the ground state transit from tetragonal antiferromagnet to a cubic ferromagnet. Further, the alloys are temper annealed to compare their structural and magnetic properties with quenched alloys. The study illustrates the presence

of $L2_1$ and $L1_0$ structural units in all the off-stoichiometric $Ni_2Mn_{2-y}In_y$ alloys. In quenched alloys, these structural units are packed in a single crystal structure thereby preventing the system from exhibiting the non-ergodic elastic behaviour like strain glass.

- Chapter 7: The summary of the work and the future prospects within the area of research are presented.

References

[1] V. K. Wadhawan. *Introduction to Ferroic Materials*. CRC Press, London, 2000.

[2] A. Aizu. *J. Phys. Soc. Japan*, 27:387, 1969.

[3] H. Schmid. Multi-ferroic magnetoelectrics. *Ferroelectrics*, 162:317–338, 1994.

[4] W. Eerenstein, N. D. Mathur, and J. F. Scott. *Nature*, 442:759–765, 2006.

[5] J. C. Agar, S. Pandya, R. Xu, A. K. Yadav, Z. Liu, T. Angsten, S. Saremi, M. Asta, R. Ramesh, and L. W. Martin. *MRS Communications*, 6:151–166, 2016.

[6] M. E. Fisher. The theory of equilibrium critical phenomena. *Rep. Prog. Phys.*, 30:615, 1967.

[7] Z. Kutnjak, R. Blinc, and Y. Ishibashi. Electric field induced critical points and polarization rotations in relaxor ferroelectrics. *Phys. Rev. B*, 76:104102, 2007.

[8] H. E. Stanley. *Introduction to Phase Transitions and Critical Phenomena*. Oxford: Oxford University Press, 1987.

[9] K. Binder. *Reports on Progress in Physics*, 50:783–859, 1987.

[10] R. A. Cowley. *Advances in Physics*, 29(1):1–110, 1980.

[11] E. K. H. Salje. *Phase transitions in Ferroelastic and Coelastic Materials*. Cambridge University Press, Cambridge, 1990.

[12] G. Careri. *Order and disorder in matter*. Addition Wesley, Massachusetts, 1984.

[13] K. Binder and W. Kob. *Glassy Materials and Disordered Solids*. World Scientific, London, 2005.

[14] B. Lohwongwatana, J. Schroers, and W. L. Johnson. *Phys. Rev. Lett.*, 96:075503, 2006.

[15] H. Wagner, D. Bedorf, S. Küchemann, M. Schwabe, B. Zhang, W. Arnold, and K. Samwer. *Nature Mater*, 10:439–442, 2011.

[16] B. Jèrôme and J. Commandeur. *Nature London*, 386:589, 1997.

[17] K. Binder and A. P. Young. *Rev. Mod. Phys.*, 58:801, 1986.

[18] L. Santen and W. Krauth. *Nature London*, 405:550, 2000.

[19] J. A. Mydosh. *Spin Glasses*. Taylor and Francis, Philadelphia, 1993.

[20] R. G. Palmer. *Adv. Phys.*, 31:669, 1982.

[21] M. Buchanan. *Nature London*, 435:281, 2005.

[22] D. L. Stein. *Decoherence and Entropy in Complex Systems, edited by H. T. Elze*. Springer, Berlin, 2003.

[23] X. Ren, Y. Wang, K. Otsuka, P. Lloveras, T. Castán, M. Porta, A. Planes, and A. Saxena. *MRS Bull.*, 34:838, 2009.

[24] Y. Ji, D. Wang, Y. Wang, Y. Zhou, D. Xue, K. Otsuka, Y. Wang, and X. Ren. *npj Computational Materials*, 3(43), 2017.

[25] L. E. Tanner, D. Schryvers, and S. M. Shapiro. *Mater. Sci. Eng.*, 127:205, 1990.

[26] A. Saxena. *Integrated Ferroelectrics*, 131(1):3–24, 2011.

[27] A. Saxena, T. Castán, A. Planes, M. Porta, Y. Kishi, T. A. Lograsso, D. Viehland, M. Wuttig, and M. De Graef. *Phys. Rev. Lett.*, 92:197203, 2004.

[28] Z. Xu, Myung-Chul Kim, Jie-Fang Li, and Dwight Viehland. *Philosophical Magazine A*, 74:395–406, 1996.

[29] Q. Tan and D. Viehland J. F. Li. *J. Appl. Phys.*, 88:3433, 2000.

[30] S. Karmarkar, S. Taran, B. K. Chaudhuri, H. Sakata, C. P. Sun, C. L. Huang, and H. D. Yang. *Phys. Rev. B*, 74:104407, 2006.

[31] X. Ren. *Strain glass and strain glass transition, in: Disorder and Strain-Induced Complexity in Functional Materials, Springer Series in Materials Science*, volume 148, pages 201–225. edited by T. Kakeshita, T. Fukuda, A. Saxena, and A. Planes, Springer Berlin Heidelberg, 2012.

[32] V. Seetharaman. *Bull. Mater. Sci.*, 6:703–716, 1984.

[33] M. S. Wechsler, D. S. Lieberman, and T. A. Read. *Trans. AIME*, 197:1503, 1953.

[34] J. S. Bowles and J. K. Mackenzie. *Acta Met.*, 2:129, 1954.

[35] C. M. Jackson, H. J. Wagner, and R. J. Wasilewski. *55-Nitinol - The alloy with a memory : Its physical metallurgy, properties and applications.* Tech. Rep. NASA SP-5110, NASA Technology Utilization Office, Washington, D.C., 1972.

[36] D. C. Lagoudas. *Shape Memory Alloys, Modeling and Engineering Applications.* Springer, 2008.

[37] K. Ullakko, J. K. Huang, C. Kantner, R. C. O'Handley, and V. V. Kokorin. *Appl. Phys. Lett.*, 69:1966–1968, 1996.

[38] H. E. Karaca, I. Karaman, B. Basaran, Y. I. Chumluakov, and H. J. Maier. *Acta Mater.*, 54:233–245, 2006.

[39] A. N. Vasil'ev, A. D. Bozhko, V. V. Khovailo, I. E. Dikshtein, V. G. Shavrov, V. D. Buchelnikov, M. Matsumoto, S. Suzuki, T. Takagi, and J. Tani. *Phys. Rev. B*, 59:1113–1120, 1999.

[40] V. K. Pecharsky and K. A. Gschneidner, Jr. *Phys. Rev. Lett.*, 78:4494–4497, 1997.

[41] O. Tegus, E. Brück, K. H. J. Buschow, and F. R. de Boer. *Nature (London)*, 415:150, 2002.

[42] K. Shimizu and T. Tadaki. *Shape Memory Efect: Mechanism in Shape Memory Alloys*, pages 10–23. Gordon and Breach Science, 1987.

[43] C. A. Wayman and K. Otsuka. *Shape Memory Materials.* Cambridge University Press, 1998.

[44] R. N. Bhowmik and R. Ranganathan. *J. Magn. Magn. Mater*, 248:101, 2002.

[45] R. T. Zhang, J. F. Li, and D. Vieland. *J. Am. Ceram. Soc.*, 87:864, 2004.

[46] S. Sarkar, X. Ren, and K. Otsuka. *Phys. Rev. Lett.*, 95:205702, 2005.

[47] S. Kartha, T. Castan, J. A. Krumhansl, and J. P. Sethna. *Phys. Rev. Lett.*, 67:3630, 1991.

[48] S. Kartha, J. A. Krumhansl, J. P. Sethna, and L. K. Wickham. *Phys. Rev. B*, 52:803, 1995.

[49] S. Semenovskaya and A. G. Khachaturyan. *Acta Mater*, 45:4367, 1997.

[50] A. Planes and L. Mañosa. *Solid State Phys.*, 55:159, 2001.

[51] X. Ren, Y. Wang, Y. Zhou, Z. Zhang, D. Wang, G. Fan, K. Otsuka, T. Suzuki, Y. Ji, and J. Zhang. *Philos. Mag.*, 90:141, 2010.

[52] X. Ren Y. Wang and K. Otsuka. *Phys. Rev. Lett.*, 97:225703, 2006.

[53] K. Otsuka Y. Wang, X. Ren and A. Saxena. *Phys. Rev. B*, 76:132201, 2007.

[54] K. Otsuka Y. Wang, X. Ren and A. Saxena. *Acta Mater*, 56:2885, 2008.

[55] Y. Wang, Y. Zhou, J. Zhang, X. Ding, S. Yang, X. Song, X. Ren, and K. Otsuka. *Acta Mater.*, 58:4723, 2010.

[56] Z. Zhang, Y. Wang, D. Wang, Y. Zhou, K. Otsuka, and X. Ren. *Phys. Rev. B*, 81:224102, 2010.

[57] Y. M. Zhou, D. Xue, X. Ding, Y. Wang, J. Zhang, Z. Zhang, D. Wang, K. Otsuka, J. Sun, and X. Ren. *Acta Mater*, 58:5433, 2010.

[58] Y. M. Zhou, D. Xue, X. Ding, K. Otsuka, J. Sun, and X. Ren. *Appl. Phys. Lett.*, 95:151906, 2009.

[59] Y. Wang, C. Huang, J. Gao, S. Yang, X. Ding, X. P. Song, and X. Ren. *Appl. Phys. Lett.*, 101:101913, 2012.

[60] Y. Wang, C. Huang, H. Wu, J. Gao, S. Yang, D. Wang, X. Ding, X. Song, and X. Ren. *Appl. Phys. Lett.*, 102:141909, 2013.

[61] Y. Yao, Y. D. Yang, S. Ren, C. Zhou, L. L. Li, and X. B. Ren. *Europhys. Lett.*, 100:17004, 2012.

[62] Y. Ni, Z. Zhang, D. Wang, Y. Wang, and X. Ren. *J. Alloys Compd.*, 577:S468–S471, 2013.

[63] D. Wang, Y. Wang, Z. Zhang, and X. Ren. *Phys. Rev. Lett.*, 105:20570, 2010.

[64] P. Lloveras, T. Castan, M. Porta, A. Planes, and A. Saxena. *Phys. Rev. Lett.*, 100:165707, 2008.

[65] M. Porta A. Planes P. Lloveras, T. Castan and A. Saxena. *Phys. Rev. B*, 80:054107, 2009.

[66] S. Kustov, D. Salas, E. Cesari, R. Santamarta, D. Mari, and J. Van Humbeeck. *Acta Mater.*, 73:275, 2014.

[67] R. Vasseur and T. Lookman. *Phys. Rev. B*, 81:094107, 2010.

[68] D. Sherrington. *Phys. Status Solidi B*, 251:1967–1981, 2014.

[69] X. Ren. *Phys. Status Solidi B*, 251:1982–1992, 2014.

[70] Y. Zhou, D. Xue, X. Ding, K. Otsuka, J. Sun, and X. Ren. *Phys. Status Solidi B*, 251:2027–2033, 2014.

[71] D. P. Wang, X. Chen, Z. H. Nie, N. Li, Z. L. Wang, Y. Ren, and Y. D.Wang. *Europhys. Lett*, 98:46004, 2012.

[72] H. Zong, H. Wu, X. Tao, D. Xue, J. Sun, S. J. Pennycook, T. Min, Z. Zhang, and X. Ding. *Phys. Rev. Lett.*, 123:015701, 2019.

[73] D. Viehland, M. Wuttig, and L. E. Cross. *Ferroelectrics*, 120(1):71–77, 1991.

[74] V. V. Shvartsman, J. Zhai, and W. Kleemann. *Ferroelectrics*, 379:77–85, 2009.

[75] L. Cui, Y. D. Hou, S. Wang, C. Wang, and M. K. Zhu. *J. Appl. Phys.*, 107:054105, 2010.

[76] J. Blasco1, V. Cuartero1, J. García, and J. A. Rodríguez-Velamazán. *J. Phys.: Condens. Matter*, 24:076006, 2012.

[77] C. Djurberg, P. Svedlindh, P. Nordblad, M. Hansen, F. Bødker, and S. Mørup. *Phys. Rev. Lett.*, 79:5154, 1997.

[78] D. Kumar and A. Banerjee. *J. Phys. Condens.Matter*, 25:216005, 2013.

[79] D. N. Lobo, K. R. Priolkar, S. Emura, and A. K. Nigam. *J. Appl. Phys.*, 116:183903, 2014.

[80] K. Koyama, H. Okada, K. Watanabe, T. Kanomata, R. Kainuma, W. Ito, K. Oikawa, and K. Ishida. *Appl. Phys. Lett.*, 89:182510, 2006.

[81] V. K. Sharma, M. K. Chattopadhyay, K. H. B. Shaeb, A. Chouhan, and S. B. Roy. *Appl. Phys. Lett.*, 89:222509, 2006.

[82] S. Y. Yu, Z. H. Liu, G. D. Liu, J. L. Chen, Z. X. Cao, G. H. Wu, B. Zhang, and X. X. Zhang. *Appl. Phys. Lett.*, 89:162503, 2006.

[83] T. Krenke, E. Duman, M. Acet, E. F. Wassermann, X. Moya, L. Mañosa, and A. Planes. *Nat. Mater*, 4:450, 2005.

[84] X. Moya, L. Mañosa, A. Planes, S. Aksoy, M. Acet, E. F.Wassermann, and T. Krenke. *Phys. Rev. B*, 75:184412, 2007.

[85] L. Mañosa, D. González-Alonso, A. Planes, E. Bonnot, M. Barrio, J. L. Tamarit, S. Aksoy, and M. Acet. *Nat. Mater*, 9:478, 2010.

[86] R. Kainuma, Y. Imano, W. Ito, Y. Sutou, H. Morito, S. Okamoto, O. Kitakami, K. Oikawa, A. Fujita, T. Kanomata, and K. Ishida. *Nature*, 439:957, 2006.

[87] P. J. Webster, K. R. A. Ziebeck, S. A. Towns, and M. S. Peak. *Phil. Mag B*, 49:295, 1984.

[88] T. Krenke, M. Acet, E. F. Wassermann, X. Moya, L. Mañosa, and A. Planes. *Phys. Rev. B*, 73:174413, 2006.

[89] K. R. Priolkar, P. A. Bhobe, D. N. Lobo, S. W. D'Souza, S. R. Barman, Aparna Chakrabarti, and S. Emura. *Phys. Rev. B*, 87:144412, 2013.

[90] M. Khan, I. Dubenko, S. Stadler, and N. Ali. *Appl. Phys. Lett*, 91:072510, 2007.

[91] W. Ito, K. Ito, R. Y. Umetsu, R. Kainuma, K. Koyama, K. Watanabe, A. Fujita, K. Oikawa, K. Ishida, and T. Kanomata. *Appl. Phys. Lett.*, 92:021908, 2008.

[92] V. K. Sharma, M. K. Chattopadhyay, and S. B. Roy. *Phys. Rev.B*, 76:140401R, 2007.

[93] K. Yadav, M. K. Sharma, S. Singh, and K. Mukherjee. *Sci. Rep.*, 9:15888, 2019.

[94] P. A. Bhobe, K. R. Priolkar, and P. R. Sarode. *J. Phys.:Condens. Matter*, 20:015219, 2008.

[95] D. N. Lobo, K. R. Priolkar, P. A Bhobe, D. Krishnamurthy, and S. Emura. *Appl. Phys. Lett.*, 96:38006, 2010.

[96] A. Çakir, M. Acet, and M. Farle. *Sci. Rep.*, 6:28931, 2016.

[97] T. Krenke, A. Çakir, F. Scheibel, M. Acet, and M. Farle. *J. Appl. Phys.*, 120:243904, 2016.

[98] A. Çakir and M. Acet. *J Magn Magn Mater*, 448:13–18, 2018.

[99] Z. Wanjiku, A. Çakir, F. Scheibel, U. Wiedwald, M. Farle, and M. Acet. *J. Appl. Phys.*, 125:043902, 2019.

[100] A. Çakir, M. Acet, U. Wiedwald, T. Krenke, and M. Farle. *Acta Mater*, 127:117–123, 2017.

Chapter 2

Experimental Techniques

2.1 Introduction

The current chapter categorically details the procedure involved in the alloy preparation along with the different experimental techniques used for the characterization of the prepared alloys. To begin with, the diffraction experiments using x-ray and neutron radiations as a source are described, which were performed to obtain the crystal structure solutions. Further, magnetic property measurements are discussed, which were carried out to understand the magnetic ground state. A brief description of the thermal analysis measurements like Differential scanning calorimetry (DSC) and Differential thermal analyzer (DTA) is given, along with four probe resistivity, conducted to determine the martensitic transition temperatures and to study the transport property. In addition to this, Dynamical mechanical analyzer (DMA) measurements are also explained which were performed to testify the presence of structural glassy phase. Towards the end, the XAFS technique is illustrated to gain insight into the structural changes occurring at the local level.

2.2 Sample Preparation

The alloys were prepared by arc melting technique in an argon atmosphere using *Centorr* arc furnace. During the process, the constituent elements of the alloy were taken in stoichiometric proportions and melted. The resultant alloy bead was flipped multiple times and remelted to ensure homogeneity. The prepared alloys were then encapsulated in quartz tubes and vacuum sealed ($\sim 10^5$ mm of Hg) to be annealed at high temperatures. The NiTi alloys were annealed at 1000°C for 1 hour while the NiMn based Heusler alloys were annealed at 750°C for 48 hours and subsequently ice quenched. The prepared alloys were cut using low speed diamond saw and powdered. The powdered NiMn based Heusler alloys were re-annealed under similar conditions as described before for further characterization. The entire synthesis procedure was carried out at the School of Physical and Applied Sciences - Goa University, India.

2.3 Diffraction experiments

The diffraction experiments were achieved using finely ground alloy powders. The room temperature x-ray diffraction measurements were performed on Rigaku diffractometer using Mo K_α radiation ($\lambda = 0.70926$ Å) at the School of Physical and Applied Sciences, Goa University and on X'Pert diffractometer using Cu K_α radiation ($\lambda = 1.5418$ Å) at the Department of Condensed Matter Physics and Material Science, TIFR, Mumbai (India). The temperature dependent measurements in the range 80 K $\leq T \leq$ 390 K were carried out on ARLX'TRA diffractometer using Cu K_α radiation at the Department of Chemistry,

Parma University (Italy). While the Synchrotron x-ray diffraction measurements were employed on BL-18B at Photon Factory, KEK-Tsukuba (Japan) using incident photons of 16 KeV ($\lambda = 0.77637$ Å) at 300 K and 500 K.

Neutron time of flight (TOF) diffraction data was collected on the WISH diffractometer at the ISIS pulsed neutron and muon facility (United Kingdom).[1] The sample powders were placed in a cylindrical Vanadium can and the measurements were performed in the temperature range 5-400 K using a close circuit refrigerator. In the time of flight method, the neutrons are made to travel over a fixed path length so that its velocity and consequently the wavelength can be measured. If λ is the de-Broglie wavelength of a neutron with momentum mv, then

$$\lambda = h/mv = ht/mL = 2dsin\theta \tag{2.1}$$

In this case, L is the path length and t is the time-of-flight. The time of flight is proportional to d spacing due to which, the TOF powder diffraction patterns are normally displayed with the ordinate axis going from small to large d spacing. This is in contrast to both angle-dispersive and energy-dispersive methods having a reverse scale in terms of d spacing.

2.3.1 Bragg's condition

The diffraction technique is based on the constructive interference of the scattered quantum beams (x-ray, neutron, or electron) from a crystalline sample used for identifying the

atomic and molecular structure of a crystal. This is described by the Bragg's condition.[2–4] The electromagnetic radiation with a wavelength λ comparable to the atomic spacings is scattered by the array of atoms in the lattice planes separated by the interplanar distance d_{hkl} of a crystalline system. The scattered waves remain in phase if they interfere constructively as the path difference of the two waves is equal to the integer multiple of the wavelength. The path difference is given by $2dsin\theta$ where θ is the glancing angle. The cumulative effect of reflection in successive crystallographic planes (h,k,l)(as described by Miller notation) of the crystalline lattice is aggravated by the constructive or destructive interference. The condition on θ for the constructive interference to be at its strongest is given by

$$n\lambda = 2d_{hkl}sin\theta_{hkl} \tag{2.2}$$

Although the diffraction theory is equally applicable to both x-ray and neutron wavelengths which are comparable with inter-atomic distances, there is a significant difference in the scattering of these two types of radiations. In the scattering of x-rays by atoms, there is an interaction with the atomic electrons with scattering amplitude being approximately proportional to the atomic number Z of the scatterer resulting in the angular distribution of scattering usually referred to as form factor. This is definitive of the spatial distribution of the electrons. The scattering of neutrons by atoms involves two important interactions. The first is the short range interactions of the neutrons with the nucleus of the atom and the second is the interactions of the magnetic moment of the

neutron with the atomic spin and orbital magnetic moments. With the nuclear interactions producing isotropic scattering, the regular variation of the scattering amplitudes with atomic number is not seen. The size and orientation of the atomic magnetic moment govern the magnetic interaction while the intensity of scattering has a form-factor angular dependence that is representative of the magnetic electrons.[5]

2.3.2 Data analysis

The crystal structure solution was obtained through LeBail and Reitveld methods using Jana 2006 software.[6] A hypothetical model was generated based on the crystallographic space group consisting of lattice constants, atomic site occupancies, fractional coordinates, etc. wherein, the parameters were iteratively refined by the Least Square method.

The more complicated modulated structure of the NiMn based alloys in their martensitic state was solved using the superspace approach formulated by Janssen and Janner.[7–10] The martensitic structure displayed main peaks coming from the monoclinic structure $I2/m$ along with satellite reflections indicating the presence of structural modulations. In literature, the Mn rich NiMn type Heusler alloys are generally known to exhibit 7M incommensurate modulations. Hence considering the structural modulation to be incommensurate, a similar procedure as described in *Righi et al 56 (2008)* was employed.[11,12] The modulation vector q was introduced to describe the structural modulations which is defined as the linear combination of reciprocal lattice vectors. The modulation function was described by the sawtooth function which is normally used in the refinement of structures with abrupt modulation changes of position and occupation.[13] The sawtooth

function incorporates the crenel modulation of occupancy with the linear modulation of position. Hence, it embodies the width, the centre and the slope of the line along the x_1, x_2 and x_3 axis of the basic unit cell while x_4 is the additional superspace coordinate as defined in the Fig 2.1. Suitable constraints were imposed and starting from 3 + 1 dimensional model, refinement was performed which resulted in the contribution from only the single component of the reciprocal space to the modulation vector q. The refinement confirmed the structure to be incommensurate with a sevenfold modulations (seven adjacent unit cells along one of the crystallographic axes). Depending on the direction of propagation of the modulation wave, the superspace group was obtained to be either $I2/m(\alpha 0\gamma)00$ or $I2/m(\alpha\beta 0)00$ if the direction was chosen along b axis or c axis respectively.

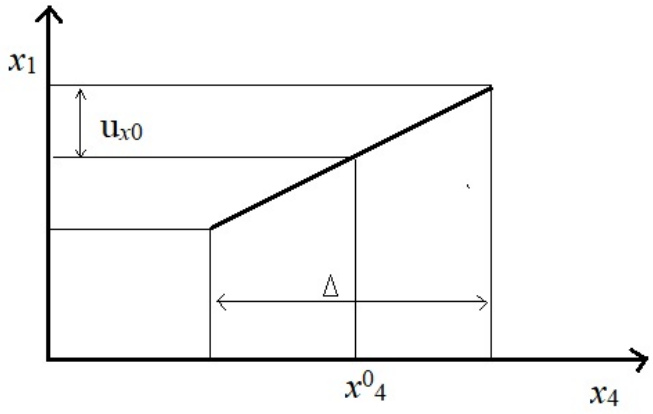

Figure 2.1: The sawtooth wave function.

In Mn rich Ni-Mn-In alloys, a systematic structural study was performed by collecting

time of flight neutron diffraction data at different temperatures spanning the entire structural and magnetic transition region. Certain alloys with Mn excess content less than the critical value displayed no structural transition and maintained austenitic behaviour up to 5 K with the cubic space group $Fm\bar{3}m$. However, below T_C a systematic shift of intensity towards lower d of the 101 peak with temperature was identified presumed to be due to magnetic origin.

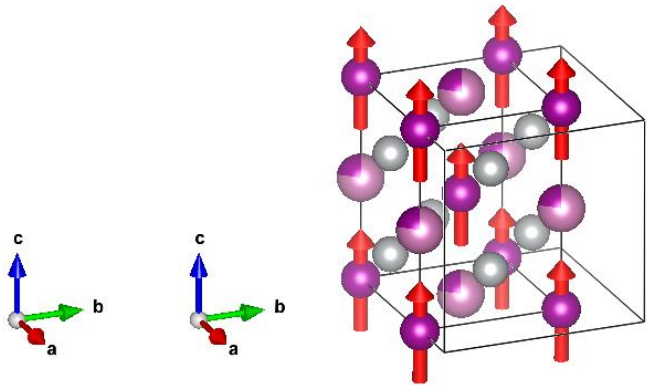

Figure 2.2: Cubic to tetragonal transition of unit cell with the constraint c = $\sqrt{2}$*a

It should be noted that the para-ferro conversion of the austenite cannot be considered as a pure second order transition since the structural analysis of the ferromagnetic state involves a symmetry breaking process. This is because the symmetry requirements for the coherent alignment of spins within a cubic lattice are inconsistent with all cubic space groups. Below T_C, the symmetry of the Heusler austenite must change so as to properly accomodate the periodicity of the spin correlations. The ferromagnetic alignment of spins on Mn atoms is illustrated by suppressing the cubic symmetry to tetragonal symmetry

with the constraint c = $\sqrt{2}$*a (Fig.2.2). The refinement for the austenitic phase is thus carried out by keeping the symmetry of the parent structure as I4/mm'm' and using the propagation vector k = (0 0 0) for magnetic structure analysis.[14–16] The average magnetic moment on Mn atoms was obtained by constraining the magnetic moments for Mn1 and Mn2 (Mn/In semi occupied site) to assume the same value. The TOF profile was expressed as a pseudo-voigt function involving a back-to-back exponential asymmetry while the anisotropic broadening of reflections were taken care of by introducing an anisotropic strain tensor.

2.4 Magnetic property measurements

The magnetic properties were measured on alloy pieces ($\sim$ 20 mg) on SQUID (Superconducting Quantum Interference Device) magnetometer, Quantum Design at the Department of Condensed Matter Physics and Material Sciences, TIFR, Mumbai (India), the Department of Mathematical, Physical and Computer Sciences, Parma University (Italy) and at Experimentalphysik, University of Duisburg-Essen, Duisburg (Germany). The magnetization measurements M(T) were performed in the temperature range of 5 – 350 K. The samples were first cooled in zero applied magnetic field and then the ZFC (zero field cooled) data was recorded while warming in the appropriate field (magnetic fields of 0.005T, 0.01T, 0.02T, 0.1T, and 5T were used for different alloy compositions) followed by subsequent cooling and warming cycles termed as FCC (field cooled cooling) and FCW (field cooled warming) respectively. The isothermal magnetization measurements M vs H

were carried out in the field range of ± 7 T. The alloy compositions were first cooled in zero field from 350 K to 5 K (ZFC-M(H)). The samples were cooled again from 350 - 5 K in an applied field of 5 T to record the field cooled magnetization loops (FC-M(H)). The ac magnetic field of H_{ac} = 10 Oe was employed to perform the ac magnetic susceptibility measurements in the temperature range 5 – 350 K at different excitation frequencies (33 Hz $\leqq f \leqq$ 9997 Hz). The measurements were performed by first cooling the samples in zero field in Physical Properties Measurement System (PPMS) Quantum Design.

2.4.1 Principle of DC and AC Magnetometry

The equilibrium value of magnetization in a sample is determined by the DC magnetization measurements. The sample is magnetized by a constant magnetic field and the magnetic moment of the sample is measured, producing a DC magnetization curve. The magnetic moment is most commonly measured by induction technique wherein the inductive measurements are carried out by moving the sample relative to a set of pickup coils, either by vibration or one-shot extraction. The technique uses a set of superconducting pickup coils and SQUID[17–20] to measure the current induced in superconducting pickup coils, yielding a high sensitivity that is independent of sample speed during extraction.[21,22]

AC magnetic measurements involve the superimposition of a small AC drive magnetic field on the DC field resulting in a time-dependent moment in the sample which induces a current in the pickup coils, allowing measurement without sample motion. At low frequencies, where the measurement is almost similar to DC magnetometry, the induced AC moment is given by,

$$M_{AC} = \frac{dM}{dH} H_A C sin(wt) \tag{2.3}$$

Here, H_{AC} is the amplitude of the driving field, ω is the driving frequency, and $\chi = \frac{dM}{dH}$ is the slope of the M(H) curve, called the susceptibility.

With the change in the DC field, different susceptibilities are accessed from different parts of M(H) curve. Since the AC measurement is sensitive to the slope of M(H), small magnetic shifts can be recognized even when the absolute moment is large.

At higher frequencies, the AC moment does not follow the DC magnetization curve due to dynamic effects in the sample. This may result in the magnetization of the sample lagging behind the drive field, an effect detected by the magnetometer circuitry. This leads to the generation of two quantities, the magnitude of susceptibility χ and phase shift θ (relative to the driving signal). Hence susceptibility acquire an in-phase or a real component χ' and an out of phase or an imaginary component χ'' given by,

$$\begin{cases} \chi' = \chi cos\theta & \chi = \sqrt{\chi'^2 + \chi''^2} \\ \chi'' = \chi sin\theta & \theta = tan^{-}1\frac{\chi''}{\chi'} \end{cases} \tag{2.4}$$

In other words, the AC susceptibility is represented as,

$$\chi_{AC} = \chi' - i\chi'' \tag{2.5}$$

The real component which is related to the reversible magnetization remains in field with the oscillating field,

$$H(t) = H_0 + hcos(2\pi ft) \tag{2.6}$$

While the imaginary component is related to the loss due to irreversible magnetization and energy absorbed from the field. The magnetization M(t) with respect to the oscillating field H(t) is given by,

$$M(t) = M_0 + mcos(2\pi ft - \theta) \tag{2.7}$$

With θ being the phase shift, we have, $\chi' = mcos\frac{\theta}{h}$ and $\chi'' = msin\frac{\theta}{h}$. The real and the imaginary components of the susceptibility of the magnetic sample are functions of temperature and may depend on the frequency f, amplitude h of the driving field, the static bias field H_0, the applied pressure and other external parameters.

2.5 Thermal Analysis

Differential Scanning calorimetry (DSC) measurements were carried out at the School of Physical and Applied Sciences, Goa University using a Shimadzu DSC-60[23] in the temperature range of 200 - 800 K on $\sim$ 8mg pieces of individual alloy crimped in an aluminium pan. Likewise, differential thermal analyzer (DTA) measurements were performed in the temperature range of 300 - 1100 K using Shimadzu DTG-60[23] on small pieces of each alloy ($\sim$ 8 mg) placed in a platinum pan. Heating/cooling cycles were recorded in an inert atmosphere at a constant rate of 5°C/min.

2.5.1 Principle

DSC is a thermoanalytical technique wherein a reference (empty aluminium pan) and a sample (sample crimped in aluminium pan) are used, both of which are maintained at

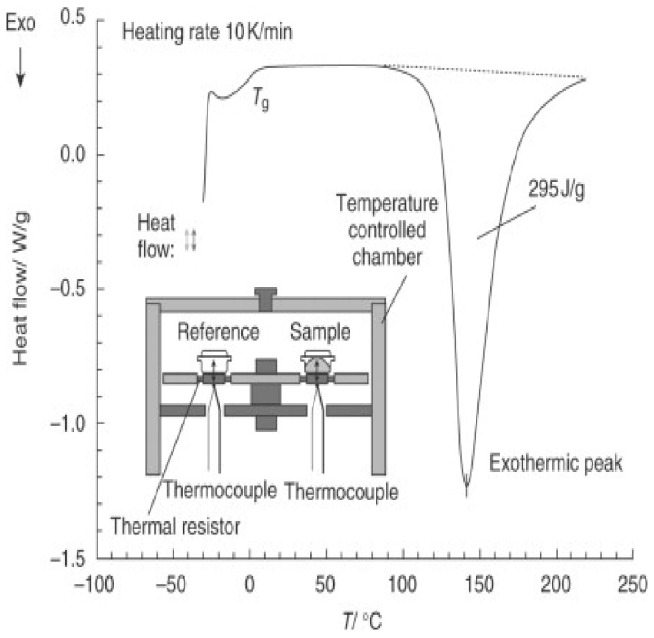

Figure 2.3: Schematic of DSC set up and thermogram.[24]

nearly same temperature throughout the experiment and the difference in the amount of heat required to increase or decrease the temperature as a function of temperature is measured. When the sample undergoes a phase transition, the amount of heat flow to the sample either increases or decreases then the reference, based on whether the process is endothermic or exothermic to maintain both the sample and the reference at the same temperature. The differential scanning calorimeters can measure the amount of heat absorbed or released during transitions based on the difference in heat flow between the sample and reference given by $\Delta\frac{dH}{dt}$, H being the enthalpy. DSC thermogram is obtained by plotting $\frac{dH}{dt}$ as a function of time or temperature. Exothermic and endothermic reac-

tions are observed as peaks or dips respectively in the DSC curve and the area under the peak corresponds to the heat evolved or absorbed during the transition (Fig. 2.3).[25]

DTA is an alternative technique wherein, the heat flow to the sample and reference remains the same rather than the temperature. During the phase transition, both the sample and the reference are heated identically, resulting in a temperature difference between the two. While both the techniques provide similar information, DSC estimates the energy required to keep both the reference and the sample at the same temperature contrary to DTA, which measures the difference in temperature between the sample and the reference when the same amount of energy is introduced to both.

2.6 Four probe resistivity measurement

The electrical resistivity measurements were carried out on thin rectangular cut alloy pieces, in the temperature range of 20 - 450 K, using conventional D.C. four probe setup[26] in a closed cycle refrigerator (CCR) at the School of Physical and Applied Sciences, Goa University.

2.6.1 Principle

Depending upon the resistance of each sample, a current I from the constant current source is passed through the two current probes and the potential drop V across the two voltage probes is measured. As negligible current is drawn by the voltmeter, the resistance R across the sample is measured using Ohm's law,

$$V = IR \tag{2.8}$$

Further, the electrical resistivity is measured using the relation,

$$\rho = R\frac{A}{l} \tag{2.9}$$

Here, l is the length and A is the area of cross section of the sample.

2.7 Dynamical Mechanical Analysis

The mechanical properties of the prepared alloy compositions were measured using the dynamical mechanical analysis (DMA) technique at the School of Physical and Applied Sciences, Goa University. The Dynamic mechanical analyzer (Q800, TA Instruments)[27,28] was used in multi-frequency mode wherein the ac storage modulus and internal friction ($tan\delta$) were measured at different frequencies ranging from 0.1 Hz to 10 Hz. The measurements were carried out using 3 point bending mode by applying a small AC stress that generated a maximum displacement of 5 μm on rectangular pieces each of ($10mm \times 5mm \times 1mm$) dimensions.

2.7.1 Principle

DMA measures the viscoelastic property of a material in the most common dynamic oscillatory test, wherein a sinusoidal force (stress σ) is applied to a material and the resulting displacement (strain ε) is measured. For a perfectly elastic solid, the resultant strain and the stress are perfectly in phase while for a purely viscous fluid, there is a

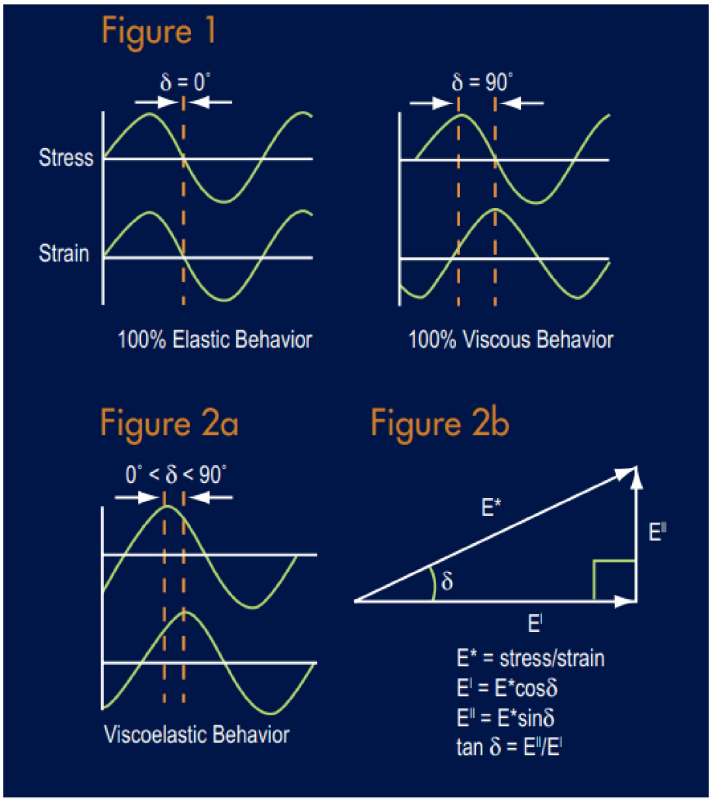

Figure 2.4: Schematic displaying the behaviour of the stress wave in elastic, viscous and viscoelastic materials.[27]

90° phase lag of strain with respect to stress. Viscoelastic materials have in between characteristics (Fig. 2.4) and exhibit some phase lag during DMA tests[29] upholding the following equations:

$$\sigma = \sigma_0 sin(\omega t + \delta) \tag{2.10}$$

$$\varepsilon = \varepsilon_0 sin(\omega t) \tag{2.11}$$

Here, ω is the frequency of strain oscillations, t is the time and δ is the phase lag between stress and the strain.

In a purely elastic case, where stress is proportional to strain,

$$\sigma = E\varepsilon(t) \Rightarrow \sigma_0 sin(\omega t) = E\varepsilon_0 sin(\omega t) \Rightarrow \delta = 0 \tag{2.12}$$

In a purely viscous case, stress is proportional to strain rate,

$$\sigma = K\frac{dE}{dt} \Rightarrow \sigma_0 sin(\omega t) = K\varepsilon_0 \omega cos(\omega t) \Rightarrow \delta = \frac{\pi}{2} \tag{2.13}$$

The tensile storage and loss moduli are described as follows,

$$\text{Storage modulus} : \mathrm{E}' = \frac{\sigma_0}{\varepsilon_0}\cos\delta \tag{2.14}$$

$$\text{Loss modulus} : \mathrm{E}'' = \frac{\sigma_0}{\varepsilon_0}\sin\delta \tag{2.15}$$

$$\text{Phase angle} : \delta = \frac{\mathrm{E}''}{\mathrm{E}'} \tag{2.16}$$

The storage modulus corresponds to the elastic portion, measuring the stored energy while the energy dissipated as heat is measured by the loss modulus which represents the viscous portion.

2.8 X-ray absorption fine structure (XAFS) spectroscopy

X-ray absorption fine structure (XAFS) is one of the best techniques to map the local structural distortions in the neighbourhood of the absorbing atom due to impurity addition. For the finely powdered alloy compositions, the incident and the transmitted photon energies were simultaneously recorded at Ti K (4966 eV), Mn K (6539 eV), Fe K (7111 eV), and Ni K (8333 eV) edges. Using gas ionisation chambers as detectors, multiple

spectra were recorded for Ni, Ti, and Mn K edges in transmission mode and for Fe K edge in florescence mode to reduce the statistical noise. Layers of scotch tape containing uniformly spread powdered alloys were stacked to prepare absorbers whose thickness was adjusted to obtain the absorption edge jump $\Delta\mu(t) \leq 1$. $\Delta\mu$ corresponds to the change in absorption coefficient at the absorption edge and t is the thickness of the absorber. The experiments were carried out at the P65 beamline at PETRA III Synchrotron Source (DESY, Hamburg, Germany) and at the XAFS beamline at Elettra Synchrotron Source (Trieste, Italy).

2.8.1 Theory of XAFS

X-ray Absorption Fine-Structure (XAFS) is the modulation of the x-ray absorption coefficient $\mu(E)$ at energies near and above an x-ray absorption edge and is broken into 2 regimes, X-ray Absorption Near-Edge Spectroscopy (XANES) and Extended X-ray Absorption Fine-Structure (EXAFS).

During the photoelectric process, atoms absorb the x-ray energy, which is transferred to a core-level electron (K, L, or M shell) ejected from the atom. The atom is left in an excited state with an empty electronic level (a core hole) while the excess energy from the x-ray is given to the ejected photo-electron. The higher level core electron drops into the core hole, as the excited core-hole tries to relax back to a ground state of the atom, and a fluorescent x-ray or Auger electron is emitted (Fig. 2.5 a). X-ray fluorescence and Auger emission occur at discrete energies that are characteristic of the absorbing atom and can be used to identify the absorbing atom.[30]

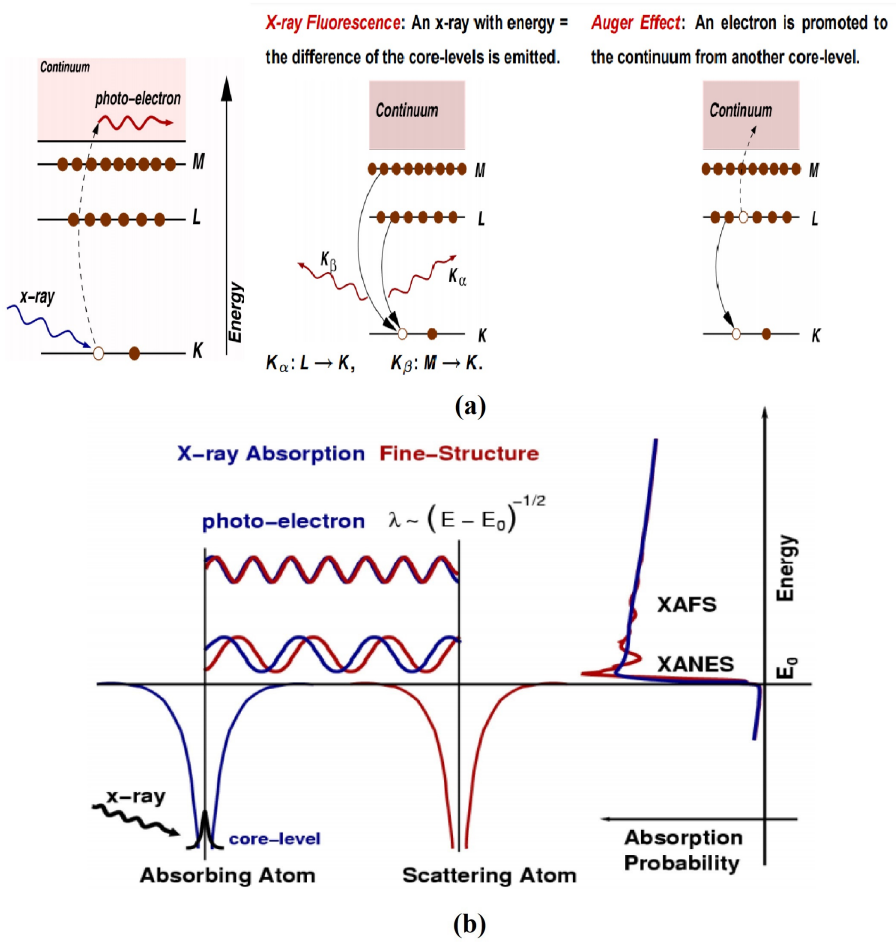

Figure 2.5: Schematic representations for : (a) Photoelectric process depicting the creation of a single photoelectron followed by emission of fluorescent x-ray and Auger electron, (b) Backscattering of the ejected photoelectron wave from the neighbouring atoms.[30]

Consider E being the x-ray energy absorbed by an atom destroying a core electron with energy E_0 and creating a photo-electron with energy $E-E_0$. Once the x-ray energy is large enough to promote a core level to the continuum, there is a sharp increase in absorption. For an isolated atom, $\mu(E)$ has a sharp step at the core-level binding energy and is a smooth function of energy above the absorption edge. With another atom nearby, the ejected photo-electron scatters from a neighboring atom and returns back to the absorbing

atom interfering with itself. With μ depending upon the presence of an electron state with energy $E - E_0$ at the absorbing atom, the amplitude of the back-scattered photo-electron at the absorbing atom varies with energy, causing the oscillations in $\mu(E)$ which are XAFS (Fig. 2.5 b). The XAFS oscillations are an interference effect of the photo-electron with itself, due to the presence of neighboring atoms.

The energy dependent oscillations in $\mu(E)$ contains the information about the neighbouring atoms and hence, EXAFS is defined as

$$\chi(E) = \frac{\mu(E) - \mu_0(E)}{\Delta\mu_0(E)} \tag{2.17}$$

$\mu(E)$ is described as the transition between quantum states by Fermi's Golden Rule,

$$\mu(E) \sim |\langle i|H|f\rangle|^2 \tag{2.18}$$

Here,

- $\langle i|$ represents the initial state corresponding to core level and the photon that is not altered by the neighboring atom.
- H is the interaction wherein,$H = e^{ikr} \approx 1$ in dipole approximation.
- $|f\rangle$ is the final state describing the photoelectron which is affected by the neighboring atom.

With Δf being the change in the photo-electron final state as a result of backscattering from the neighboring atom, $|f\rangle$ can be written as $|f\rangle = |f_0 + \Delta f\rangle$. Further, μ can be expanded as

$$\mu(E) \sim |\langle i|H|f\rangle|^2[1 + \frac{\langle i|H|f\rangle\langle f_0|H|i\rangle^*}{|\langle i|H|f\rangle|^2} + C.C] \tag{2.19}$$

Using the definition for χ,

$$\mu(E) = \mu_0(E)[1 + \chi(E)] \tag{2.20}$$

since $\mu_0 E$ is given by $|\langle i|H|f_0\rangle|^2$, $\chi(E)$ can be represented as,

$$\chi(E) \sim \langle i|H|\Delta f\rangle \sim \langle i\Delta f\rangle \tag{2.21}$$

The initial state for the core-level is nearly a delta-function in space (centered at the absorbing atom), hence this becomes,

$$\chi(E) \approx \int dr\delta(r)\psi_{scatt}(r) = \psi_{scatt}(0) \tag{2.22}$$

The XAFS χ is the result of the oscillations in the photo-electron wave-function at the absorbing atom caused by the scattering from neighboring atoms.

With $\chi \sim \psi_{scatt}(0)$, a simple model is built for χ from the photoelectron leaving the absorbing atom, scattering from the neighboring atom, and returning to the absorbing atom. With spherical wave $e^{ikr/kr}$ for the propagating photo-electron, and a scattering atom at a distance $r = R$, we get,

$$\chi(k) = \frac{e^{ikR}}{kR}[2kf(k)e^{i\delta(k)}]\frac{e^{ikR}}{kR} + C.C \tag{2.23}$$

The neighboring atom gives the amplitude $f(k)$ and phase-shift $\delta(k)$ to the scattered photo-electron. Combining terms (including the complex conjugate) for one scattering atom;

$$\chi(k) = \frac{f(k)}{kR^2} sin[2kR + \delta(k)] \tag{2.24}$$

For N neighbouring atoms, and with thermal and static disorder of σ^2, giving the mean-square disorder in R,

$$\chi(k) = \frac{Nf(k)e^{-2k^2\sigma^2}}{kR^2} sin[2kR + \delta(k)] \tag{2.25}$$

In a real system, neighbouring atoms are of different types, present at different distances. By adding all these contributions, the EXAFS equation can be written as:

$$\chi(k) = \sum_j \frac{N_j f_j(k) e^{-2k^2\sigma_j^2}}{kR_j^2} sin[2kR_j + \delta_j(k)] \tag{2.26}$$

If the photo-electron scatters inelastically, it may not get back to the absorbing atom. Further, the core level has a finite lifetime, limiting how far the photoelectron can go. Hence a damped wave function is used given by $e^{ikr}e^{-r/\lambda(k)}$/kr, wherein $\lambda(k)$ is the photoelectrons mean free path. The EXAFS equation now becomes;

$$\chi(k) = \sum_j \frac{N_j f_j(k) e^{-2R_j/\lambda(k)} e^{-2k^2\sigma_j^2}}{kR_j^2} sin[2kR_j + \delta_j(k)] \tag{2.27}$$

The mean free path λ is dependent on k and is less than 25 Åfor the EXAFS k range. The terms λ and R^{-2} cause EXAFS to turn into a local probe.

Another important amplitude reduction term is S_0^2 which corresponds to the relaxation of all the other electrons in the absorbing atom to the hole in the core level given by

$S_0^2 = |\langle\phi_f^{N-1}|\phi_0^{N-1}\rangle|^2$ wherein $\langle\phi_f^{N-1}|$ accounts for the relaxation of other (N-1) electrons relative to electrons in the unexcited atom $|\phi_0^{N-1}\rangle$. Typically, S_0^2 is a constant correlated to N and is calculated for a given central atom to be multiplied to the XAFS χ.

Generally, S_0^2 is established from a "standard" (sample with a well known structure) and applied as a scale factor to a set of unknowns.

The final equation used to model and interpret XAFS is;

$$\chi(k) = \sum_j \frac{N_j S_0^2 f_j(k) e^{-2R_j/\lambda(k)} e^{-2k^2\sigma_j^2}}{kR_j^2} sin[2kR_j + \delta_j(k)] \tag{2.28}$$

Here, $f(k)$ and $\delta(k)$ are the photoelectron scattering properties and depend on the atomic number Z of the neighbouring atoms, $\lambda(k)$ is the mean free path and S_0^2 is the amplitude reduction term due to the relaxation of all the other electrons in the absorbing atom to the hole in the core level. The distance between the neighbouring atom R, the coordination number of the neighbouring atom N, and the mean square disorder of the neighbour distance are determined by calculating the scattering properties.

2.8.2 EXAFS: Data reduction

Generally, EXAFS is recorded in transmission, and if I_0 is the intensity of the x-ray beam passing through the material of thickness t and I is the transmitted intensity, then :

$$I = I_0 e^{-\mu t} \tag{2.29}$$

μ depends strongly on the x-ray energy E, atomic number Z, the density ρ and atomic mass A such that $\mu \sim \frac{\rho Z^4}{AE^3}$.

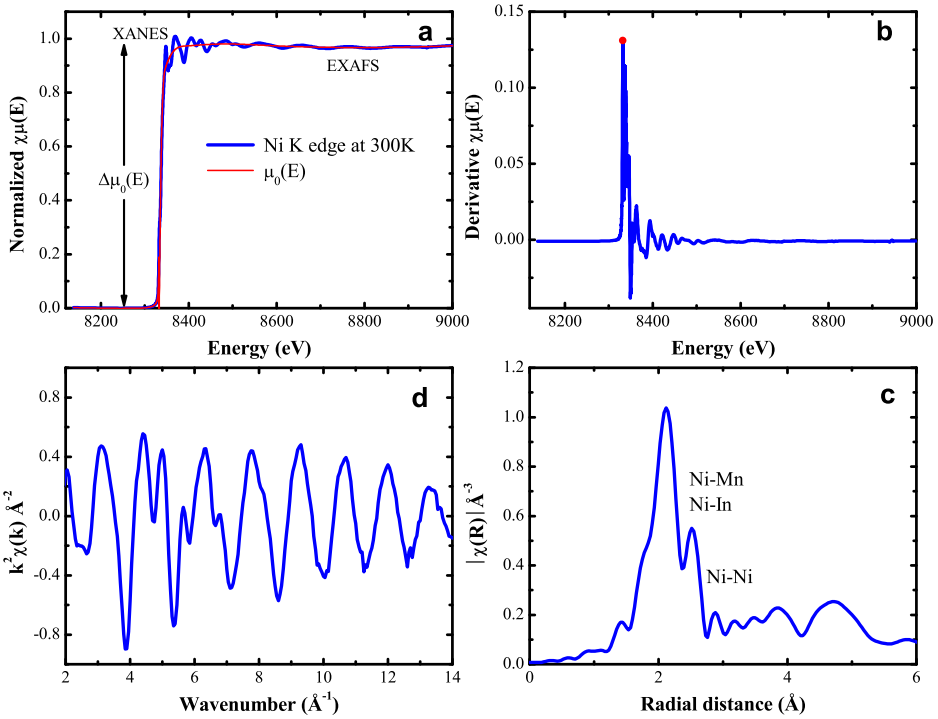

Figure 2.6: Basic steps carried out in the reduction of Ni_2MnIn Ni K edge XAFS data recorded at 300 K include: a. the subtraction and normalisation of background data, b. calibration of data to match the first inflection point (8332 eV) in Ni foil, c. k weighting of the XAFS data to amplify higher oscillations and d. identification of scattering contribution from different near neighbour shells.

Fig. 2.6 depicts the basic steps carried out in the reduction of Ni K edge XAFS data of Ni_2MnIn recorded at 300 K. The steps involved to carry out data reduction to $\chi(k)$ as described by the XAFS equation 2.28 are listed below,

1. Conversion of measured intensities to $\mu(E)$.

2. Subtraction of a smooth pre-edge function, to get rid of any instrumental background, and absorption from other edges.

3. Normalization of $\mu(E)$, so that it represents the absorption of one x-ray.

4. Removal of a smooth post-edge background function to approximate $\mu_0(E)$ to isolate

the XAFS χ.

5. Identification of the threshold energy E_0, and conversion from E to k space using the relation $k = \sqrt{\frac{2m(E-E_0)}{\hbar^2}}$.

6. Fourier transformation of the weighted XAFS $\chi(k)$ from k to R space.

7. Fourier filtering to isolate $\chi(k)$ for an individual shell.

After this procedure, scattering properties $f(k)$ and $\delta(k)$ can be modelled using computer program FEFF and analyze $\chi(k)$ to obtain the distance R and coordination number N.

In our study, the theoretical calculations were computed with ATOMS and FEFF8.4 programs[31] and the EXAFS data analysis were carried out using well established procedures in the Demeter software.[32]

References

[1] L. C. Chapon, P. Manuel, P. G. Radaelli, C. Benson, L. Perott, S. Ansell, D. D. D. S. E. N. J. Rhodes, and N. J.and Raspino. *Neutron News*, 22:22, 2011.

[2] J. M. Cowley. *Diffraction physics*. Amsterdam : North-Holland Pub.Co., New York : American Elsevier, 1975.

[3] V. Pecharsky and P. Zavalij. *Fundamentals of Diffraction*, pages 133–149. Springer US, Boston, MA, 2009.

[4] C. G. Shull and E. O. Wollan. *Science*, 108:69–75, 1948.

[5] M. K. Wilkinson, E. O. Wollan, and W. C. Koehler. *Annual Review of Nuclear Science*, 11:303–348, 1961.

[6] V. Petricek, M. Dusek, and L. Palatinus. *Z. Kristallogr.*, 229:345–352, 2014.

[7] A. Janner and T. Janssen. Symmetry of incommensurate crystal phases. i. incommensurate basic structure. *Acta Cryst*, A36:399–408, 1980.

[8] A. Janner and T. Janssen. Symmetry of incommensurate crystal phases. ii. incommensurate basic structure. *Acta Cryst*, A36:408–415, 1980.

[9] de Wolff P. M. The pseudo-symmetry of modulated crystal structures. *Acta Cryst*, A30:777–785, 1974.

[10] de Wolff P. M., Janssen T., and Janner A. The superspace groups for incommensurate crystal structures with a one-dimensional modulation. *Acta Cryst*, A37:625–636, 1981.

[11] L. Righi, F. Albertini, L. Pareti, A Paoluzi, and G. Calestani. *Acta Mater*, 55:5237–5244, 2007.

[12] L. Righi, F. Albertini, E. Villa, A. Paoluzi, G. Calestini, V. Chernenko, S. Besseghini, C. Ritter, and F. Passaratti. *Acta Mater*, 56:4529–4535, 2008.

[13] M. Dušek, V. Petříček, and L. Palatinus. *Journal of Physics: Conference Series*, 226:012014, 2010.

[14] A. V. Shubnikov and N. V. Belov. *Colored Symmetry.* Oxford:Pergamon Press, 1964.

[15] C. J. Bradley and A. P. Cracknell. *The Mathematical Theory of Symmetry in Solids.* Oxford: Clarendon, 1972.

[16] H. T. Stokes and D. M. Hatch. *Isotropy Subgroups of the 230 Crystallographic Space Group.* Singapore: World Scientific, 1987.

[17] W. G. Jenks, I. M. Thomas, and Jr. J. P. Wikswo. *Encyclopedia of Applied Physics*, 19, 1997.

[18] T. V. Duzer and C. W. Turner. *Principles of Superconductive Devices and Circuits,(Second Ed.)*. Prentice Hall PTR, Upper Saddle River, NJ, USA, 1999.

[19] J. Clarke. *Scientific American*, 271:46–53, 1994.

[20] C. Granata and A. Vettoliere. *Phys. Rep.*, 614:1–69, 2016.

[21] https://www.qdusa.com/sitedocs/appNotes/ppms/1078 201.

[22] http://przyrbwn.icm.edu.pl/APP/PDF/124/a124z6p12.

[23] https://www.ssi.shimadzu.com/sites/ssi.shimadzu.com/files/Products/literature/thermal/60 Series-Thermal-Analysis-Brochure-C160-E006N.pdf.

[24] W. Stark and W. Bohmeyer. *Non-Destructive Evaluation (NDE) of Polymer Matrix Composites*, pages 136–181. Woodhead Publishing.

[25] G. W. H. Höhne, W. F. Hemminger, and H.-J. Flammersheim. *Differential Scanning Calorimetry,(Second Ed.)*. Springer, Verlag, 2003.

[26] L. J. van der Pauw. *Philips Res. Rep.*, 16:187, 1961.

[27] http://www.tainstruments.com/pdf/brochure/dma.pdf.

[28] https://www.tainstruments.com/wp-content/uploads/Boston DMA-Training-2019.pdf.

[29] M. A. Meyers and Chawla K. K. *Mechanical Behavior of Materials*. Prentice-Hall, 1999.

[30] M. Newville. Fundamentals of xafs. *Consortium for Advanced Radiation Sources, University of Chicago (USA)*, 78, 2004.

[31] J. J. Rehr, J. J. Kas, M. P. Prange, A. P. Sorini, Y. Takimoto, and F. D. Vila. *Comptes Rendus Physique*, 10:548–559, 2009.

[32] B. Ravel and M. Newville. *J Synchrotron Radiat*, 12:537, 2005.

Chapter 3

Understanding the nature of structural defects leading to strain glassy transition in Ni rich NiTi alloys

3.1 Introduction

NiTi is a binary alloy undergoing a martensitic transition from B2 to B19' near room temperature.[1] Recent studies have shown that the addition of impurity elements including Ni itself disturbs the long range ordering of the elastic strain vector resulting in strain glass transition.[2–4] Interestingly, when Ni is doped at the expense of Ti to realize $Ni_{50+x}Ti_{50-x}$, an addition of a small concentration of $\sim 2\%$ excess Ni impurity drives the system into a nonergodic state. This observation intensifies the need to identify the nature of structural defects responsible for glassy dynamics. Since invariance of crystal structure is one of the characteristics of strain glass transition, critical knowledge of the evolution of short range structural order is required.

Latterly, studies suggest the presence of incommensurate reflections below glass transition temperature in in-situ high resolution electron microscopy (HREM), on TiPd alloys

doped with Cr, indicating the ground state to be an inhomogeneous distribution of nano-sized domains with modulated structure.[5] Further, a decisive role of Ni atoms as point defects has been revealed in the mechanism of strain glass transition in $Ni_{51.3}Ti_{48.7}$ through in-situ anomalous small-angle x-ray scattering (ASAXS)technique. The study reports the distribution of Ni atoms as nanodomains comprising of a disk like core-shell configuration with a Ni-rich shell and a highly Ni-rich core.[6] Nonetheless, the nature of structural defects and the invariance of the crystal structure, despite the presence of martensitic domains is yet to be understood. In order to achieve this objective, an attempt is made to investigate $Ni_{50+x}Ti_{50-x}$ alloys through extended x-ray absorption fine structure (EXAFS) technique to understand the structural distortions around the absorbing atom due to impurity addition. The initial part of the chapter focuses on various characterization methods which reveal that with the average structure remaining invariant, the martensitic transition is suppressed in the composition $x = 0.2$. These results propel the investigation of the local structure which is discussed in detail in the later half of the chapter.

3.2 Results

3.2.1 Structure

The nominal and the actual composition of the four alloys as obtained from SEM-EDX is provided in table 3.1. The x-ray diffraction data recorded at 300 K on the powdered alloys is displayed in Fig.3.1. The phases are identified using the LeBail method. All four alloy compositions exhibit a major cubic B2 phase. A minor fraction of ~ 9 % B19'

Table 3.1: The nominal and the actual compositions as obtained from the SEM-EDEX measurements within the error bar of 3%.

Nominal compositions	**Actual compositions**
$Ni_{50}Ti_{50}$	$Ni_{52.06}Ti_{47.96}$
$Ni_{52}Ti_{48}$	$Ni_{54.82}Ti_{45.18}$
$Ni_{55}Ti_{45}$	$Ni_{57.53}Ti_{42.47}$
$Ni_{60}Ti_{40}$	$Ni_{60.61}Ti_{39.39}$

phase is seen in the alloy $Ni_{50}Ti_{50}$ while about 6% anatase TiO_2 is witnessed in $Ni_{55}Ti_{45}$. Moreover, $\sim$ 20% of face-centered cubic (FCC) Ni metal segregates in the alloy $Ni_{60}Ti_{40}$ as impurity phase. A decrease in lattice constant with an increase in Ni concentration is seen as evidenced by the variation of the (101) Bragg reflection presented in Fig.3.1. There is an increase in full-width at half-maximum (FWHM) of the (101) Bragg peak from $Ni_{50}Ti_{50}$ to $Ni_{55}Ti_{45}$ with a slight decrease in $Ni_{60}Ti_{40}$. An increase in the width of the peak implies a strain build up finally resulting in the separation of fcc Ni metal phase from the cubic B2 phase accompanied by a reduction in the FWHM of the Bragg peaks in $Ni_{60}Ti_{40}$.

3.2.2 Mechanical, thermal and transport properties

Fig.3.2 displays differential scanning calorimetry (DSC) and resistivity plots for the alloys. Martensitic transition is seen in the alloy $Ni_{50}Ti_{50}$ with a martensitic start temperature M_S at around 330 K. This alloy exhibit a transformation hysteresis region extending from martensitic finish temperature $M_F = 280$ K to austenitic finish temperature $A_F = 350$ K. This is a possible explanation for the appearance of relatively broad diffraction

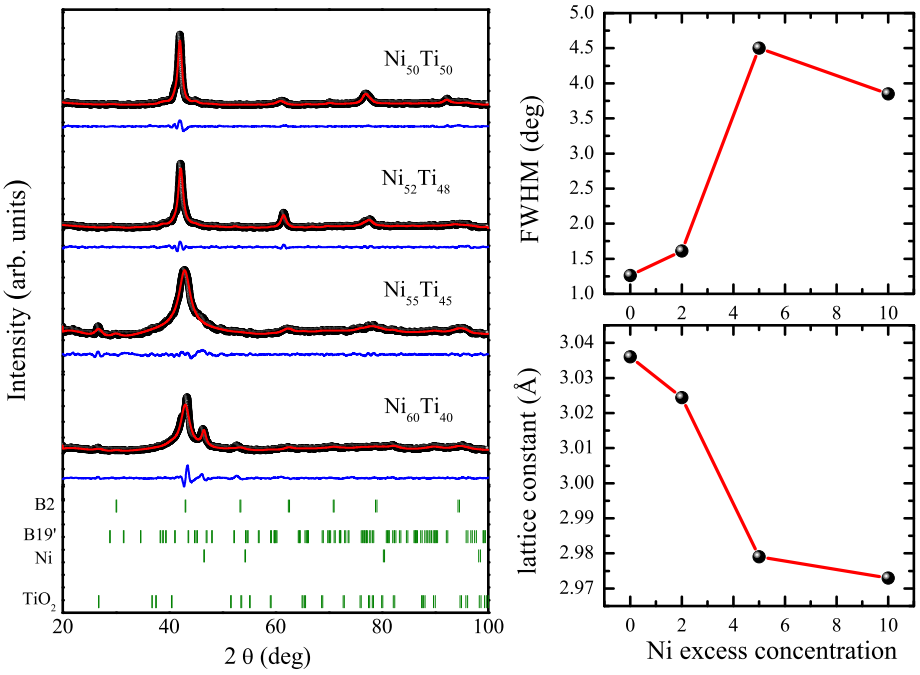

Figure 3.1: X ray diffraction data at room temperature analyzed using LeBail method. With increase in the Ni excess content x, there is an increase in the full width half maximum of the (101) Bragg peak signifying build up of strain along with a decrease in lattice constant.

peaks and B19' phase seen in the x-ray diffraction pattern at 300 K. The other three alloys do not show a martensitic transition in either DSC measurements performed down to 150 K or resistivity measurements recorded down to 50 K. On the contrary, a broad hump below 200 K is witnessed in the resistivity measurements moving towards lower temperatures with Ni excess concentration. An increase in scattering due to Ni impurity doping appears to escalate the resistivity with excess Ni content more evidently visible in the alloy $Ni_{60}Ti_{40}$.

The variation of storage modulus and loss ($\tan\delta$) with temperature at different frequencies is shown in the Fig.3.3 for the alloy compositions $Ni_{50}Ti_{50}$ and $Ni_{52}Ti_{48}$. Martensitic transition is seen in the alloy $Ni_{50}Ti_{50}$ as indicated by the dip in storage modulus and a

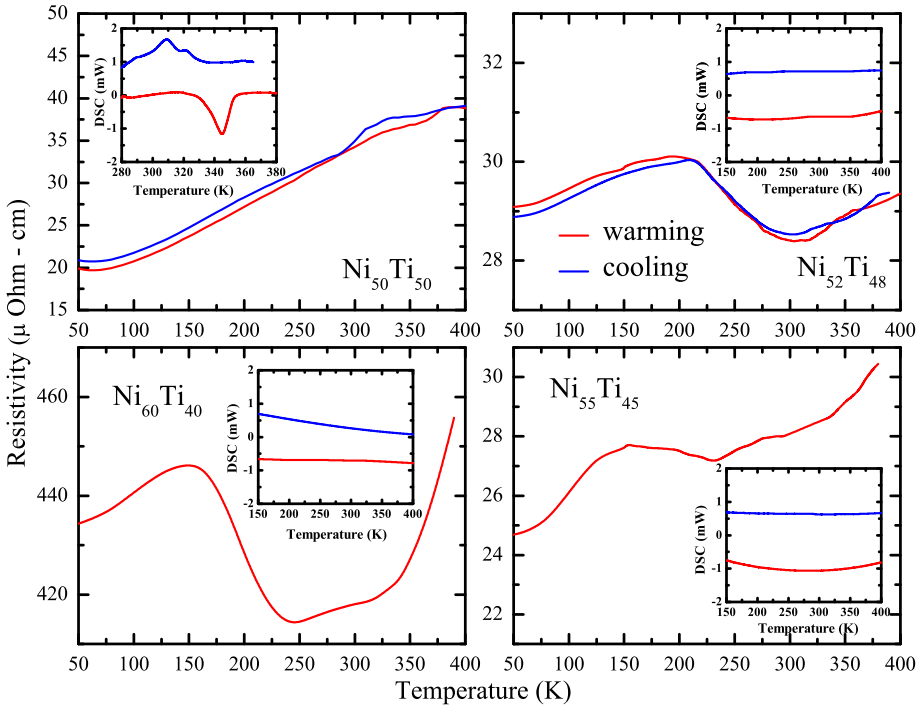

Figure 3.2: The resistivity and the dsc (shown as insets) plots for all the four alloy compositions. Martensitic transition is observed in the alloy $Ni_{50}Ti_{50}$ just above 300 K which is not seen in the other alloys in the temperature range of 50 K to 400 K.

peak in the loss. The dip and peak temperatures of the two respective signals are present within the temperature range obtained from the transport property measurements. The strain glass transition is noticed in the alloy $Ni_{52}Ti_{48}$ as evidenced by the broad humps in the storage modulus and loss signals at around 200 K, displaying frequency dependence following the Vogel-Fulcher relationship. The DMA measurements did not show any features in the other two alloy compositions $Ni_{55}Ti_{45}$ and $Ni_{60}Ti_{40}$ down to 150 K.

3.2.3 EXAFS calculations

To understand the interatomic interactions driving the glassy transition, local structural studies were performed using the EXAFS technique at the Ni and Ti K edges. Analysis

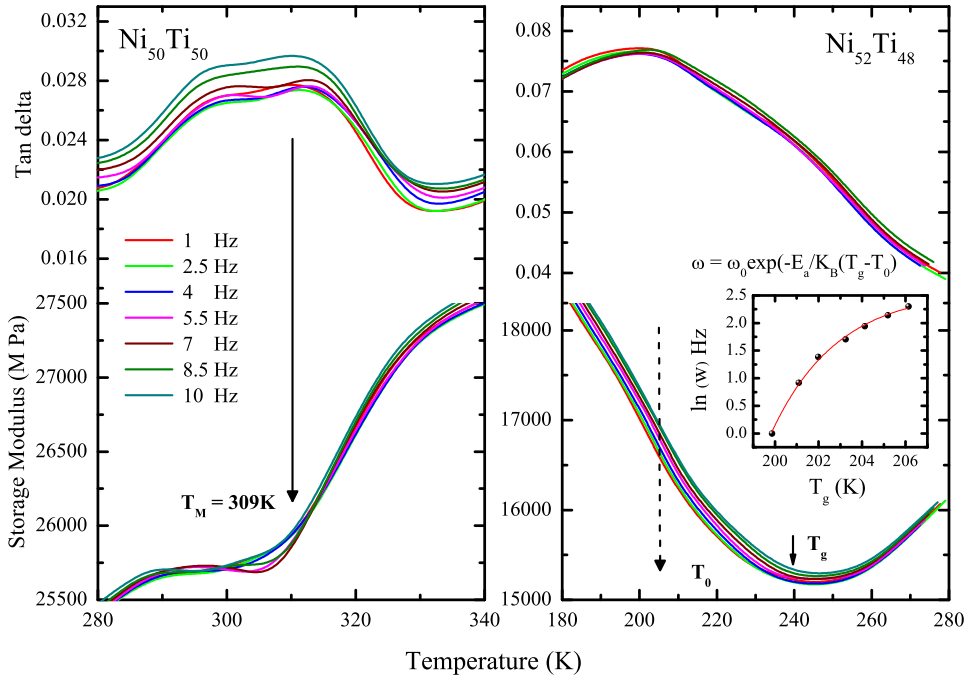

Figure 3.3: The variation of storage modulus and loss at multiple frequencies as a function of temperature in the alloys $Ni_{50}Ti_{50}$ and $Ni_{52}Ti_{48}$. The inset shows the frequency dependence at glass transition following Vogel Fulcher relation in $Ni_{52}Ti_{48}$.

was performed by fitting both the Ni K and Ti K edges together with a common structural model based on the crystal structure. However, this approach achieved a reasonably good fit only for the stoichiometric $Ni_{50}Ti_{50}$, while discrepancies were noticed in other alloy compositions. Hence, ab initio calculations of the EXAFS signals at Ni K and Ti K edges were employed using FEFF 8.4 for all the possible phases including austenitic (B2), the martensitic (B19'), the R phase, and for phases like Ni_3Ti and pure Ni metal to confirm the correct structural model. These calculated spectra $\chi(k)$ were then compared with the respective experimental data recorded at 77 K in all the alloy compositions.

The k weighted EXAFS data in all the four alloy compositions along with the theo-

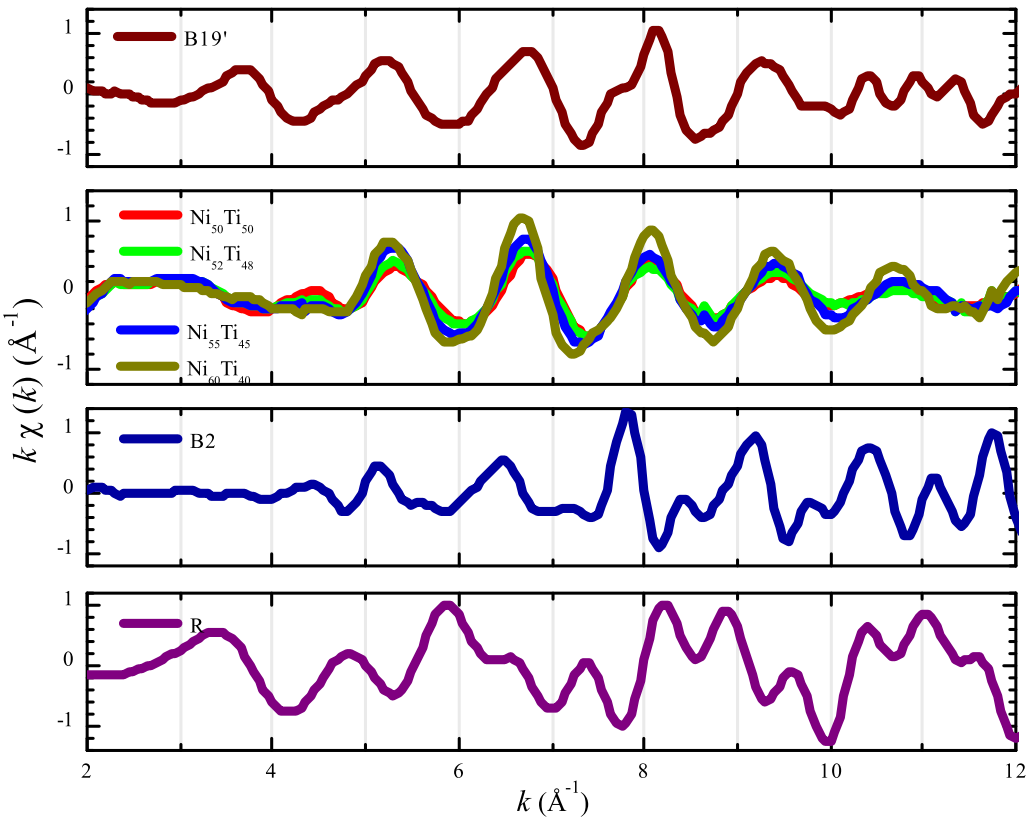

Figure 3.4: The Ti edge k-weighted EXAFS spectra recorded at 77 K compared with the theoretically calculated spectra of the structures B19′, B2 and R. A good resemblance to B19′ phase is seen in all the four alloy compositions over B2 or R phases.

retically calculated spectra at Ti edge are presented in Fig.3.4. All the alloy compositions display similar EXAFS oscillations but with an increase in magnitude with increasing Ni content. The experimental spectra show a good resemblance with the calculated B19' structure over B2 or R structures. This is expected for the alloy $Ni_{50}Ti_{50}$, as it is in its martensitic state at 77 K. However, for all the other Ni excess compositions, this implies a modulated local structure around the Ti atom. Fig.3.5 presents the k weighted EXAFS spectra at Ni edge for the first three alloy compositions $0 \leq x \leq 5$ displaying fairly identical EXAFS oscillations with the enhancement in amplitude with excess Ni content.

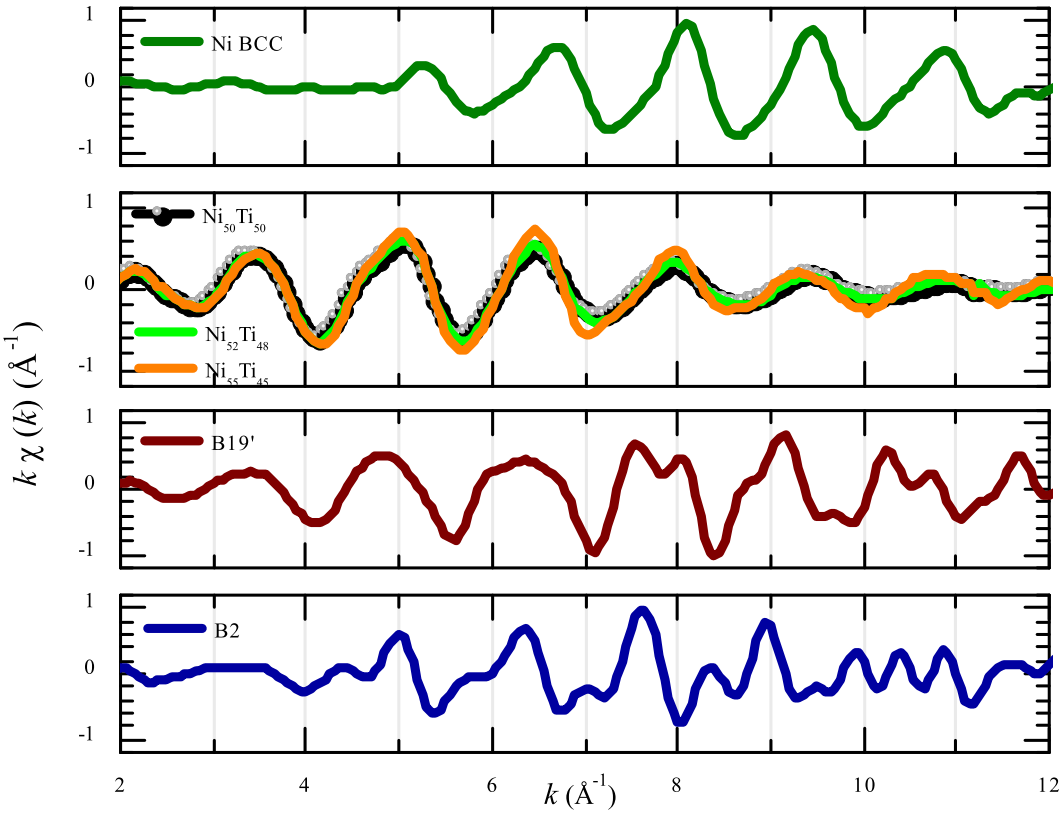

Figure 3.5: The Ni edge k-weighted EXAFS spectra of the alloys $Ni_{50}Ti_{50}$, $Ni_{52}Ti_{48}$ and $Ni_{55}Ti_{45}$ at 77 K compared with B2 and B19′ phases of the NiTi alloy and Ni BCC metal phase. The Ni local structure is best described as a combination of B19′ phase and Ni BCC in all the three alloy compositions.

A careful comparison of the experimental and the calculated spectra reveals analogous behaviour with the B19' structure below 7 $Å^{-1}$ above which discrepancy is noticed. Interestingly, similarities are seen with the body-centered (bcc) Ni structure[7] particularly in the region $k > 6$ $Å^{-1}$. In the B2 or B19' structures of NiTi, the Ni atom is surrounded by 8 Ti atoms in the first coordination whereas in the bcc Ni phase the nearest neighbors are Ni atoms themselves. This change in the nearest neighbor atom from Ti (Z = 22) to Ni (Z = 28) shifts the back-scattering amplitude maximum from $\sim$ 5.5 to about 7 $Å^{-1}$.[8,9]

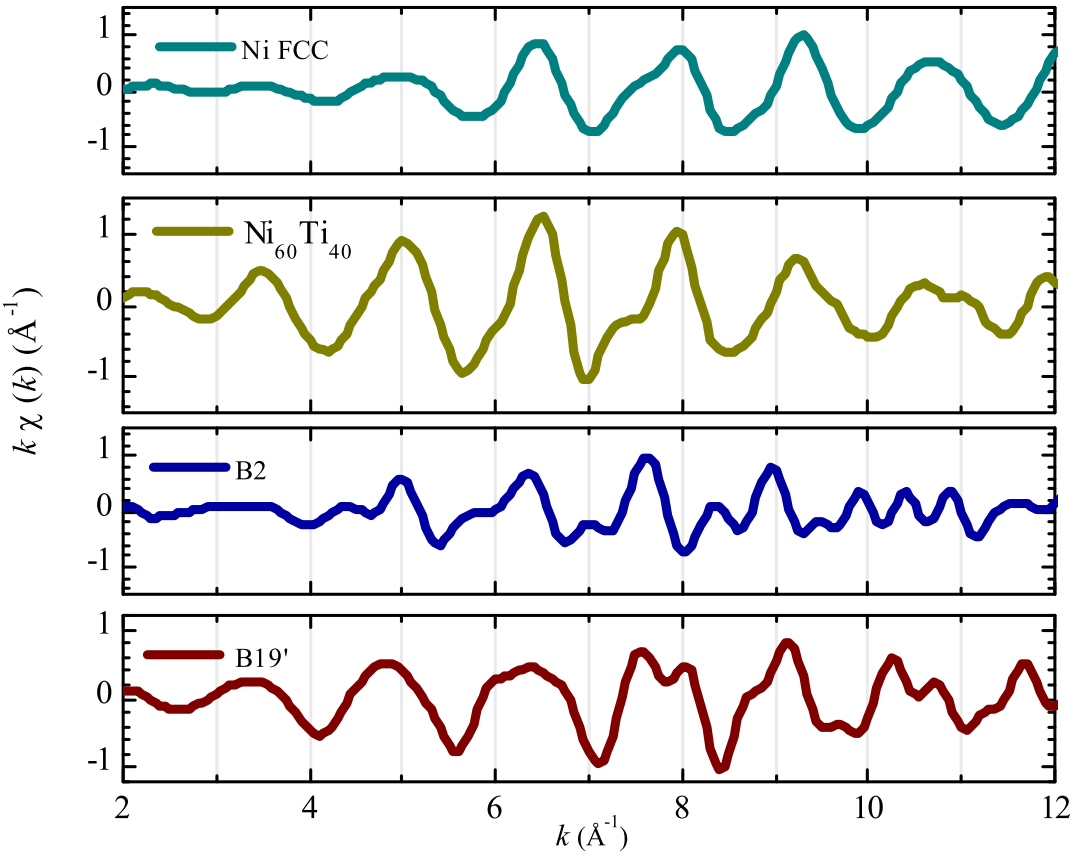

Figure 3.6: The Ni edge k-weighted EXAFS spectra of $Ni_{60}Ti_{40}$ at 77 K compared with the B2 and B19′ phases of the NiTi alloy and Ni FCC metal phase indicating a combination of B2 phase and Ni FCC metal phase to be favorable solution.

These results indicate that the Ni local structure in the alloys $0 \leq x \leq 5$ is a combination of B19' and Ni bcc phase. The Ti EXAFS matches with the calculated B19' spectra while Ni EXAFS is equivalent to the sum of calculated B19' and bcc Ni spectra.

The situation is slightly different in the alloy $Ni_{60}Ti_{40}$ as depicted in Fig.3.6. While the Ti local structure is B19', the x-ray diffraction has shown the presence of face centered cubic (FCC) Ni metal phase due to which the presence of this phase in Ni EXAFS spectra is inevitable. Interestingly, the Ni local structure in $Ni_{60}Ti_{40}$ carries an essence of the B2

phase, unlike the other three alloy compositions that have more similarities with the B19' phase. Hence, in the alloys $Ni_{50+x}Ti_{50-x}$, the Ni local structure is different from that of Ti and evolves from a sum of B19' and bcc Ni phases to a mixture of B2 and fcc Ni phases with increasing x.

3.2.4 EXAFS fittings

The fitting of EXAFS spectra at the Ni K and Ti K edges in $Ni_{50+x}Ti_{50-x}$ were carried out using the structural models adapted based on the above comparison. Nine independent parameters consisting of correction to the bond length ΔR and mean square variation in bond length σ^2 were used for each of the scattering paths to fit the spectra at both the edges. The crystal structure reported in[7,10,11] was used to derive the structural model to obtain the coordination numbers of the individual scattering paths. The amplitude reduction factor S_0^2 and correction to edge energy ΔE_0 were achieved from the analysis of the standard metal spectra and were kept fixed throughout the analysis. Further, during the analysis of Ni EXAFS spectra, one more independent parameter y was introduced to estimate the fraction of the two phases NiTi and Ni metal phase.

In all the alloy compositions, the correlations from B19' phase were used to obtain the best fits to the Ti local structure. The magnitude of Fourier transform (FT) of the Ti EXAFS spectra includes contributions from four coordination shells, two with Ni atoms at $\sim$ 2.52 and $\sim$ 2.60 Å and two with Ti atoms at $\sim$ 2.88 and $\sim$ 2.99 Å , respectively. Fig.3.7 presents the experimental EXAFS data along with best fits at 300 and 77 K while the values of the bond distances and the mean square displacements in the four near

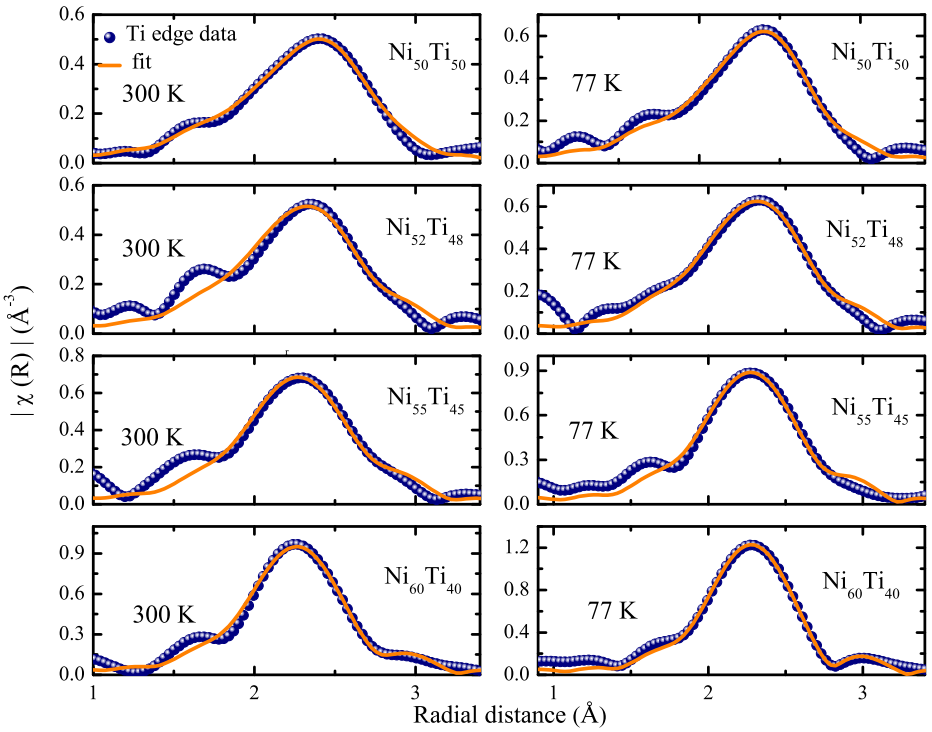

Figure 3.7: The magnitude of Fourier transform spectra at Ti edge for the four alloy compositions at 300 K and 77 K.

neighbour bonds are given in table 3.2. No significant changes are observed in the Ti-Ni and Ti-Ti bond distances either with temperature or with a change in Ni concentration. The fittings affirm the local structure of Ti to be like that of B19' phase which does not change with Ni doping.

Since the comparisons of the experimental data with the theoretically calculated spectra indicated contribution from more than one phase in Ni local structure, the spectra in the alloys $0 \leq x \leq 5$ were fitted with two different combinations. In the first case correlations from B2 and BCC, Ni phase were considered while in the second case correlations from B19' and BCC Ni phase were included. The presence of $\sim 6 \pm 1\%$ of the BCC Ni phase was observed even in the stoichiometric $x = 0$ composition which is in agreement

Table 3.2: The results of the best fits obtained at 300 K and 77 K for the four alloy compositions at Ti edge carried out in the k-range 3-12 Å^{-1}, k weighted at 2 and in R-range 1-3 Å. The bond length is given by the parameter R while the thermal variation in bond length is described by σ^2. Figures in parenthesis indicate uncertainty in last digit.

Alloys	**Atoms with coordination no.**	**300 K** R(Å)	σ^2 (Å^2)	**77 K** R(Å)	σ^2 (Å^2)
$Ni_{50}Ti_{50}$	Ni1×3	2.49(1)	0.0175(8)	2.49(1)	0.016(1)
	Ni2×4	2.58(1)	0.0175(8)	2.58(1)	0.016(1)
	Ti1×2	2.86(2)	0.004(1)	2.86(2)	0.002(2)
	Ti2×2	3.00(2)	0.005(2)	3.00(3)	0.004(2)
$Ni_{52}Ti_{48}$	Ni1×3	2.49(3)	0.017(2)	2.49(2)	0.015(1)
	Ni2×4	2.58(3)	0.017(2)	2.58(2)	0.015(1)
	Ti1×2	2.88(4)	0.005(4)	2.87(2)	0.004(3)
	Ti2×2	3.03(6)	0.008(5)	3.02(4)	0.007(4)
$Ni_{55}Ti_{45}$	Ni1×3	2.49(3)	0.013(2)	2.49(3)	0.011(2)
	Ni2×4	2.58(3)	0.013(2)	2.58(3)	0.011(2)
	Ti1×2	2.88(3)	0.004(3)	2.88(3)	0.003(3)
	Ti2×2	3.04(6)	0.007(5)	3.04(3)	0.005(5)
$Ni_{60}Ti_{40}$	Ni1×3	2.496(6)	0.0104(8)	2.51(2)	0.008(1)
	Ni2×4	2.584(6)	0.0104(8)	2.59(2)	0.008(1)
	Ti1×2	2.89(1)	0.004(2)	2.90(1)	0.003(2)
	Ti2×2	3.07(3)	0.009(5)	3.09(3)	0.010(4)

with the slightly higher Ni content estimated from SEM-EDX (table 3.1). Contributions from the near neighbor correlations consisting of Ti at $\sim$ 2.52 Å, and at $\sim$ 2.60 Å, Ni at $\sim$ 2.61 Å and $\sim$ 2.84 Å from the B19′ phase and a Ni–Ni scattering path at $\sim$ 2.44 Å from the BCC Ni metal phase were employed to achieve the best fits to the experimental spectra. The second scattering path from the BCC Ni metal phase (2.82 Å) was masked by the Ni–Ni scattering path at 2.84 Å from B19′ phase. In the alloy $x = 10$, the Ni EXAFS fittings were performed by including correlations from B2 and FCC Ni or B19′ and FCC Ni phases. The scattering paths, Ni–Ti (2.61 Å) and Ni–Ni (3.02 Å) from B2 phase and Ni–Ni at 2.51 Å and 3.54 Å from the FCC Ni phase were used to obtain the

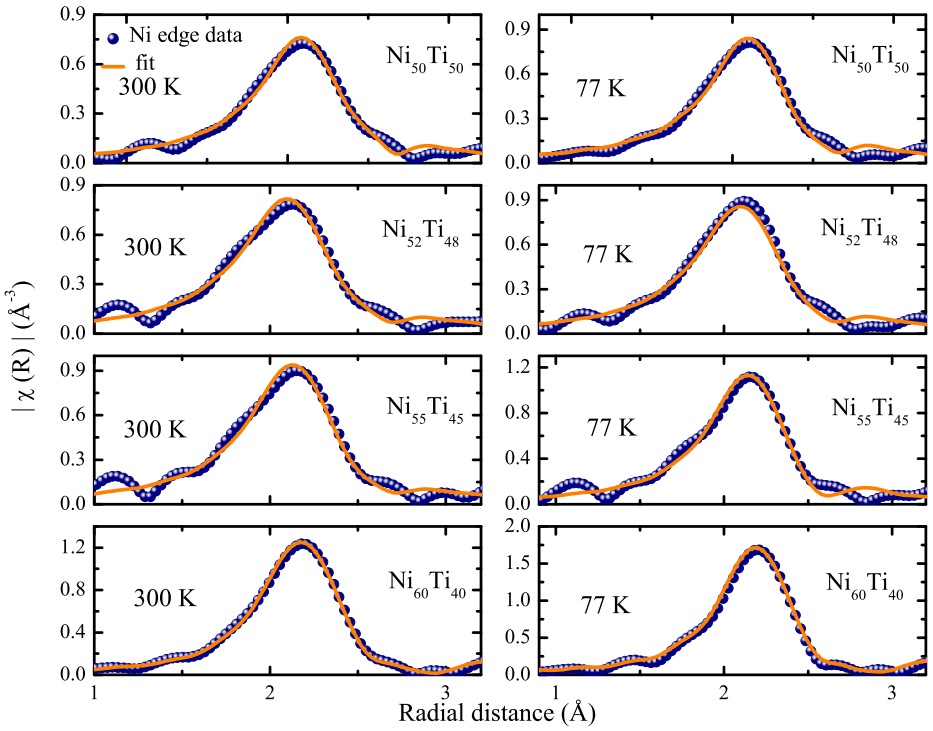

Figure 3.8: The magnitude of Fourier transform spectra at Ni edge for the four alloy compositions at 300 K and 77 K.

best fits. The experimental EXAFS data along with best fits at 300 and 77 K is presented in Fig.3.8 while the values of the bond distances and the mean square displacements in the four near neighbour bond are given in table 3.3.

3.3 Discussion

Through local structural study, an attempt has been made to understand the structural changes leading to the strain glassy phase in martensite. Our analysis reveals that with the increase in doping of excess Ni, the Ni local structure evolves from a combination of B19′ and BCC Ni to a mixture of B2 and FCC Ni metal phase while the Ti local structure remains consistent with the B19′ phase. The mean square radial distance (σ^2) of Ti–Ni

Table 3.3: The results of the best fits obtained at 300 K and 77 K for the four alloy compositions at Ni edge carried out in the k-range 3-12 Å^{-1}, k weighted at 2 and in R-range 1-3.5 Å. The bond length is given by the parameter R while the thermal variation in bond length is described by σ^2. Figures in parenthesis indicate uncertainty in last digit.

Alloys	**Atoms with coordination no.**	**300 K** R(Å)	σ^2 (Å^2)	**77 K** R(Å)	σ^2 (Å^2)
$Ni_{50}Ti_{50}$	Ti1×3	2.51(3)	0.032(2)	2.51(3)	0.032(2)
	Ti2×4	2.60(3)	0.032(2)	2.60(3)	0.032(2)
	Ni1×2	2.63(3)	0.017(3)	2.61(3)	0.017(3)
	Ni2×2	2.90(3)	0.017(3)	2.88(3)	0.017(3)
	Ni1×8 (Ni BCC)	2.45(1)	0.007(2)	2.45(1)	0.007(2)
$Ni_{52}Ti_{48}$	Ti1×3	2.51(5)	0.031(2)	2.51(4)	0.031(2)
	Ti2×4	2.60(5)	0.031(2)	2.60(4)	0.031(2)
	Ni1×2	2.63(5)	0.018(6)	2.61(4)	0.018(5)
	Ni2×2	2.90(5)	0.018(6)	2.88(4)	0.018(5)
	Ni1×8 (Ni BCC)	2.461(8)	0.008(2)	2.464(6)	0.007(7)
$Ni_{55}Ti_{45}$	Ti1×3	2.52(6)	0.032(3)	2.52(6)	0.031(3)
	Ti2×4	2.61(6)	0.032(3)	2.60(6)	0.031(3)
	Ni1×2	2.63(7)	0.019(8)	2.62(6)	0.019(8)
	Ni2×2	2.90(7)	0.019(8)	2.89(6)	0.019(8)
	Ni1×8 (Ni BCC)	2.481(8)	0.008(2)	2.482(7)	0.0073(8)
$Ni_{60}Ti_{40}$	Ti1×8	2.64(2)	0.046(2)	2.63(8)	0.036(4)
	Ni1×6	3.11(5)	0.048(9)	3.01(8)	0.030(9)
	Ni1×12 (Ni FCC)	2.513(2)	0.0083(5)	2.514(3)	0.0063(4)
	Ni2×6 (Ni FCC)	3.54(2)	0.015(3)	3.57(3)	0.012(4)

(Ti absorber) and Ni–Ti (Ni absorber) bonds illustrates the above disparity in the local structures of Ni and Ti. Ni carries a larger disorder around itself in comparison with Ti as indicated by the higher σ^2 of Ni–Ti ($\sim$ 0.03 Å^2) than Ti–Ni ($\sim$ 0.01 Å^2) bonds in all the alloy composition. This disorder around Ni is caused by defects formed due to the presence of BCC Ni clusters in all the Ni excess compositions. This argument is further supported by the increase in the resistivity seen with increasing x in $Ni_{50+x}Ti_{50-x}$. This is because defects result in increased scattering of free charge carriers and hence a higher resistivity.

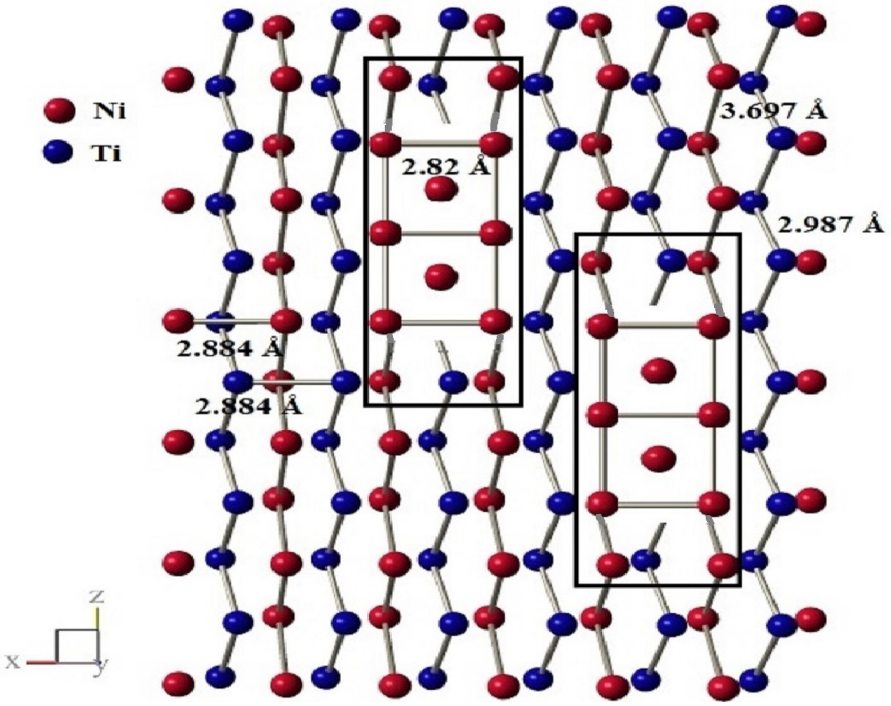

Figure 3.9: Structural distortion in B19′ structure because of the presence of impurity Ni BCC clusters seen in ball and stick model.

As Ni atoms progressively replace Ti atoms, Ni-Ni nearest neighbour pairs are formed leading to the growth of Ni BCC clusters as seen in the rectangular regions in Fig. 3.9. These Ni–Ni pairs then influence the next nearest Ni–Ni bond distances in the B19′ phase at $\sim$ 2.884 Å to 2.82 Å causing its contraction and a structural defect. The presence of such structural defects forces the crystal structure to retain B2 symmetry even as the NiTi grain undergoes a martensitic transformation. As Ni excess concentration further increases, these defects grow in size leading to the possibility of the formation of pure Ni clusters. At this stage, the minimization of free energy demands a conversion of BCC Ni to FCC Ni. The strain caused by the presence of larger size defects is perhaps responsible for a change in the Ni local structure from B19′ to B2 type in $Ni_{60}Ti_{40}$ alloy. The formation

of BCC Ni defects and the associated decrease in the Ni–Ni bond length of B19′ phase explains the increase in FWHM of Bragg peaks and the decrease in the lattice constant with an increase in excess Ni concentration. The random distribution of Ni clusters breaks the long range ordering of the elastic strain vector, causing a martensitic composition to transform to a strain glassy phase.

3.4 Conclusion

In conclusion, the study on $Ni_{50+x}Ti_{50-x}$ alloys is primarily aimed at understanding the local structural changes through EXAFS as the ground state transit from martensite to strain glass. With the doping of impurity Ni atoms at the expense of Ti, Ni BCC clusters are formed which segregate as a defect phase within the B19′ martensitic clusters of $Ni_{50}Ti_{50}$. As the concentration of the excess Ni increases, there is a structural change from Ni BCC to Ni FCC due to the growth of nearest neighbor Ni–Ni correlations. However, the core structure of the parent NiTi phase remains unaffected as evidenced by the unchanged Ti local structure throughout the doping region. The presence of BCC Ni clusters obstructs the propagation of long range ordering of the elastic strain vector, thereby leading to a transformation from a martensitic state to a strain glassy state.

References

[1] K. Otsuka and X. Ren. *Prog. Mater. Sci.*, 50:511, 2005.

[2] S. Sarkar, Xiaobing Ren, and K. Otsuka. *Phy. Rev. Lett.*, 95:205702, 2005.

[3] D. Wang, Z. Zhang, J. Zhang, Y. Zhou, Y. Wang, X. Ding, Y. Wang, and X. Ren. *Acta Mater*, 58:6206–6215, 2010.

[4] Y. Zhou, D. Xue, X. Ding, Y. Wang, J. Zhang, Z. Zhang, D. Wang, K. Otsuka, J. Sun, and Xiaobing Ren. *Acta Mater*, 58:5433–5442, 2010.

[5] Y. Zhou, D. Xue, Y. Tian, X. Ding, S. Guo, K. Otsuka, J. Sun, and X. Ren. *Phys. Rev. Lett.*, 112:025701, 2014.

[6] Yung-Chien Huang, Cheng-Si Tsao, and Shyi-Kaan Wu. *Scientific Reports*, 10:1–11, 2020.

[7] C. Tian, D. Qian, D. Wu, R. He, Y. Wu, W. Tang, L. Yin, Y. S. Shi, G. Dong, X. Jin, X. Jiang, F. Liu, H. Qian, K. Sun, L. Wang, G. Rossi, Z. Qiu, and J. Shi. *Phys. Rev. Lett.*, 94:137210, 2005.

[8] A. G. McKale, B. W. Veal, A. P. Paulikas, S. K. Chan, and G. S. Knapp. *J. Am. Chem. Soc.*, 110(12):3763–3768, 1988.

[9] J. J. Rehr and R. C. Albers. *Rev. Mod. Phys.*, 72:621, 2000.

[10] H. Sitepu, W. W. Schmahl, and J. K. Stalick. *Appl. Phys. A.*, 74:1719, 2002.

[11] E. A. Owen and E. L. Yates. *Phil. Mag.*, 21:809, 1936.

Chapter 4

Effect of Fe doping in the martensitic alloy $Ni_2Mn_{1.5}In_{0.5}$

4.1 Introduction

The strain glass phase reportedly occurs in all ferroelastic/martensitic alloys beyond a critical dopant concentration.[1] Recently the structural glass is also reported in Heusler type alloy in $Ni_{55-x}Co_xFe_{18}Ga_{27}$ at a critical Co level of 10%.[2] The martensitic transition in Heusler alloys is predominantly controlled by the addition of impurities. In such Ni–Mn–Z (Z = In, Sn, Sb) alloys, the structural transformation from cubic $L2_1$ austenite to lower symmetry martensite or vice-versa occurs when the dopant concentration exceeds a critical value. This is also associated with the alteration of magnetic ground state from ferromagnetic to non-magnetic/antiferromagntic.[3,4]

Fe doping in martensitic Ni-Mn-In alloys causes the suppression of martensitic transition temperature T_M and strengthening of ferromagnetic interactions.[5,6] The suppression is rather rapid and is explained to be due to the destruction of Mn-Ni-Mn antiferromagnetic interactions and formation of Fe-Fe ferromagnetic interactions as a result of site occupancy disorder.[6] In some cases, Fe addition to NiMn type alloys results in an emer-

gence of structural impurity phases.[6–9] The question then arises as to whether Fe doping in martensitic Ni-Mn-In alloys also results in impeding long range ordering of the elastic strain vector and formation of the strain glass phase similar to the one observed in Ni doped NiTi alloys. Further, in an X_2YZ Heusler alloy, the site symmetry of the X site ($\bar{4}3m$) is different from that of Y and Z sites ($m\bar{3}m$), and this difference is known to affect structural and magnetic interactions. Therefore, it would be interesting to explore the effect of site occupancy on the occurrence of strain glassy phase in Heusler alloys.

In order to achieve these objectives, we have studied the effect of Fe doping on the alloy $Ni_2Mn_{1.5}In_{0.5}$ that undergoes martensitic transition at around 425 K. A careful analysis is carried out by doping Fe at the expense of Mn and Ni to realize $Ni_2Mn_{1.5-x}Fe_xIn_{0.5}$, $0 \leqslant x \leqslant 0.2$ and $Ni_{2-y}Fe_yMn_{1.5}In_{0.5}$, $0 \leqslant y \leqslant 0.2$ respectively which is detailed in this chapter.

4.2 Results

4.2.1 Structure : X-ray diffraction studies

Fig.4.1 and Fig.4.2 depicts the x ray diffraction patterns at 300 K when Fe is doped at the expense of Mn or Ni respectively. In the series $Ni_2Mn_{1.5-x}Fe_xIn_{0.5}$, the modulated monoclinic martensitic structure of the parent alloy $Ni_2Mn_{1.5}In_{0.5}$ persists in the Fe doped alloys upto $x = 0.1$ (Fig.4.1 a - c). A further increase in Fe ($x = 0.2$) leads to a structural change from martensitic to a biphasic composition consisting of major $L2_1$ and a minor impurity phase (Fig.4.1 d). The additional Bragg peaks of the impurity phase can be

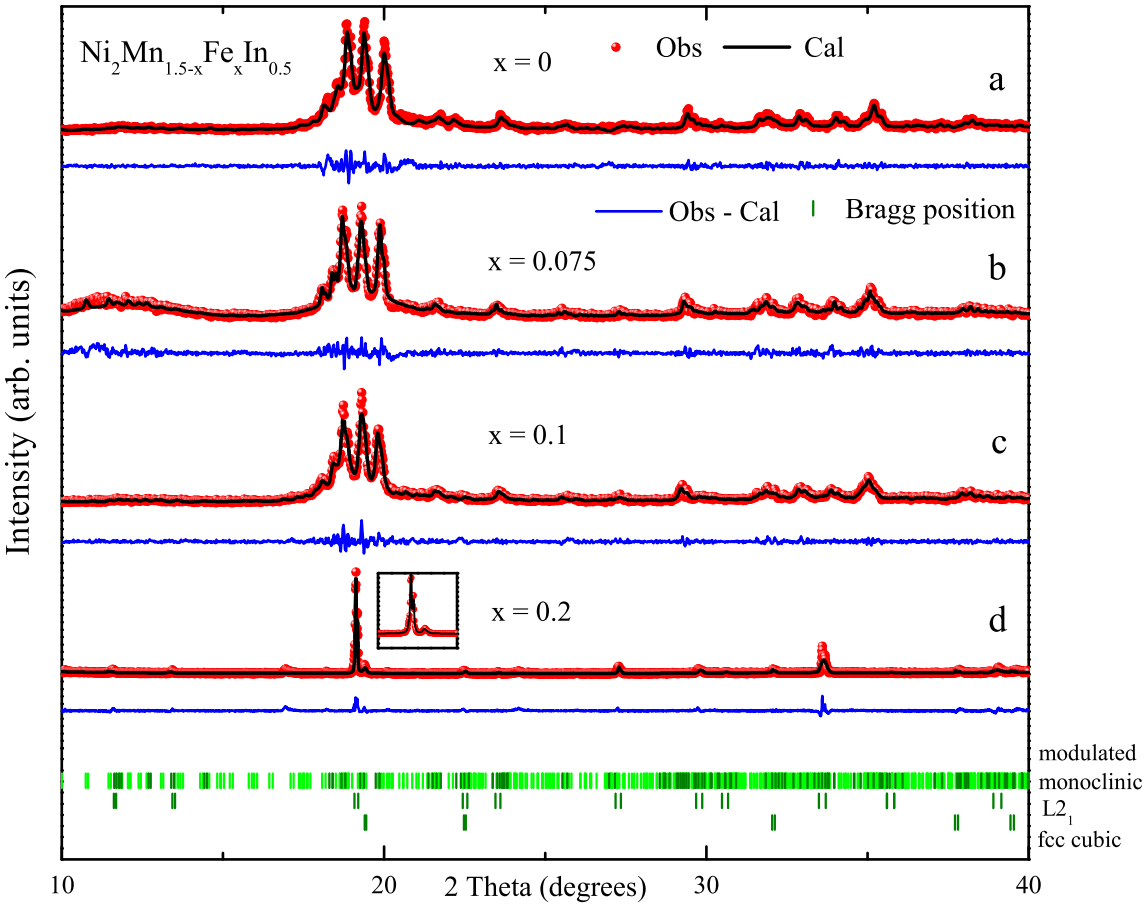

Figure 4.1: The LeBail refined x-ray diffraction data at 300 K for the series $Ni_2Mn_{1.5-x}Fe_xIn_{0.5}$. Inset highlights the presence of minor fcc cubic phase seen in the alloy x = d.

fitted to a face centred cubic (fcc) phase identified later as $\gamma-$(Fe,Ni) phase. In the second series $Ni_{2-y}Fe_yMn_{1.5}In_{0.5}$, the modulated phase is converted to a cubic Heusler phase with the increase in Fe concentration from $y = 0.1$ to $y = 0.2$ (Fig.4.2 b and c). The refinement results are summarized in Table 4.1.

4.2.2 Thermal, transport, mechanical and magnetic properties

The austenite to martensite transition temperature is determined through DSC measurements presented in Fig.4.3. The transition is characterized by the existence of the

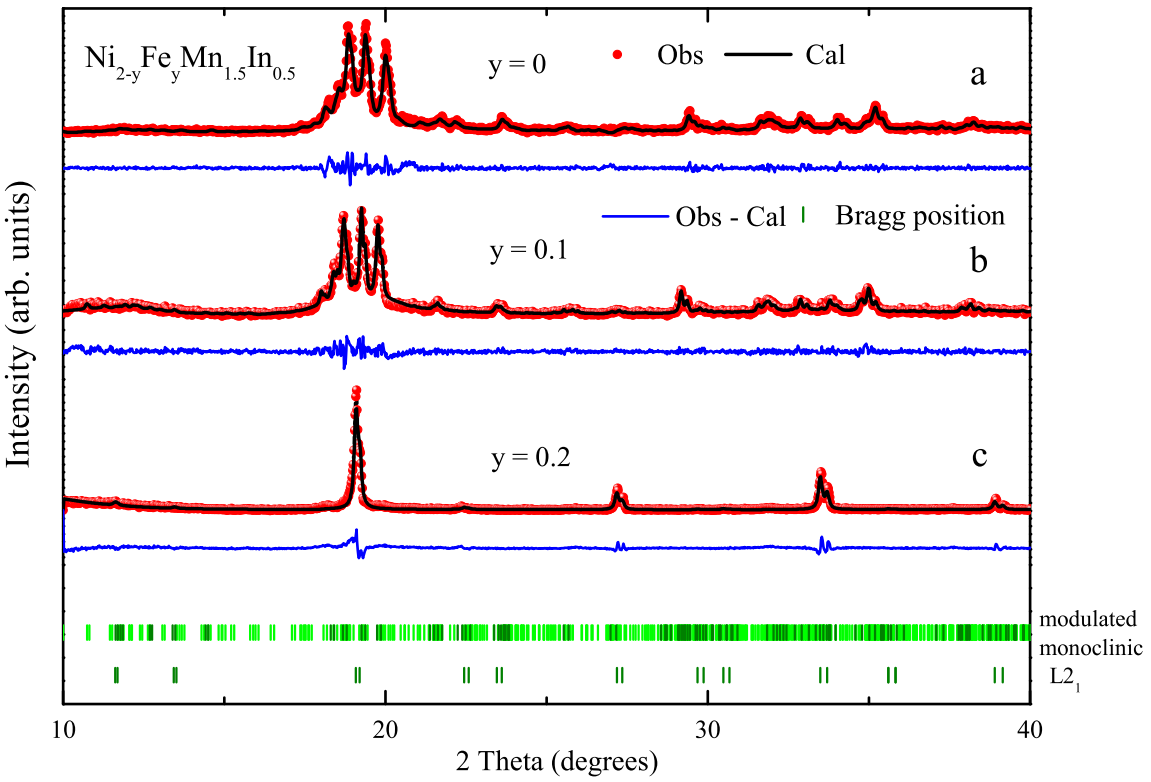

Figure 4.2: The LeBail refined x-ray diffraction data at 300 K for the series $Ni_{2-y}Fe_yMn_{1.5}In_{0.5}$.

endothermic and exothermic peaks in the cooling and warming cycles respectively. The hysteresis in the position of the warming and cooling peaks confirms the first order of the transition. The undoped alloy $Ni_2Mn_{1.5}In_{0.5}$ undergoes martensitic transition at 420 K as depicted in the Fig.4.3 (a). When Fe is doped for Mn, a decrease in martensitic transition temperature T_M is seen with increase in Fe content to 0.075 (Fig.4.3 (b) and (c)) while a further increase to $x = 0.1$ (Fig.4.3 (d)) leads to the appearance of broad feature over an otherwise sharp transition. A broad feature in DSC is an indication of compositional disorder. It can also imply the existence of more than one structural phase wherein one

Table 4.1: The refined crystallographic data for the alloy compositions.

Chemical formula	**Space group**	**Lattice parameters**
$Ni_2Mn_{1.5}In_{0.5}$	$I2/m(\alpha 0\gamma)00$	a = 4.376(4) Å, b = 5.683(6) Å, c = 4.343(4) Å $\beta = 93.58(6)^\circ$, $q = 0.311(9)$
$Ni_2Mn_{1.425}Fe_{0.075}In_{0.5}$	$I2/m(\alpha 0\gamma)00$	a = 4.450(5) Å, b = 5.624(7) Å, c = 4.376(4) Å $\beta = 93.93(1)^\circ$, $q = 0.342(5)$
$Ni_2Mn_{1.4}Fe_{0.1}In_{0.5}$	$I2/m(\alpha 0\gamma)00$	a = 4.438(2) Å, b = 5.644(1) Å, c = 4.355(1) Å $\beta = 93.32(2)^\circ$, $q = 0.337(1)$
$Ni_2Mn_{1.3}Fe_{0.2}In_{0.5}$	$Fm-3m$ $(L2_1)$ $Fm-3m$ (γ)	a = 5.983 (3) Å a = 3.616 (2) Å
$Ni_{1.9}Fe_{0.1}Mn_{1.5}In_{0.5}$	$I2/m(\alpha 0\gamma)00$	a = 4.471(5) Å, b = 5.651(7) Å, c = 4.381(4) Å $\beta = 92.97(1)^\circ$, $q = 0.339(4)$
$Ni_{1.8}Fe_{0.2}Mn_{1.5}In_{0.5}$	$Fm-3m$ $(L2_1)$	a = 6.012 (2) Å

of them is martensitic and its transformation is hindered by the other impurity phases. However, the compositional disorder can be ruled out as the SEM-EDX measurements report its composition to be $Ni_{2.00}Mn_{1.36}Fe_{0.14}In_{0.50}$ which is very much the same as the prepared composition. Similarly, substituting Fe at the expense of Ni leads to the suppression of T_M (Fig.4.3 (e) and (f)) with the DSC thermogram exhibiting some bizarre features in the alloy $y = 0.2$ (Fig.4.3 (g)) that needs further understanding.

Fig.4.4 compares the normalized resistance of both the alloys $x = 0.1$ and $y = 0.2$, exhibiting unusual features, with the alloys undergoing a sharp martensitic transition in their respective series. In the case of $Ni_2Mn_{1.5-x}Fe_xIn_{0.5}$, a sharp rise in resistance values is observed in the alloy $x = 0.075$ (Fig.4.4 a) with hysteresis in the warming and cooling cycles as a signature of first order transition in the same temperature range as DSC measurement. However, a much slower rise in resistance is seen in the alloy $x = 0.1$ (Fig.4.4 b) at around 350 K, which is consistent with the broad transition in the DSC thermogram. In addition to this, a weak first order transition is seen at $\sim$ 380

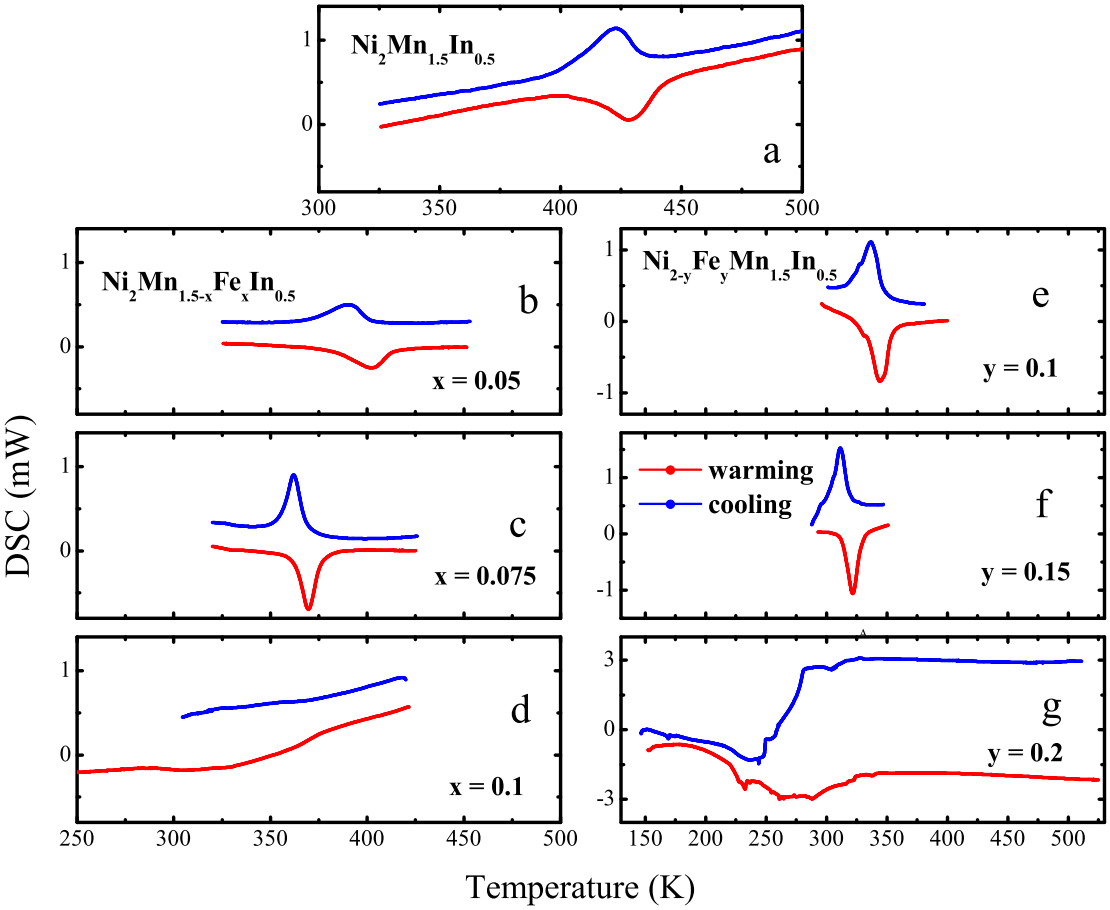

Figure 4.3: The differential scanning calorimetry plots during warming and cooling cycles in the alloy compositions.

K (inset Fig.4.4 e) which could be due to martensitic transformation. This explains the occurrence of the modulated structure in XRD at room temperature. There is a possibility that the broad transition at 350 K could be due to short range order of the elastic strain vector. The presence of two transitions, one hinting at long range martensitic order and the other pointing to some sort of glassy phase transition, indicates the presence of phase co-existence in this alloy. In the second series $Ni_{2-y}Fe_yMn_{1.5}In_{0.5}$, the behaviour of normalized resistance plots signifies martensitic transition in the alloy $y = 0.1$ (Fig.4.4 c). However, in the case of $y = 0.2$ (Fig.4.4 d), the situation is completely changed as it

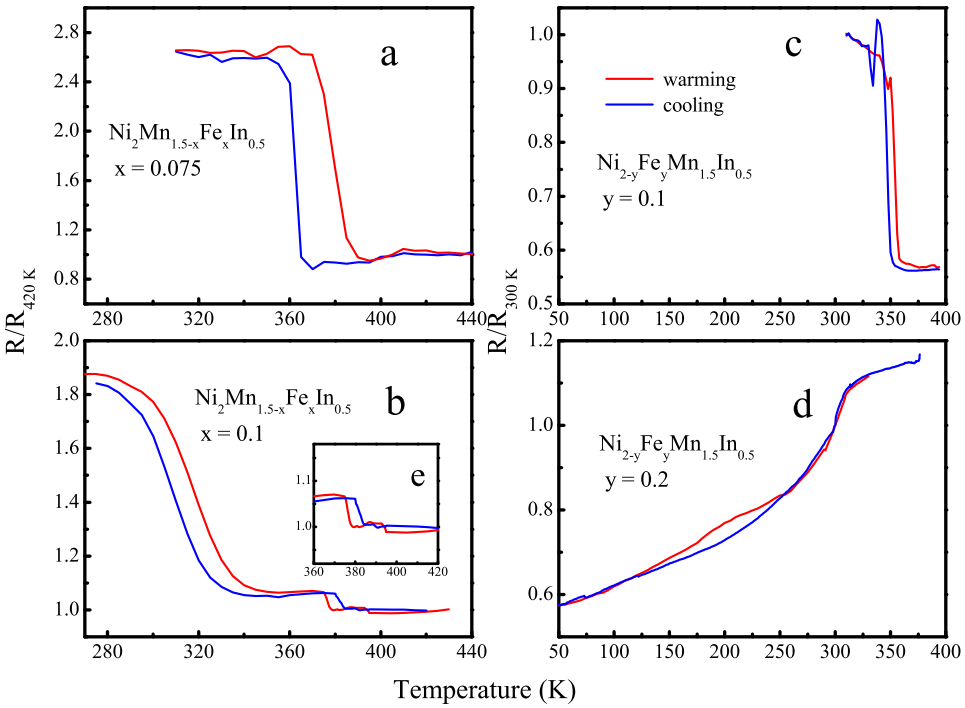

Figure 4.4: The temperature dependence of the normalized resistance during warming and cooling cycles in the alloy compositions.

displays a metallic behavior with an anomaly at 314 K followed by a weak hysteresis that is more prominently seen in the temperature range of 250 K - 140 K. Such a behavior could be ascribed to the cubic phase seen from the diffraction measurements.

To investigate the probable glassy nature, AC storage modulus and internal friction or loss were measured as a function of temperature at several different frequencies between 10 Hz and 0.1 Hz in the alloys $x = 0.1$ and $y = 0.2$ and compared with the alloys of lower Fe content in their respective series. Fig.4.5 depicts the storage modulus and $tan\delta$ in the alloy compositions at a single frequency of 1.1 Hz. It has been observed that the temperature evolution of ac storage modulus exhibit a dip followed by a sharp increase and a peak in loss ($\tan\delta$) at the onset of martensitic transition in the alloy compositions

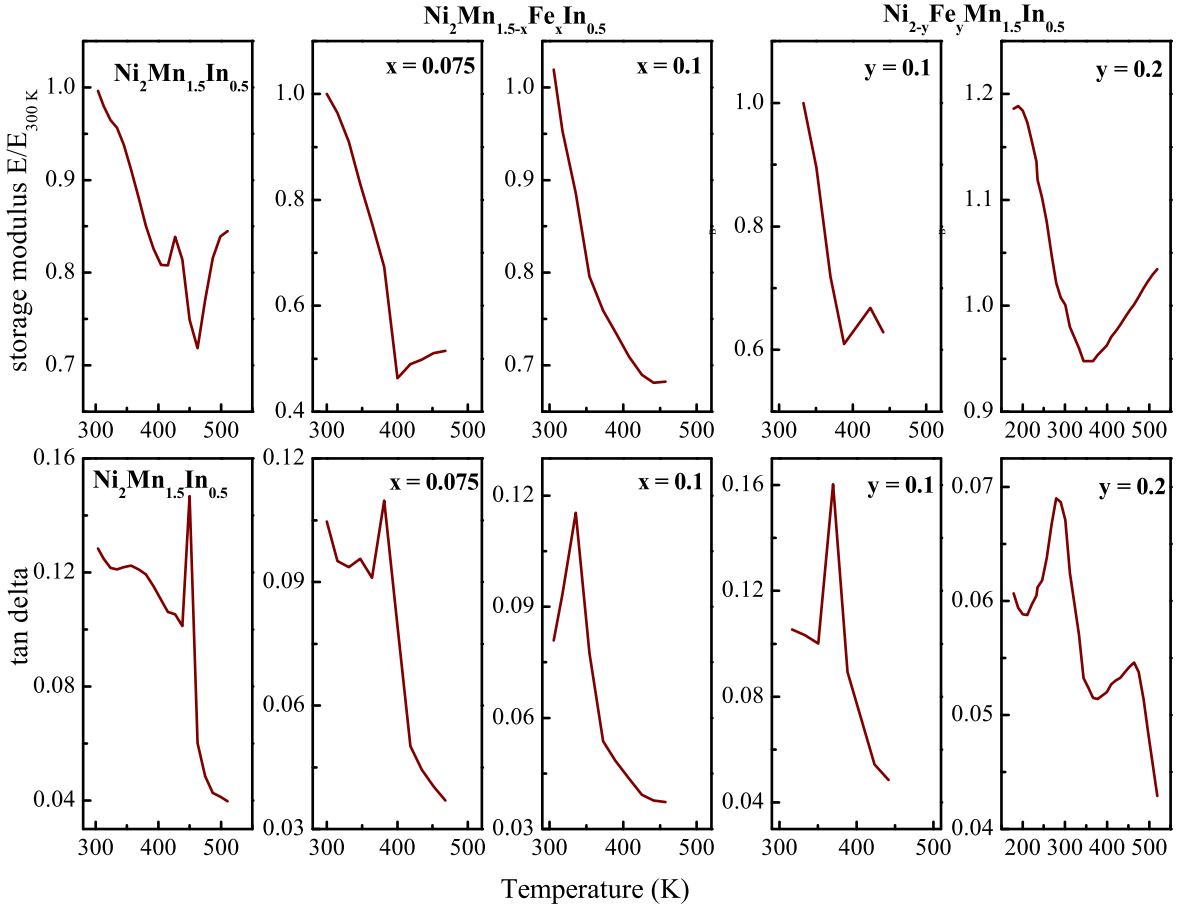

Figure 4.5: Temperature dependance of normalised ac storage modulus and $tan\delta$ measurements in the alloy compositions at a representative frequency of 1.1 Hz.

$0 \leq x < 0.1$ from the series $Ni_2Mn_{1.5-x}Fe_xIn_{0.5}$ and $0 \leq y < 0.2$ from the second series $Ni_{2-y}Fe_yMn_{1.5}In_{0.5}$.

In the alloy $x = 0.1$ from the series $Ni_2Mn_{1.5-x}Fe_xIn_{0.5}$, the sharp anomaly converts to a broad feature followed by a slow rise of storage modulus at about 350 K. The peak in tan δ observed at the same temperature and classified as T_g exhibits a frequency dependence as seen in Fig.4.6. Such a frequency dependence is absent in all other alloys with a lower Fe content in the series. A plot of T_g versus log(frequency) presented in the inset of Fig.4.6 can be fitted to the Vogel Fulcher law, $\omega = \omega_0 \exp[-E_a/k_B(T - T_0)]$, where E_a is the

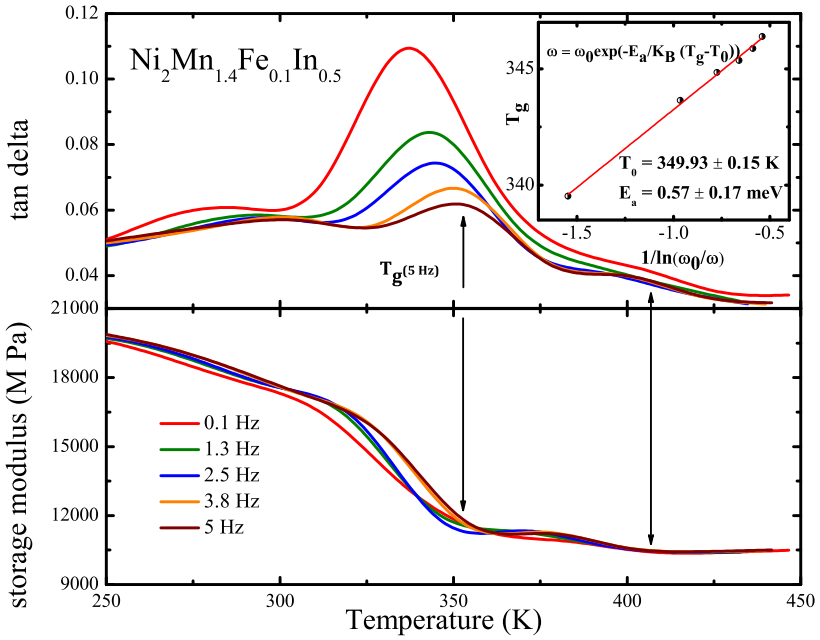

Figure 4.6: The frequency dependent behavior of ac storage modulus and tan δ observed in $Ni_2Mn_{1.4}Fe_{0.1}In_{0.5}$. Inset shows the logarithmic dependence of the peak in tan δ along with a best fit to Vogel Fulcher relation (solid line).

activation energy and T_0 is the "ideal glass" temperature. This indicates a possibility of a glassy transition in $Ni_2Mn_{1.4}Fe_{0.1}In_{0.5}$. The relative shift of glass transition temperature is assessed by a parameter $k = \frac{\Delta T_g}{T_g(\Delta \log \omega)}$ and is estimated to be 0.025. In comparison, the value of k parameter in Ni rich NiTi alloys is about 0.02.[10] This slightly higher value of k parameter in $Ni_2Mn_{1.4}Fe_{0.1}In_{0.5}$ could be due to the presence of larger sized domains in the present alloy as compared to those in Ni rich NiTi alloys. Another interesting aspect to be noted is the presence of a smaller but distinct feature in the temperature dependence of tan δ. This feature appears at about 420K (Fig.4.6) that matches with the martensitic transition temperature of undoped alloy $Ni_2Mn_{1.5}In_{0.5}$. To further check the presence of strain glassy phase in $Ni_2Mn_{1.4}Fe_{0.1}In_{0.5}$, history dependence of strain during zero field cooled (ZFC) and field cooled (FC) cycles was carried out and the results are presented

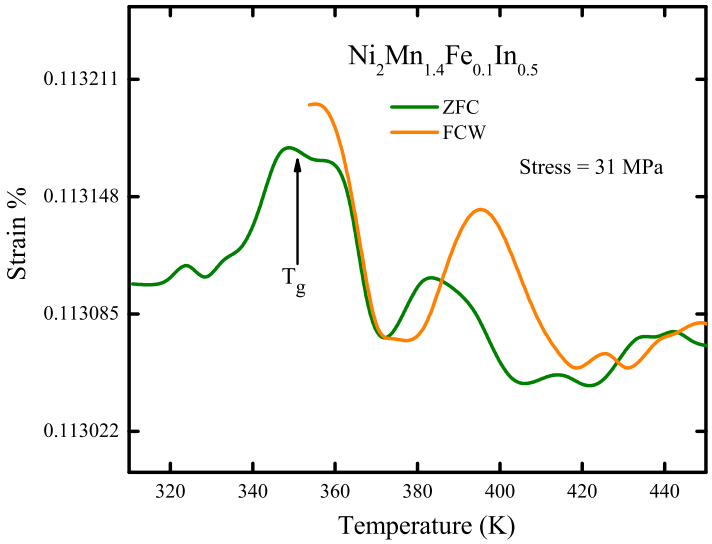

Figure 4.7: % Strain as a function of temperature recorded during zero field cooled and field cooled cycles at 6 Hz.

in Fig. 4.7. A clear deviation between the two curves is considered as a critical proof of the existence of a strain glassy phase that can be seen from $\sim$ 363 K, which is above the T_g = 350 K. This confirms that $Ni_2Mn_{1.4}Fe_{0.1}In_{0.5}$ is indeed a strain glass.

The question then arises about the room temperature structure of $Ni_2Mn_{1.4}Fe_{0.1}In_{0.5}$. For a strain glass the structure is expected to be invariant across the transition. However, the x = 0.1 alloy exhibits a martensitic structure. In magnetic cluster glasses, there are examples of materials displaying glassy characteristics and yet presenting long range magnetic order. In such cases, the clusters are large enough to show characteristics of long range magnetic order in neutron diffraction. However, the interactions between these clusters are limited which leads to glassy behaviour.[11] The presence of such large strain domains in $Ni_2Mn_{1.4}Fe_{0.1}In_{0.5}$ cannot be ruled out. In fact, it is supported by the presence

of a weak but distinct feature in ac storage modulus and loss at about 422 K (See Fig. 4.6). It appears that $Ni_2Mn_{1.4}Fe_{0.1}In_{0.5}$ consists of clusters that are largely deficient in Fe and hence undergo martensitic transition at a temperature very close to that of undoped alloy. These clusters are large enough to show signatures of incommensurate modulated monoclinic structure in diffraction but have very limited interactions with other similar clusters due to the presence of minor Fe rich impurity phases. The slightly higher value of k parameter (0.025) as compared to that observed in NiTi alloys also supports the presence of large clusters. Hence $Ni_2Mn_{1.4}Fe_{0.1}In_{0.5}$ is termed as a unusual strain glass.

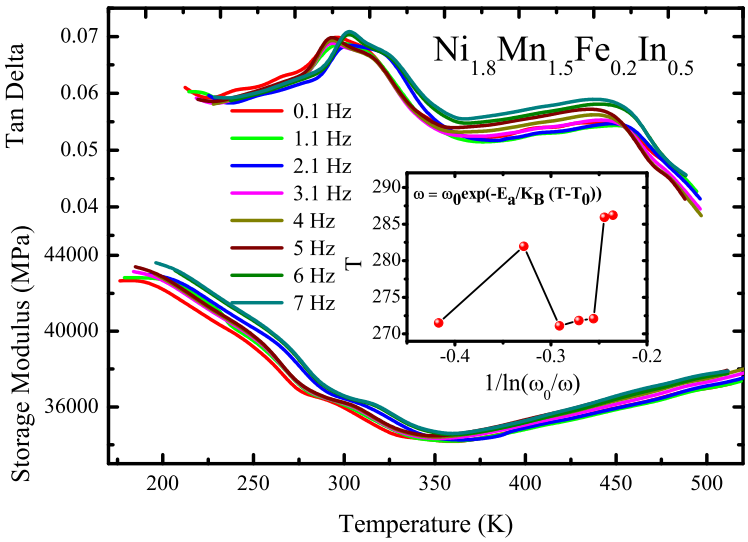

Figure 4.8: Temperature dependent ac storage modulus and tan δ measurements for the composition $Ni_{1.8}Mn_{1.5}Fe_{0.2}In_{0.5}$ at multiple frequencies. Inset shows plot of T_g versus $\log \omega$ which is not in accordance with Vogel Fulcher relation for glassy dynamics.

The composition $y = 0.2$ from the second series $Ni_{2-y}Fe_yMn_{1.5}In_{0.5}$ (See Fig. 4.5), shows a broad valley in the storage modulus and a broad peak in the loss at about 280 K. Another broad feature in the loss modulus is seen at 450 K, but there is no

corresponding feature seen in the storage modulus. The frequency dependence of storage modulus and loss feature at 280 K were probed and are displayed in Fig. 4.8. No Vogel-Fulcher dependence is seen as a function of frequency indicating the absence of a strain glassy transition (inset of Fig. 4.8). The loss feature at 450 K also did not show any frequency dependence in accordance with Vogel-Fulcher law. Thus $Ni_{1.8}Fe_{0.2}Mn_{1.5}In_{0.5}$ neither displays a martensitic transition nor a strain glassy phase. Further, the possibility of crystallization of the strain glassy phase was checked. This was done by performing repeated DSC measurements on $y = 0.2$ alloy after giving it an isothermal treatment at certain temperatures below 300 K.[12] But the DSC thermograms did not show any significant changes.

Fig. 4.9 displays the temperature dependent magnetization measurements M(T) recorded in applied magnetic fields of 5 mT and 5 T. In the alloys $x = 0.075$, $x = 0.1$ and $y = 0.1$, the first order martensitic transition is seen as evident from the hysteresis in the warming and cooling data. In 5 mT field, ZFC (zero field cooled) data exhibits a broad peak at the blocking temperature T_B in addition to the large splitting between ZFC and the FC (field cooled) curves signifying a non-ergodic behaviour. In the first series $Ni_2Mn_{1.5-x}Fe_xIn_{0.5}$, an increase in Fe concentration from 0.075 to 0.1 leads to a decrease in T_M from 360 K to about 302 K while the T_B shifts towards higher temperature. This indicates the strengthening of ferromagnetic interactions at the expense of martensitic interactions. Interestingly in $x = 0.1$, the ZFC curve approaches a negative magnetization value below $T = 100$ K (Fig. 4.9(b)) signifying a magnetic compensation. Since the

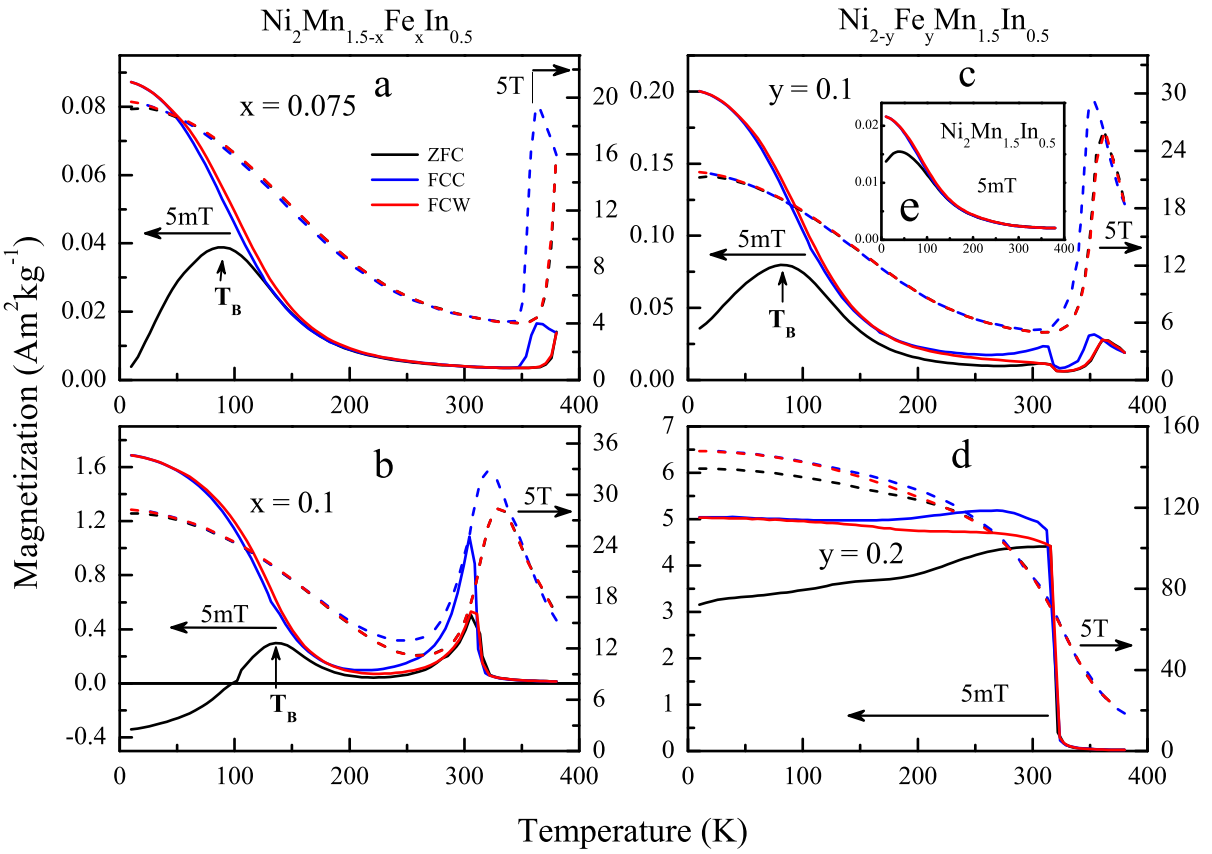

Figure 4.9: Magnetization as a function of temperature for the alloys $x = 0.075$ and $x = 0.1$ in the series $Ni_2Mn_{1.5-x}Fe_xIn_{0.5}$ (a, b) and for the alloys $y = 0.1$ and $y = 0.2$ in the series $Ni_{2-y}Fe_yMn_{1.5}In_{0.5}$ (c, d) during warming after cooling the alloys in zero field (ZFC) and subsequent warming (FCW) and cooling (FCC) cycles in magnetic field.

hysteresis region in the M(T) measurement in 5 mT coincides with the one in normalized resistance curves (see Fig. 4.4 b), the transition in M(T) could be the signature of the martensitic transformation of the large undoped grains. As the magnetic field is increased from 5 mT to 5 T, T_M shifts towards higher temperature (Fig.4.9(b)). Such a behaviour of increasing T_M with magnetic field is not seen in the other two transforming alloys, $x = 0.075$ and $y = 0.1$. Contrary to this, the magnetization of $Ni_{1.8}Fe_{0.2}Mn_{1.5}In_{0.5}$ increases sharply displaying a paramagnetic to ferromagnetic transition at $T_C = 314$ K (Fig.

4.9(d)). However, the presence of hysteresis in the warming and the cooling magnetization curves in the temperature range of 150 K to 350 K is similar to the one observed in resistance curves (see Fig. 4.4 d). This observation propels a need for a deeper understanding of the structure.

4.2.3 Structure : Synchrotron x-ray diffraction studies

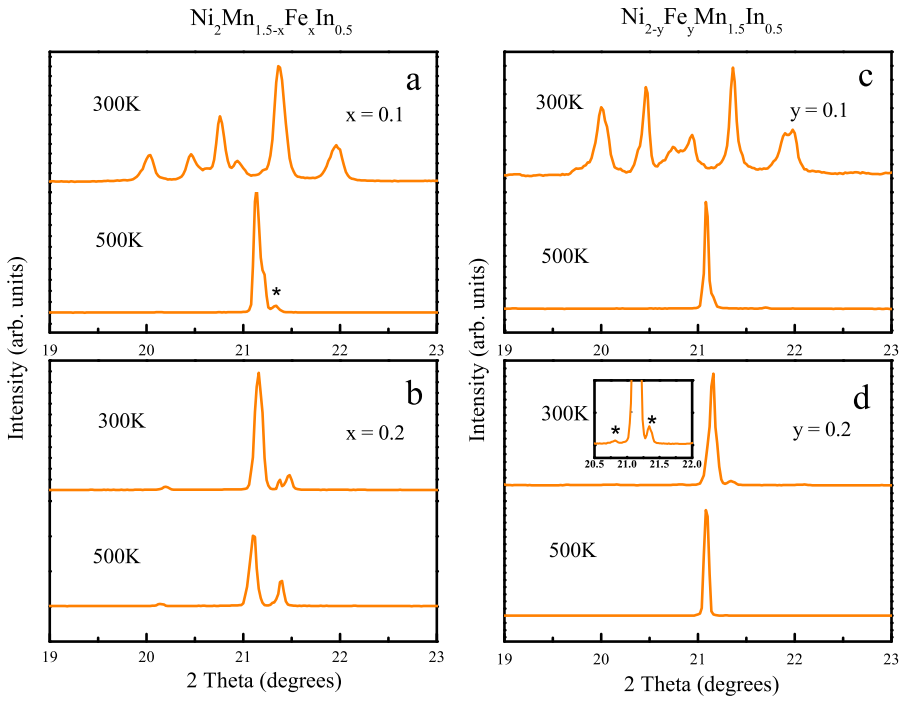

Figure 4.10: X-ray diffraction data in the limited two theta range highlighting the evolution of phases with temperature and Fe concentration in the series $Ni_2Mn_{1.5-x}Fe_xIn_{0.5}$ (a, b) and $Ni_{2-y}Fe_yMn_{1.5}In_{0.5}$ (c, d). The presence of minor impurity phases arising due to Fe substitution are marked as (*).

The results so far have shown that in $Ni_2Mn_{1.5}In_{0.5}$, when Fe is doped at the expense of Mn, the martensitic transition is suppressed via strain glassy phase. However, when Fe is substituted for Ni, ferromagnetic interactions are enhanced with the complete destruction of martensitic transition. Therefore, it is essential to understand the role of the dopant

in the occurrence of the strain glassy phase. In particular, the nature of the structural defect created leads to the formation of the strain glass and the apparent site selectivity of the dopant atom that results in a cubic ferromagnetic ground state. Hence with the pretext of exploring the possible impurity phases as a result of Fe doping in the alloys, synchrotron x-ray diffraction measurements were performed at 300 K and at 500 K, which is well above the martensitic transition temperature of the undoped alloy. The phases were identified using the LeBail refinement.

Fig. 4.10 highlights the diffraction patterns in the limited two theta range. In the first series $Ni_2Mn_{1.5-x}Fe_xIn_{0.5}$, the alloy $x = 0.1$ (Fig. 4.10 a) transforms from modulated monoclinic structure to a combination of a major cubic Heusler phase and a minor fcc impurity phase (marked as $*$) with the increase in temperature from 300 K to 500 K. In the alloy $x = 0.2$ (Fig. 4.10 b), the same impurity phase seems to have grown and is present at both the temperatures along with the major Heusler phase. It, therefore, appears that at 300 K, the modulated monoclinic structure of the alloy $x = 0.1$ has masked the impurity phase, displaying a single phase. The presence of the impurity phase in $x = 0.1$ lends weight to the earlier proposition that the strain glass phase in $Ni_2Mn_{1.4}Fe_{0.1}In_{0.5}$ occurs due to large martensitic grains separated by an impurity phase. The martensitic grains transform into an austenitic phase above 300 K. Since the phase fraction of the impurity phase increases with Fe doping, it either consists of Fe or the impurity phase itself is induced by Fe doping.

In the second series $Ni_{2-y}Fe_yMn_{1.5}In_{0.5}$, the alloy $y = 0.1$ (Fig. 4.10 c) exhibits the

modulated phase at 300 K which transform in to a cubic Heusler phase at 500 K. On the other hand, in the alloy $y = 0.2$ (Fig. 4.10 d), two phases consisting of major cubic Heusler and a minor percentage of monoclinic phase (I2/m) are seen at 300 K. The monoclinic phase was not noticed in the diffraction pattern recorded using a laboratory source, and hence its phase fraction should be meager. The presence of this martensitic impurity phase could be the reason for observed hysteresis in the warming and cooling magnetization and resistance curves of $y = 0.2$ alloy. Despite the presence of the impurity phase, these alloys do not exhibit a strain glassy ground state; instead, the martensitic state is completely suppressed by a ferromagnetic cubic phase.

4.2.4 Local structure : EXAFS studies

It appears that the ground state of Fe doped Ni-Mn-In alloys depends on the doping site. In Mn rich Ni-Mn-In alloys, Ni atoms are expected to occupy the X sites while the Mn atoms are present on the Y sublattice and along with In atoms on the Z sublattices. To determine the site occupancy of the Fe atoms and to study the structural interactions that play a role in the determination of the ground state, the local environment of Ni, Mn, and Fe atoms have been looked upon via EXAFS experiments performed at 300 K and 50 K.

EXAFS data at Ni and Mn K edges were analyzed together using a common structural model. The analysis was carried out using 14 independent parameters. The amplitude reduction factor (S_0^2) for the two data sets were obtained from the analysis of respective metal foils and were kept fixed during the analysis. The magnitude of Fourier transform

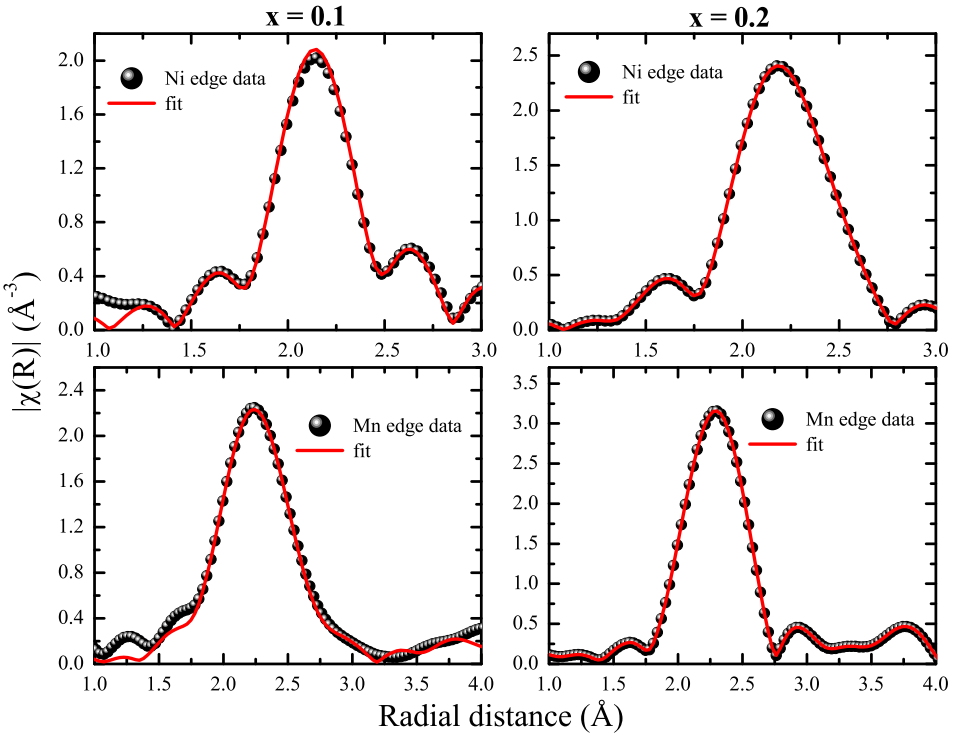

Figure 4.11: The magnitude of Fourier transform of the EXAFS spectra recorded at 50 K at the Ni K and Mn K edges for the alloys $x = 0.1$ and $x = 0.2$ in the series $Ni_2Mn_{1.5-x}Fe_xIn_{0.5}$.

(FT) of Ni K edge EXAFS spectra include the contribution from the nearest neighbors Mn and In atoms at ~ 2.5 Å with their coordination number fixed as per the composition ratio and from the next nearest neighbor Ni atoms (~ 3.0 Å). Mn K edge EXAFS spectra, on the other hand, are fitted considering the nearest neighbor, Ni (~ 2.5 Å), the next nearest neighbor, In and Mn_Z (~ 3.0 Å) and the third neighbor, Mn_Y at (~ 4.2 Å) as backscattered atoms. Best fits at all temperatures were obtained only after relaxing the constraints imposed by the cubic austenitic structure as described in earlier studies.[13]

Fig. 4.11 depicts the best fits for Ni K and Mn K EXAFS spectra obtained in the first series when Fe is substituted for Mn, while Fig. 4.12 displays the results in the second

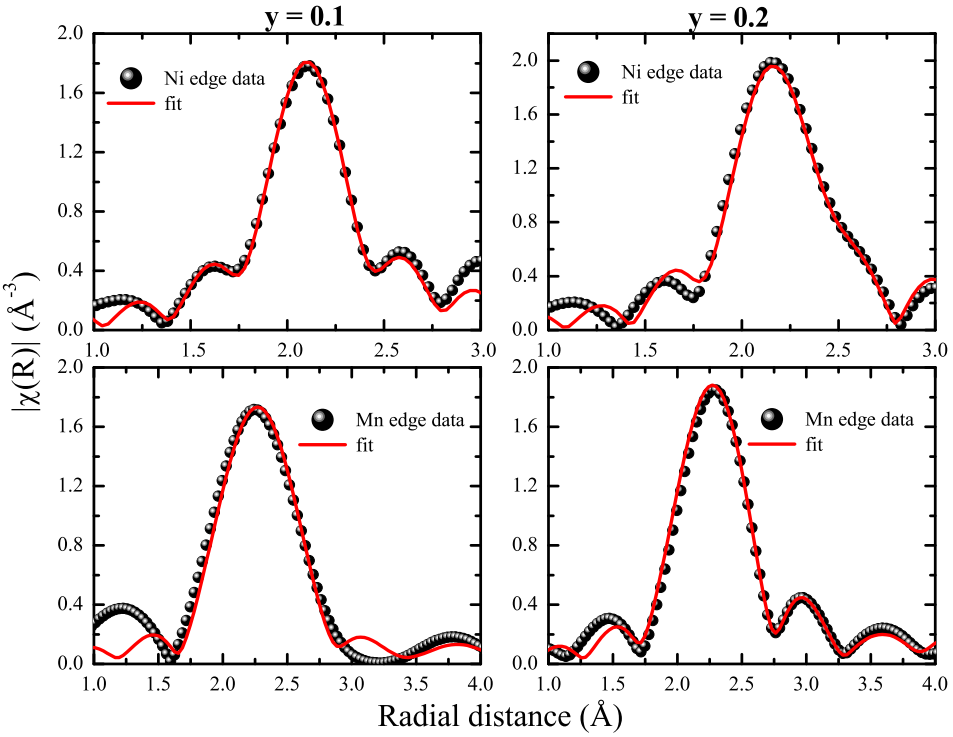

Figure 4.12: The magnitude of Fourier transform of EXAFS spectra at 50 K at the Ni K and Mn K edges for the alloys $y = 0.1$ and $y = 0.2$, in the series $Ni_{2-y}Fe_yMn_{1.5}In_{0.5}$.

series when Fe is doped at the expense of Ni. The best fit values of bond length (R) and mean square radial displacement (σ^2) at 300 K and 50 K are listed in Table 4.2. The results are in good agreement with previously reported EXAFS studies on such Mn rich Ni-Mn-In alloys.[14,15] As expected, the nearest neighbour, Ni–Mn distance is shorter than the Ni–In the bond distance. Similarly, the Mn_Y–Mn_Y distance (Mn_Y describes Mn atoms in the Y sublattice of X_2YZ Heusler structure) decreases from $\sim$ 4.4 Å in alloys undergoing a martensitic transformation in the paramagnetic state to $\sim$ 4.2 Å in alloys with dominant ferromagnetic interactions. This is clearly evident in $Ni_{2-y}Fe_yMn_{1.5}In_{0.5}$. At 300 K, with an increase in Fe content, the crystal structure changes from modulated monoclinic in the alloy $y = 0.1$ to a major cubic Heusler in the alloy $y = 0.2$ along with

the strengthening of ferromagnetic interactions. The cubic Heusler structure demands the bond distances Mn–In and Mn_Y–Mn_Z (Mn_Z represents Mn atoms occupying Z sublattice) to be equal. This change is also visible as the structure of Fe doped alloys converts from martensitic to cubic Heusler structure.

Table 4.2: The results of the best fits obtained at 300 K and 50 K at Ni K and Mn K edges in the $k-$range 3–12 Å^{-1}, and in $R-$range 1–3 Å. The parameter R gives the bond length while the mean square disorder in the bond length is described by σ^2. Figures in parenthesis indicate uncertainty in the last digit.

Alloys	**Temperature**		**Bonds** Ni - Mn	Ni - In	Mn - In	Mn_Y - Mn_Y	Mn_Y - Mn_Z
$Ni_2Mn_{1.5}In_{0.5}$	300 K	R (Å)	2.571(8)	2.620(7)	2.88(4)	4.40(5)	3.05(4)
		σ^2 (Å^2)	0.0057(4)	0.0099(8)	0.050(5)	0.025(8)	0.04(3)
	50 K	R (Å)	2.58(1)	2.618(5)	2.88(4)	4.45(1)	3.01(4)
		σ^2 (Å^2)	0.0018(5)	0.0068(5)	0.008(5)	0.02(1)	0.016(7)
$Ni_2Mn_{1.4}Fe_{0.1}In_{0.5}$	300 K	R (Å)	2.57(1)	2.62(1)	2.86(4)	4.39(6)	3.05(4)
		σ^2 (Å^2)	0.0105(7)	0.005(1)	0.050(5)	0.025(8)	0.04(3)
	50 K	R (Å)	2.572(8)	2.61(1)	2.89(4)	4.45(1)	3.01(4)
		σ^2 (Å^2)	0.001(1)	0.0062(5)	0.008(5)	0.02(1)	0.016(7)
$Ni_2Mn_{1.3}Fe_{0.2}In_{0.5}$	300 K	R (Å)	2.54(1)	2.63(1)	2.93(3)	4.25(7)	2.98(4)
		σ^2 (Å^2)	0.011(1)	0.004(1)	0.003(4)	0.02(1)	0.010(9)
	50 K	R (Å)	2.542(9)	2.64(2)	2.94(3)	4.24(4)	2.96(2)
		σ^2 (Å^2)	0.002(1)	0.0049(6)	0.002(2)	0.016(4)	0.003(3)
$Ni_{1.9}Fe_{0.1}Mn_{1.5}In_{0.5}$	300 K	R (Å)	2.577(9)	2.633(8)	2.88(4)	4.39(6)	3.05(4)
		σ^2 (Å^2)	0.0048(8)	0.0116(8)	0.050(5)	0.025(8)	0.04(3)
	50 K	R (Å)	2.588(7)	2.619(8)	2.89(4)	4.45(1)	3.02(4)
		σ^2 (Å^2)	0.0015(8)	0.0072(4)	0.008(5)	0.02(1)	0.016(7)
$Ni_{1.8}Fe_{0.2}Mn_{1.5}In_{0.5}$	300 K	R (Å)	2.54(2)	2.62(1)	2.93(6)	4.21(6)	2.95(5)
		σ^2 (Å^2)	0.013(2)	0.003(1)	0.026(5)	0.02(1)	0.005(7)
	50 K	R (Å)	2.576(7)	2.625(6)	2.93(2)	4.25(5)	2.95(1)
		σ^2 (Å^2)	0.0080(7)	0.0009(5)	0.001(1)	0.04(4)	0.08(1)

In $Ni_2Mn_{1.5-x}Fe_xIn_{0.5}$, the Fe K EXAFS spectra recorded at 300 K appears to differ from that of Ni K and Mn K edge spectra, indicating a different local environment around Fe in comparison with Ni and Mn atoms. Since the compositions $x = 0.1$ and $x = 0.2$, reveal the presence of an fcc impurity phase, an attempt was made to fit the Fe K edge EXAFS to structural correlations obtained for the fcc structure. A good fit is obtained

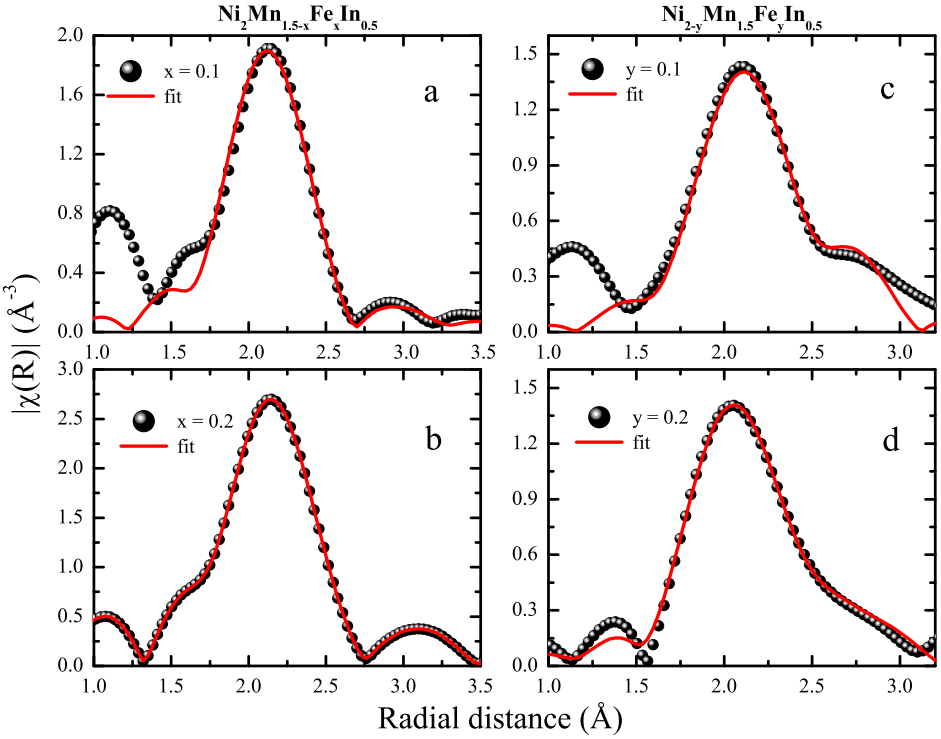

Figure 4.13: The Fe K edge EXAFS spectra in $R-$space (Fourier transform magnitude) obtained at 300 K for the alloys $x = 0.1$ (a) and $x = 0.2$ (b) in the series $Ni_2Mn_{1.5-x}Fe_xIn_{0.5}$ and for the alloys $y = 0.1$ (c) and (d) $y = 0.2$ in the series $Ni_{2-y}Fe_yMn_{1.5}In_{0.5}$.

by considering 12 Ni atoms at $\sim$ 2.5 Å and 6 Fe atoms at $\sim$ 3.5 Å as can be seen in Fig. 4.13(a and b). All attempts to include In atoms as scatterers either in the first shell ($\sim$ 2.5 Å) or the second shell ($\sim$ 3.5 Å) did not result in physically acceptable parameters. Therefore, the impurity phase segregated in $Ni_2Mn_{1.5-x}Fe_xIn_{0.5}$ consists of Fe and Ni and from the Fe-Ni binary phase diagram was identified as $\gamma-$(Fe,Ni) phase.

In the second series $Ni_{2-y}Fe_yMn_{1.5}In_{0.5}$, though Fe is doped for Ni, the local structure of Fe looks similar to that of Mn at the Y/Z site rather than Ni at the X site. It may be mentioned here that in the X_2YZ Heusler structure, X (Ni) atoms have Y (Mn) and Z (In) atoms in the first coordination shell and X (Ni) atoms in the second coordination

shell while the Y (Mn) atoms have only X (Ni) in their first coordination shell and Z (In/Mn) atoms in the second coordination shell. Therefore, if Fe replaces Ni at the X site, then it should have Mn and In atoms as nearest neighbours and Ni atoms as the second nearest neighbours. However, EXAFS signal can be fitted with only Ni atoms in the first coordination shell and In/Mn atoms as second neighbours. The best fit to the experimental data is shown in Fig. 4.13(c and d), and the parameters obtained from fitting are presented in Table 4.3.

Table 4.3: The results of the best fits obtained at 300 K at Fe K edge in the $k-$range 3–12 $Å^{-1}$, and in $R-$range 1–3 Å. The parameter R gives the bond length while the thermal variation in bond length is described by σ^2. Figures in parenthesis indicate uncertainty in the last digit.

Alloys		**Bonds** Fe - Ni	Fe - Fe	Fe - In
$Ni_2Mn_{1.4}Fe_{0.1}In_{0.5}$	R (Å)	2.508(8)	3.546(8)	
	σ^2 (Å^2)	0.006(3)	0.02(2)	
$Ni_2Mn_{1.3}Fe_{0.2}In_{0.5}$	R (Å)	2.525(4)	3.571(4)	
	σ^2 (Å^2)	0.009(1)	0.015(6)	
$Ni_{1.9}Fe_{0.1}Mn_{1.5}In_{0.5}$	R (Å)	2.46(5)	2.8(1)	2.97(8)
	σ^2 (Å^2)	0.01(1)	0.02(3)	0.01(1)
$Ni_{1.8}Fe_{0.2}Mn_{1.4}In_{0.5}$	R (Å)	2.41(2)	2.93(4)	3.1(1)
	σ^2 (Å^2)	0.004(3)	0.008(6)	0.01(1)

4.3 Discussion

In the X_2YZ Heusler structure, the intensities of the superlattice reflections, (111) and (200), are sensitive to the antisite disorder. The disorder associated with the occupancy of Y and Z sublattices of the Heusler structure is known as $B2$ disorder and results in lowering the intensities of both (111) and (200) reflections. Furthermore, a disorder

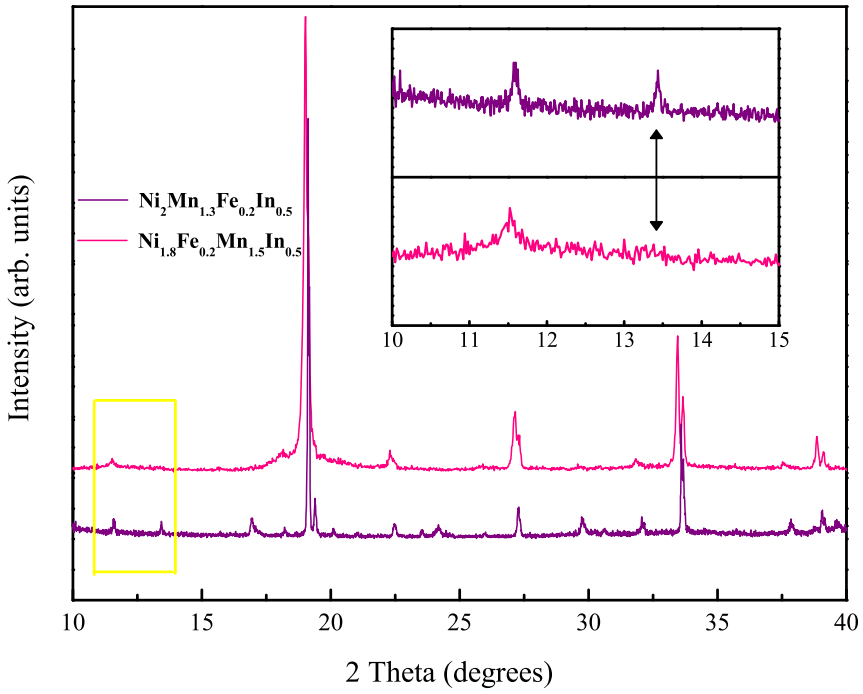

Figure 4.14: A comparison of the x-ray diffraction patterns of the alloys $Ni_2Mn_{1.3}Fe_{0.2}In_{0.5}$ and $Ni_{1.8}Fe_{0.2}Mn_{1.5}In_{0.5}$ featuring the absence of 200 peak and the presence of $A2$ disorder in the later.5

involving X and Y sublattices affects the intensity of (200) reflection and is identified as $A2$ disorder.[16,17] In $Ni_{2-y}Fe_yMn_{1.5}In_{0.5}$, the doped Fe appears to occupy the Y/Z sublattice as evidenced from EXAFS measurements. This should force the Mn atoms to occupy the vacant X sites thereby resulting in an $A2$ type disorder. Fig. 4.14 compares the x-ray diffraction patterns of $Ni_2Mn_{1.3}Fe_{0.2}In_{0.5}$ and $Ni_{1.8}Fe_{0.2}Mn_{1.5}In_{0.5}$, highlighting the absence of (200) reflection in $Ni_{1.8}Fe_{0.2}Mn_{1.5}In_{0.5}$ and confirming the presence of $A2$ type disorder.

The above studies affirm that the martensitic state is suppressed when Fe is doped in the martensitic alloy $Ni_2Mn_{1.5}In_{0.5}$. There is a possibility that the dopant atom either segregates in an impurity phase or occupies one of the crystallographic sites in the Heusler

structure. These two scenarios decide the ground state as indicated from both XRD and EXAFS studies. In the series $Ni_2Mn_{1.5-x}Fe_xIn_{0.5}$, as the Fe concentration rises, an impurity phase, $\gamma-$(Fe,Ni) segregates in addition to the martensitic Heusler phase. The large Heusler grains undergo martensitic transformation just above room temperature. But the ordering of the elastic strain vector is spatially disturbed by the presence of the impurity phase resulting in a strain glass phase. This is evident from the fact that the glass transition temperature $T_g = 350$ K is higher than the martensitic transition temperature $T_M = 304$ K. Moreover, the increase in the applied magnetic field from 5 mT to 5 T results in an increase in T_M from 304 K to 340 K in the alloy $Ni_2Mn_{1.4}Fe_{0.1}In_{0.5}$. In Mn excess Ni-Mn-In alloys, T_M generally decreases with the magnetic field. This contravening behaviour of increase in T_M under magnetic field can be ascribed to a strong coupling between magnetic and elastic degrees of freedom. Increased magnetic field lowers the entropy of the system, thus promoting an increased order of the elastic strain vector and higher transformation temperature.

Contrary to this, in $Ni_{2-y}Fe_yMn_{1.5}In_{0.5}$, Fe promotes antisite disorder by occupying Y or Z sublattices and forcing Mn to the vacancies in the X sublattice of the Heusler alloy. This $A2$ disorder suppresses martensitic transition and strengthens ferromagnetic interactions resulting in a cubic ferromagnetic ground state. It appears that when the X sublattice in X_2YZ Heusler structure is fully occupied, Fe doping results in the segregation of an impurity phase. In the case of Fe being doped into the X sublattice, it promotes antisite disorder and accommodates itself in the Y/Z sublattice of the Heusler structure.

4.4 Conclusions

In conclusion, the addition of Fe at the expense of Mn in the martensitic alloy $Ni_2Mn_{1.5}In_{0.5}$, results in the phase segregation into a major Heusler phase and a minor $\gamma-$(Fe,Ni) phase. This $\gamma-$(Fe,Ni) phase serves as an impediment for the long range ordering of the elastic strain vector, promoting a strain glassy ground state. On the other hand, when Fe is doped for Ni, it replaces Mn in the Y/Z Heusler sublattices forcing Mn to occupy the X sublattice along with Ni thereby creating an $A2$ disorder. The presence of antisite disorder suppresses martensitic transition by promoting a ferromagnetic ground state. This study implies that the suppression of martensite via strain glass occurs if the Fe addition facilitates the segregation of an impurity phase. However, if the dopant Fe is accommodated in the Heusler phase even via an antisite disorder; the resultant stronger ferromagnetic interactions forbid martensitic transformation of the resultant alloy.

References

[1] X. Ren. *Strain Glass and Strain Glass Transition*, pages 201–225. Springer Berlin Heidelberg, 2012.

[2] D. P. Wang, X. Chen, Z. H. Nie, N. Li, Z. L. Wang, Y. Ren, and Y. D.Wang. *Europhys. Lett.*, 98:46004, 2012.

[3] T. Krenke, M. Acet, E. F. Wassermann, X. Moya, L. Mañosa, and A. Planes. *Phys. Rev. B*, 73:174413, 2006.

[4] K. R. Priolkar, P. A. Bhobe, D. N. Lobo, S. W. D'Souza, S. R. Barman, Aparna Chakrabarti, and S. Emura. *Phys. Rev. B*, 87:144412, 2013.

[5] M. K. Chattopadhyay, K. Morrison, A. Dupas, V. K. Sharma, L. S. Sharath Chandra, L. F. Cohen, and S. B. Roy. *Journal of Applied Physics*, 111, 2012.

[6] D. N. Lobo, K. R. Priolkar, S. Emura, and A. K. Nigam. *Journal of Applied Physics*, 116, 2014.

[7] L. Chen, F. X. Hu, J. Wang, L. F. Bao, J. R. Sun, B. G. Shen, J. H. Yin, and L. Q. Pan. *Appl. Phys. Lett.*, 101:012401, 2012.

[8] C. Tan, Z. Tai, K. Zhang, X. Tian, and W. Cai. *Sci. Rep.*, 7:43387, 2017.

[9] H. Zhang, M. Qian, X. Zhang, L. Wei, F. Cao, D. Xing, X. Cui, J. Sun, and L. Geng. *J. Alloys Compd.*, 689:481 – 488, 2016.

[10] S. Sarkar, Xiaobing Ren, and K. Otsuka. *Phy. Rev. Lett.*, 95:205702, 2005.

[11] E. T. Dias, K. R. Priolkar, A. K. Nigam, R. Singh, A. Das, and G. Aquilanti. *Phys. Rev. B*, 95:144418, 2017.

[12] J. Yuanchao, D. Wang, X. Ding, K. Otsuka, and X. Ren. *Phys. Rev. Lett.*, 114:055701, 2015.

[13] P. A. Bhobe, K. R. Priolkar, and P. R. Sarode. *Phys. Rev. B*, 74:224425, 2006.

[14] K. R. Priolkar, D. N. Lobo, P. A. Bhobe, S. Emura, and A. K. Nigam. *EPL*, 3:94, 2011.

[15] D. N. Lobo, K. R. Priolkar, P. A Bhobe, D. Krishnamurthy, and S. Emura. *Appl. Phys. Lett.*, 96:38006, 2010.

[16] P. J. Webster. *Contemp. Phys.*, 10:559–77, 1969.

[17] Y. Takamura, R. Nakane, and S. Sugahara. *J. Appl. Phys.*, 105:07B109, 2009.

Chapter 5

Investigation of pre-transition phases in Ni-Mn-In based magnetic shape memory alloys

5.1 Introduction

A strain glass phase is expected in a defect-containing ferroelastic/martensitic material when defect concentration exceeds a critical value. This is because the presence of impurities impede the long range ordering of the elastic strain vector resulting in a frozen disordered ferroelastic phase. However, the previous chapter on Fe doped Ni-Mn-In alloys concludes that it is not necessary for all the impurity doped martensitic alloys to display a strain glass transition.

The alloy $(NiMn)_2$ is an antiferromagnet exhibiting a tetragonal $L1_0$ structure in the martensite state below 973 K.[1] The progressive replacement of Mn with In, Sn or Sb to realize $Ni_2Mn_{2-y}Z_y$, causes a decrease in martensitic transition temperature T_M, resulting in complete suppression of the martensite phase at a critical concentration.[2,3] This critical concentration, and the rate of variation of transition temperature with average electron per atom (e/a) ratio, rely on the type of replaced atom (In, Sn or Sb). However, no non-

ergodic phases like strain glass have been hitherto reported. Such Ni-Mn based magnetic shape memory alloys are generally investigated as Mn rich Heusler alloys with a generic formula $Ni_2Mn_{1+x}Z_{1-x}$ (Z = In, Sn or Sb). In these alloys, the high temperature austenite phase is predominantly ferromagnetic below the characteristic Curie temperature T_C. While below T_M, a state competing ferromagnetic and antiferromagnetic interactions appear in the martensitic state.[4–6] The driving force for the martensitic transition is believed to be the hybridization of Ni 3*d* states and the 3*d* states of antiferromagnetically coupled excess Mn replacing Z atom.[7] The martensitic structure is proposed to be 5M and 7M through the superspace approach.[8–10] In addition to this, the inter martensitic transformations are also noticed, and with further lowering of temperature depending on the composition, the martensite achieves $L1_0$ phase as the ground state.[11] EXAFS investigations conclude the presence of local structural disorder to be responsible for increased hybridization of the Ni 3d and Mn 3d states.[12–14] This strong coupling between the structural and magnetic degrees of freedom is a characteristic property witnessed in the magneto-structural transition in Ni-Mn based Heusler alloys with excess Mn.[15]

In the present chapter, the series $Ni_2Mn_{1+x}In_{1-x}$ is investigated. The purpose of carrying forward the study on these Ni-Mn-In alloys is to understand the reason for the sudden appearance of martensitic transition at a critical dopant concentration and to explore the possibility of any pre-transition phases like strain glass around this critical region. To this effect, a careful study of the local and average structure and magnetic properties around the critical concentration is carried out with a particular focus on the

compositions $Ni_2Mn_{1.32}In_{0.68}$, $Ni_2Mn_{1.35}In_{0.65}$, $Ni_2Mn_{1.38}In_{0.62}$ and $Ni_2Mn_{1.4}In_{0.6}$.

5.2 Results

5.2.1 Structure : X-ray diffraction studies

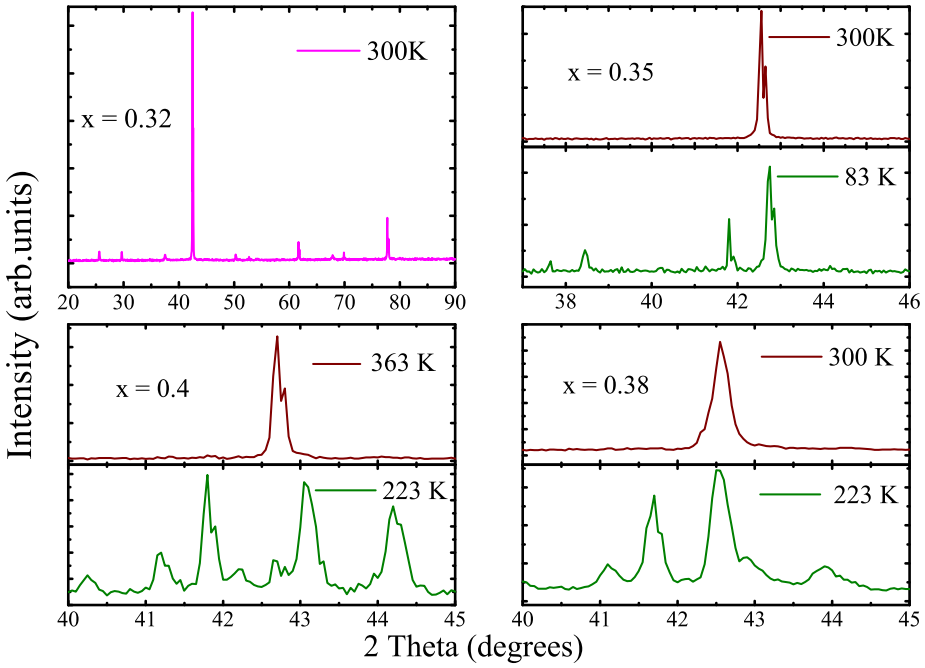

Figure 5.1: X-ray diffraction patterns for the alloys in the series $Ni_2Mn_{1+x}In_{1-x}$.

The temperature dependent x-ray diffraction data recorded down to 80 K is presented in Fig.5.1. The alloy $x = 0.32$ exhibits cubic structure at 300 K and retains its austenitic behaviour at all the measured temperatures. The diffraction patterns for the subsequent alloys are shown in limited 2 theta range ($36 \leq 2\theta \leq 46$) around the 220 Bragg reflection at different temperatures highlighting the evolution of phases. Below 100 K, additional Bragg peaks appear in the diffraction pattern of the alloy $x = 0.35$ indicating a martensitic transition. The martensitic phase coexists with the high temperature cubic austenitic

phase down to the lowest temperature studied here. Contrary to this, the alloys $x = 0.38$ and $x = 0.4$ completely transform into martensite as the temperature is lowered below their respective martensitic finish temperatures M_S

5.2.2 Magnetic property measurements : DC Magnetization

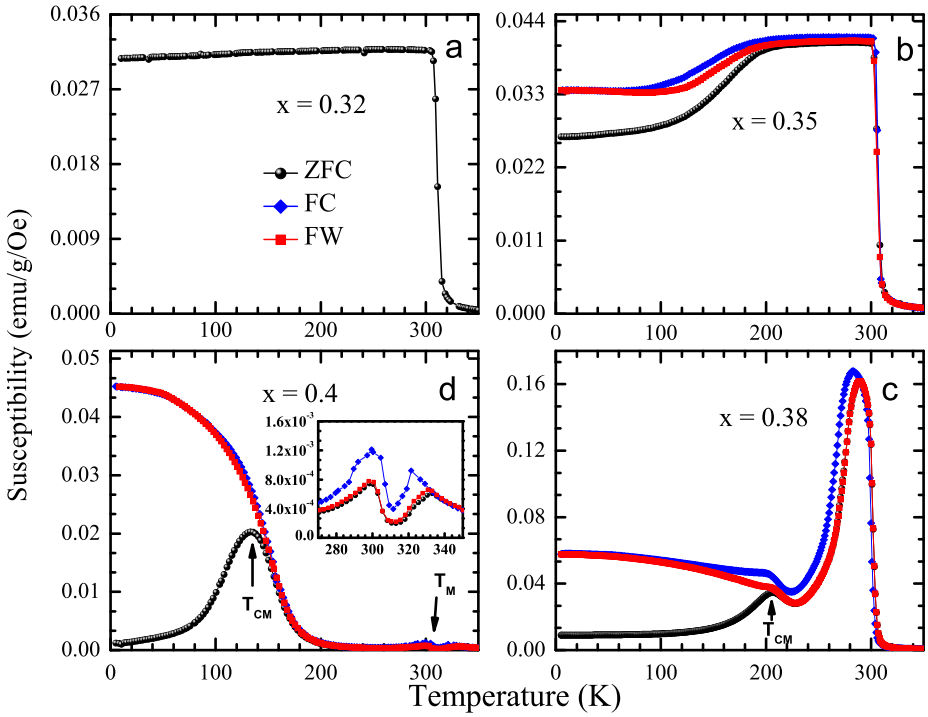

Figure 5.2: Susceptibility as a function of temperature for the alloys $Ni_2Mn_{1+x}Z_{1-x}$, $x = 0.32$, $x = 0.35$, $x = 0.38$ and $x = 0.4$ shown in a, b, c and d respectively during warming after cooling in zero field (ZFC), and subsequent cooling (FCC) and warming (FCW) cycles displaying martensitic transition.

The magnetization measurements as a function of temperature M(T) were achieved in the applied magnetic field of 50 Oe for the alloys $x = 0.32$ and $x = 0.35$, in 100 Oe for the alloy $x = 0.38$ and in 200 Oe for the alloy $x = 0.4$. A steep rise in susceptibility (χ = M/H) is witnessed in the alloy $x = 0.32$ (Fig. 5.2 (a)) below its T_C illustrating the ferromagnetic nature. The ferromagnetic behavior is also observed in the alloy $x =$

0.35 (Fig. 5.2 (b)) which experiences a decrease in the susceptibility below 200 K. This decrease can be ascribed to the occurrence of a partial first order transition, evident from the hysteresis seen in the FCC and FCW magnetization cycles. The susceptibility of the alloy $x = 0.38$ (Fig. 5.2 (c)) decreases sharply and then increases to display a maximum at $T_{CM} = 206$ K due to martensitic transition. Below this temperature, a divergence is seen in the ZFC and FC curves. The ZFC data decreases with further lowering of temperature while a weak increase is noticed in the FC data. Although the martensitic transition in the $x = 0.4$ alloy occurs in the paramagnetic state at $T_M = 333$ K, its χ(T) behavior in the martensitic state is akin to the alloy $x = 0.38$ (Fig. 5.2 (d)). In the alloy $x = 0.4$, the ZFC magnetization curve displays a peak at $T_{CM} = 135$ K before approaching zero at lower temperatures. While the FC curves rise continuously giving the impression of a blocking temperature. It is pertinent to note that with an increase in excess Mn concentration, T_{CM} decreases indicating a weakening of ferromagnetic interactions. In fact, in the alloy $x = 0.5$, T_{CM} is identified to be 39 K reported in Fig 4.9 in chapter 4.

5.2.3 Structure : Neutron diffraction studies

The magnetostructural properties were further addressed by carrying out the temperature-dependent time of flight neutron powder diffraction experiments for the alloys as shown in Fig. 5.3, Fig. 5.4 and Fig. 5.5. The alloy $x = 0.32$ (Fig. 5.3) exhibits austenitic behavior throughout the investigated temperature range. Below T_C, ferromagnetic behavior is witnessed with the major contribution to the ferromagnetic moment coming from the Mn atoms. The temperature-dependent curve of the magnetic moment for Mn atoms

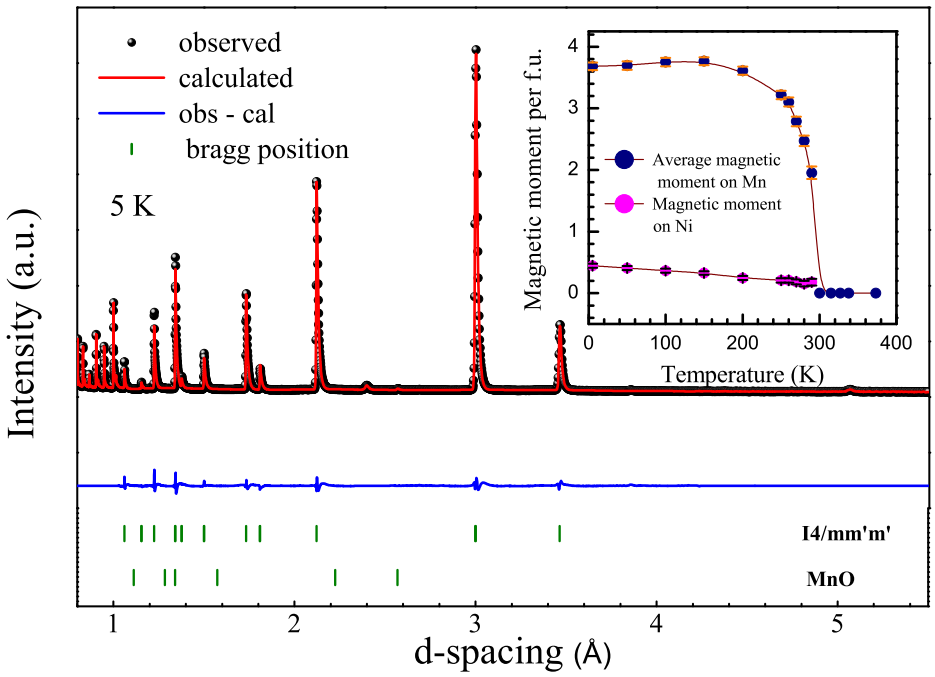

Figure 5.3: Rietveld refined neutron diffraction data of the alloy $x = 0.32$ at 5 K. Inset shows the variation of the average magnetic moment on the Mn and Ni atoms with temperature.

shown in the inset of Fig. 5.3 asserts a behavior following the temperature-dependent magnetization curve shown in Fig. 5.2 (a). The neutron diffraction data of the alloy $x = 0.35$ (Fig. 5.4) portrays the presence of two structural phases below 200 K. The martensitic phase manifested by the two peaks (marked as $*$) on either side of the (101) peak gradually grow at the expense of austenitic phase as the temperature is lowered and accounts for $\sim 12\%$ of the total phase fraction at all temperatures T < 50 K. The values of the magnetic moment obtained from neutron diffraction for both $x = 0.32$ and $x = 0.35$ are in agreement with the respective magnetization behavior of these alloys. Fig. 5.5 depicts the diffraction patterns in the austenitic and martensitic phases of the alloy $x = 0.4$. In the martensitic phase, the alloy transforms into an incommensurate 7M modulated

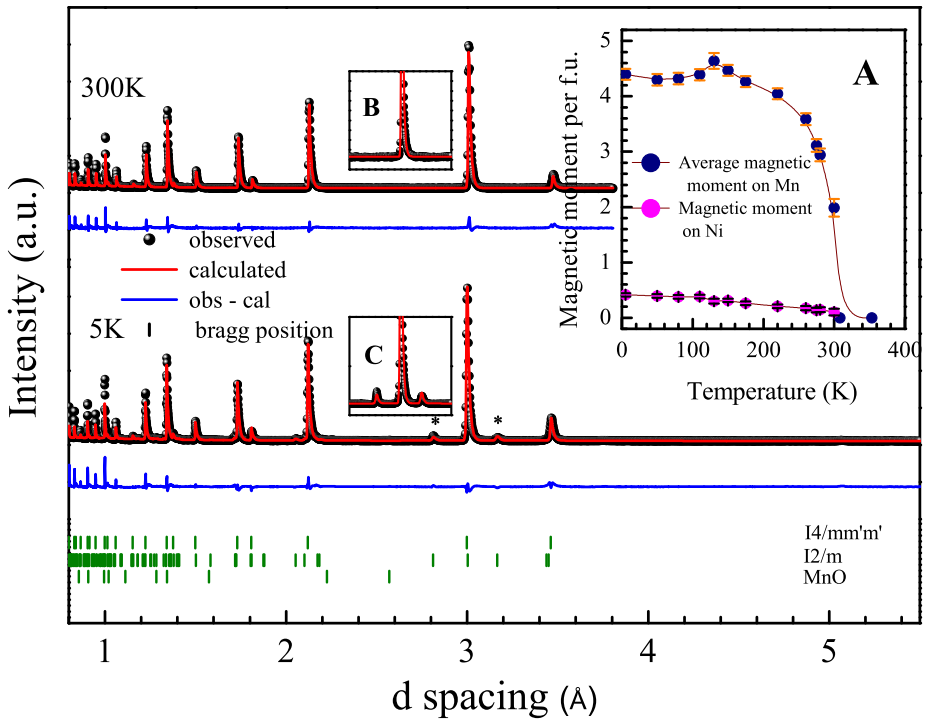

Figure 5.4: Rietveld refined neutron diffraction data of the alloy $x = 0.35$ at two different temperatures, 300 K (austenite) and 5 K (austenite with 12% martensite). Insets C highlights the growth of peaks intrinsic to martensitic phase with decrease in temperature while Inset A shows the variation of the average magnetic moment on the Mn and Ni atoms with temperature.

monoclinic structure with zig-zag modulations from a cubic $L2_1$ structure in the austenitic phase. Contrary to $x = 0.35$, the alloy $x = 0.4$ transforms completely to the martensitic state. The neutron diffraction analysis suggests the presence of a magnetic moment on Mn atoms be about 1.18 μB at 5 K which appears to be in contrast with magnetization measurements. This implies the presence of randomly oriented ferromagnetic clusters resulting in a net-zero magnetization given the fact that neutron diffraction is a local probe, while magnetization measures an average effect. On the other hand, the large irreversibility is seen between FC and ZFC susceptibility curves below T_{CM} in Fig. 5.2(d) that supports the presence of competing for magnetic interactions leading to frustration

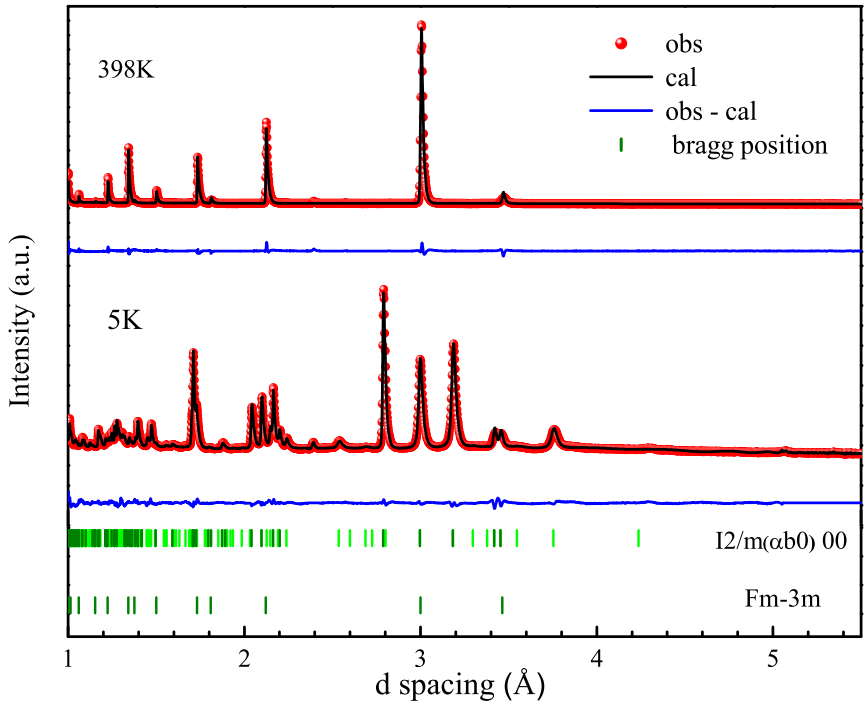

Figure 5.5: Rietveld refined neutron diffraction data in the austenitic phase (398 K) and the martensitic phase (5 K) for the alloy $x = 0.4$.

and glassy behavior.[16–18] The refinement results for the alloy $x = 0.32$ are presented in the tables 5.1 and 5.2 while tables 5.1, 5.3 and 5.4 summarize the data for the alloy $x = 0.35$. Tables 5.5 and 5.6 display results for the alloy $x = 0.4$.

5.2.4 Magnetic properties : AC Magnetization and M-H measurements

The temperature dependent ac susceptibility measurements were performed at various frequencies presented in Fig. 5.6 to further probe the nature of the magnetic state in the present alloys. No frequency dependence of a ac susceptibility signal is seen in the alloy $x = 0.35$ either at its ferromagnetic transition or at the martensitic transition temperature. Nonetheless, the frequency dependent behaviour of the real part of ac susceptibility, χ'

Table 5.1: Crystallographic data and reliability factors for the alloys $x = 0.32$ and $x = 0.35$ at 5 K

Chemical formula	$\mathbf{Ni_2Mn_{1.32}In_{0.68}}$ **($x = 0.32$)**	$\mathbf{Ni_2Mn_{1.35}In_{0.65}}$ **($x = 0.35$)**
Space group	I4/mm'm'	I4/mm'm'(88%) and I2/m (12%)
Lattice parameters (Å)	a = 4.2442(6) c = 5.9960(2)	a = 4.23790(3) c = 5.99329(3) and
		a = 4.347 (1) b = 4.377 (1) c = 5.619 (1) γ = 93.07(2)
V(Å^3)	108.008(2)	107.636(1) and 106.687(1)
GOF	7.56	7.19
Rp	4.46	5.87
wRp	5.72	6.84

Table 5.2: Atomic positions, atomic displacement parameters and occupancy for the alloy $x = 0.32$ (space group - I4/mm'm') at 5 K

atoms	**Wyckoff positions**	**x**	**y**	**z**	**Uiso(Å^2)**	**Occupancy**	**M$_Z$ (μ_B)**
Ni1	4d	0	0.5	0.25	0.0229(3)	0.125	0.44 (3)
Mn1	2a	0	0	0	0.0229(3)	0.0625	3.86(6)
In1	4c	0	0	0.5	0.0229(3)	0.045361	
Mn2	4c	0	0	0.5	0.0229(3)	0.017139	3.86(6)

is observed at around T_{CM} in the alloys $x = 0.38$ and $x = 0.4$ indicating the possibility of a non-ergodic ground state. Behavior in accordance with Vogel Fulcher law is noted for the peak temperature confirming the presence of a glassy phase in both alloys. The parameter $\delta T_f = \frac{\Delta T_f}{T_f(\Delta \log \nu)}$ determines the frequency dependence in $\chi^{'}$ and is calculated to be 0.01 and 0.02 for the $x = 0.38$ and $x = 0.4$ alloys respectively. These values are larger than those expected for typical spin glass and smaller compared to those expected for a typical superparamagnet.[19,20] A cooperative dynamics due to inter cluster interactions are described by the Vogel Fulcher law, $\tau = \tau_0 \exp(\frac{E_a}{K_B(T_f - T_0)})$ wherein τ_0 is the time constant corresponding to characteristic attempt frequency and is related to the strength

Table 5.3: Atomic positions, atomic displacement parameters and occupancy for the major phase (88%, space group - I4/mm'm') of the alloy $x = 0.35$ at 5 K

atoms	**Wyckoff positions**	**x**	**y**	**z**	**Uiso(Å^2)**	**Occupancy**	**M$_Z$ (μ_B)**
Ni1	4d	0	0.5	0.25	0.0163(3)	0.125	0.41 (3)
Mn1	2a	0	0	0	0.0163(3)	0.0625	4.37(8)
In1	2b	0	0	0.5	0.0163(3)	0.042458	
Mn2	2b	0	0	0.5	0.0163(3)	0.020042	4.37(8)

Table 5.4: Atomic positions, atomic displacement parameters and occupancy for the minor phase (12%, space group - I2/m) of alloy $x = 0.35$ at 5 K

atoms	**Wyckoff positions**	**x**	**y**	**z**	**Uiso(Å^2)**	**Occupancy**
Ni2	4i	0	0.5	0.232205	0.0163(3)	0.5
Mn3	2a	0	0	0	0.0163(3)	0.25
In2	2c	0	0	0.5	0.0163(3)	0.146246
Mn4	2c	0	0	0.5	0.0163(3)	0.103754

of interactions while E_a is the activation energy of the relaxation barriers. The fittings results in the value of τ_0 to be $\sim 10^{-6}$ s and the ratio $\frac{E_a}{K_B}$ to be between 15 to 20 in both the compositions as seen in Fig. 5.7(c) and Fig. 5.7(d). This is indicative of a significant coupling amongst the dynamic entities.[21,22] A strong inter-cluster interactions can give rise to spin-glass like cooperative freezing, and in this case, the frequency dependence of peak in $\chi^{'}$ is expected to follow the power law divergence of the standard critical slowing down given by dynamic scaling theory, $\frac{\tau}{\tau^*} = (\frac{T_f}{T_g} - 1)^{-z\nu^{'}}$ wherein τ represents the dynamical fluctuation time scale corresponding to measurement frequency at the peak temperature of $\chi*$, τ^* is the spin flipping time of the relaxing entities, T$_g$ is the glass transition temperature in the limit of zero frequency, z is the dynamic scaling exponent, and $\nu^{'}$ is the critical exponent. In the vicinity of glass transition, the spin cluster correlation length ξ diverges as $\xi \propto (\frac{T_f}{T_g} - 1)^{-\nu^{'}}$ and the dynamic scaling hypothesis relates τ

Table 5.5: Crystallographic data and reliability factors for the alloy $x = 0.4$ at 5 K

Chemical formula	$\mathbf{Ni_2Mn_{1.4}In_{0.6}}$ **(x = 0.4)**
Space group	I2/m($\alpha\beta$0)00
Lattice parameters (Å)	Modulation vector q = - 0.3358(4) a = 4.4059 (1) b = 4.33333 (9) c = 5.57471 (8) γ = 93.49(2)
V(Å^3)	106.24(3)
GOF	5.72
Rp	3.31
wRp	4.01

Table 5.6: Atomic positions, atomic displacement parameters and occupancy of the alloy $x = 0.4$ at 5 K

atoms	**Wyckoff positions**	**x**	**y**	**z**	**Uiso(Å^2)**	**Occupancy**	**M$_Z$ (μ_B)**
Ni1	4i	-0.5	0	-0.748668	0.0210(2)	0.5	
Mn1	2c	0	0	-0.5	0.0163(3)	0.25	1.2(2)
In1	2a	0	0	0	0.0163(3)	0.143	
Mn2	2a	0	0	0	0.0163(3)	0.107	1.2(2)
					xslope = 0.146(7)	x40 = 0.01(2)	delta = 0.99(1)

to ξ as $\tau \sim \xi^z$.[23,24] The results of the best fits obtained for the $x = 0.38$ and $x = 0.4$ alloys are shown in Fig. 5.7(a) and Fig. 5.7(b) respectively. Here, T$_g$ is taken as the abscissa of the $ln(\nu)$ Vs T$_f$ plots shown in Fig. 5.6. The value of τ^* are 2.3×10^{-12}s and 7.9×10^{-11}s and the values of $z\nu'$ are 4.8 and 4.7 respectively for $x = 0.38$ and $x = 0.4$ alloys. Such values have been reported in Ni-Mn alloys and are characterized as super spin glass systems.[25–27]

The frequency dependence around T_{CM} in ac susceptibility following Vogel Fulcher law and scaling law advocates the presence of a glassy phase along with significant inter cluster interactions in the $x = 0.38$ and $x = 0.4$ alloys. These alloys seem to have ferromagnetic

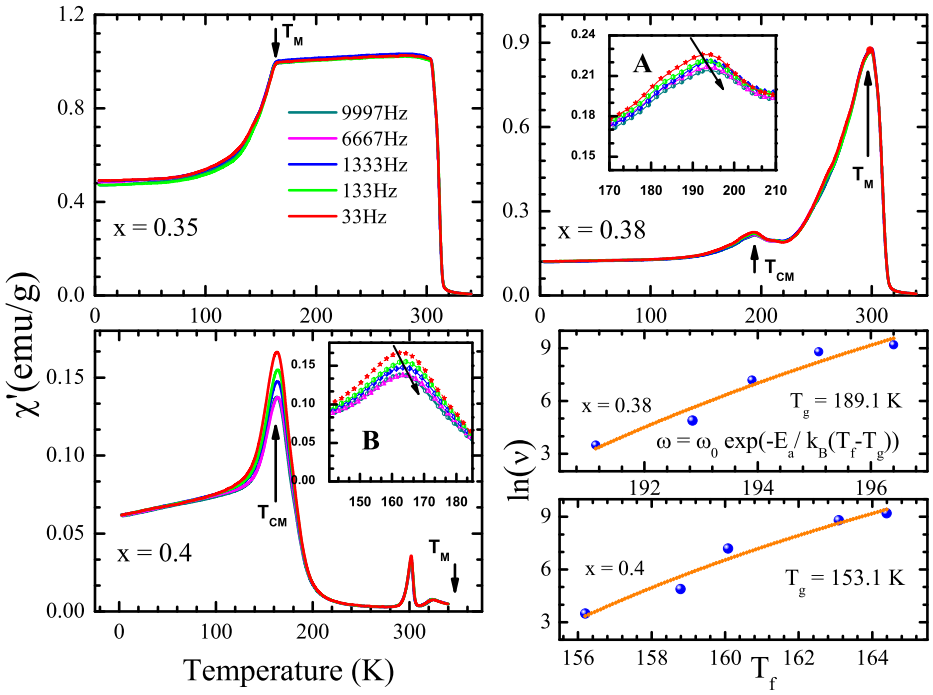

Figure 5.6: Temperature dependent measurements of the real part of ac susceptibility for the three alloys $x = 0.35$, 0.38 and 0.4 at different frequencies. Frequency dependent behaviour of T_{CM} is seen in the insets A and B for the alloys $x = 0.38$ and 0.4 respectively following Vogel Fulcher law.

and non-ferromagnetic clusters that are actively interacting with each other leading to a glassy ground state and exhibit critical slowing down as expected from dynamical scaling theory.

A better understanding of the magnetic ground state can be achieved by studying the shape of the hysteresis loop. Hence M(H) data was recorded st 5 K for the alloy compositions $x = 0.35$, $x = 0.38$ and $x = 0.4$ featured in Fig.5.8 while Fig.5.9 reflects the expanded view of the ZFC M(H) plots in the field interval of ± 400 Oe. In the alloys $x = 0.32$ and $x = 0.38$, the ZFC hysteresis loop is present firmly around the center of the axis and the virgin curve is traced within the loop Fig.5.9. Contrary to this, in the

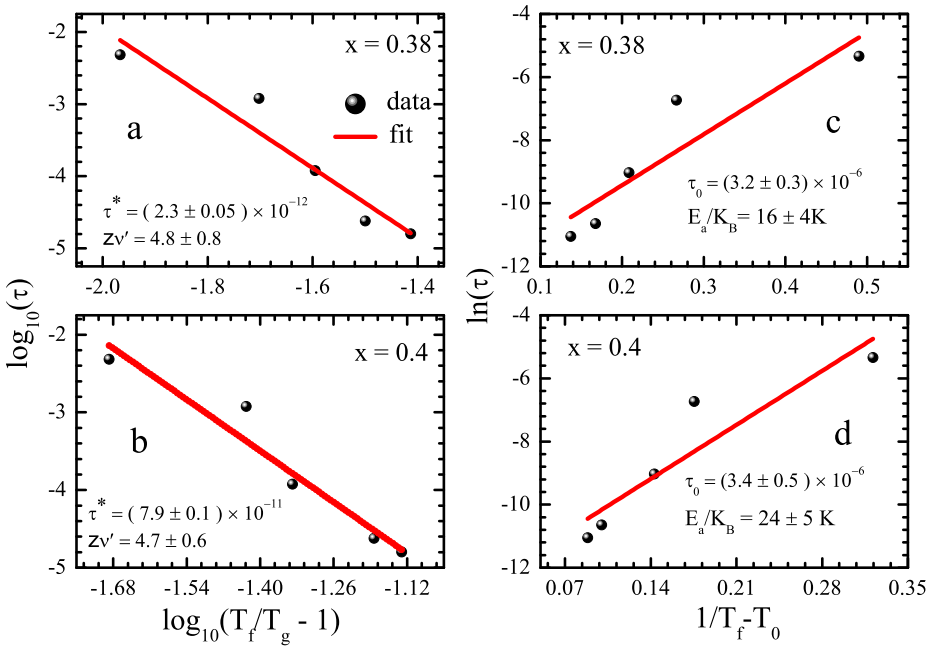

Figure 5.7: The plots marked a and b give the best fits to the equation $\tau = \tau^*(\frac{T_f}{T_g} - 1)^{-z\nu'}$ for the alloys $x = 0.38$ and $x = 0.4$ respectively while the Vogel Fulcher relation $\tau = \tau_0 \exp(\frac{E_a}{K_B(T_f - T_0)})$ is shown in graphs marked as c and d for the two alloys.

alloys $x = 0.38$ and $x = 0.4$, the loop appears to be displaced vertically up and down respectively with the virgin curve lying outside the loop. This behaviour is attributed to the presence of ferromagnetic and antiferromagnetic interacting clusters.[28] In the alloy $x = 0.38$, the coupling between ferromagnetic and antiferromagnetic clusters seems to be favorable in the +H direction by virtue of which the magnetization assumes a higher magnitude in that direction and the loop appears to be shifted up. While in the alloy $x = 0.4$, the situation appears to be reversed resulting in the loop shifting down. The value of exchange bias field increases from -78.96 Oe in $x = 0.38$ to -149.23 Oe in $x = 0.4$. The existence of exchange bias in M(H) loops assures the presence of both ferromagnetic and antiferromagnetic interactions while the increasing values of the exchange bias field with

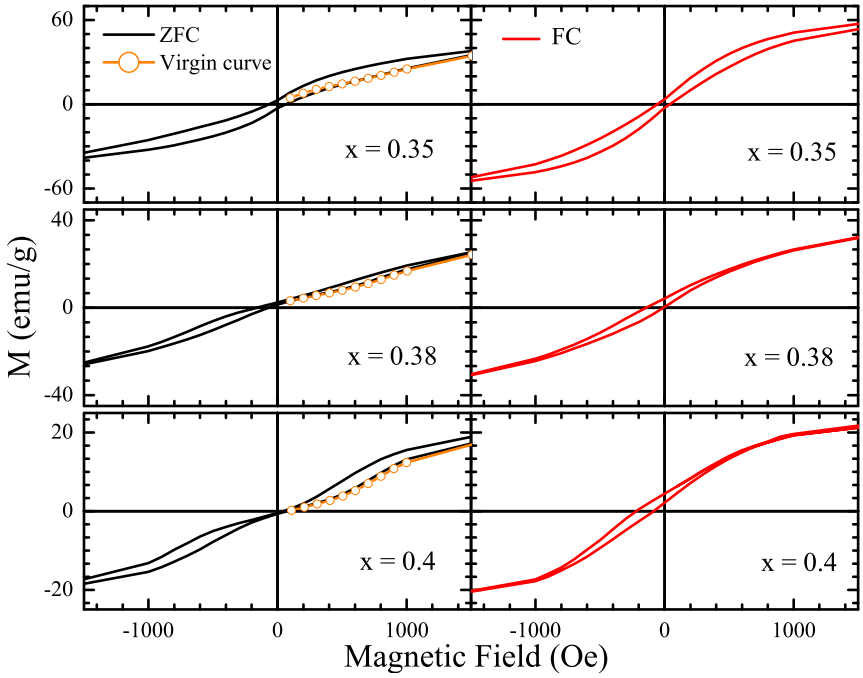

Figure 5.8: Magnetization as a function of applied field at 5 K for the three alloys x = 0.35, 0.38 and 0.4. The dotted line in orange represents virgin curve.

increasing Mn excess content indicates the growth of antiferromagnetic clusters in these alloys.

5.2.5 Mechanical properties

To correlate the existence of magnetic glass with a possible presence of strain glass, the alloys $x = 0.35$ and $x = 0.38$ were further investigated for frequency dependent elastic properties by performing the dynamical mechanical analyzer (DMA) studies in the temperature range of 100 K to 400 K. No frequency dependence of storage modulus or loss were visible over a frequency range 0.1 Hz to 7 Hz ruling out the possibility of the existence of the strain glass in these alloys. Fig.5.10 displays the DMA plots in the alloy $x = 0.38$ at different frequencies featuring martensitic transition and absence of strain

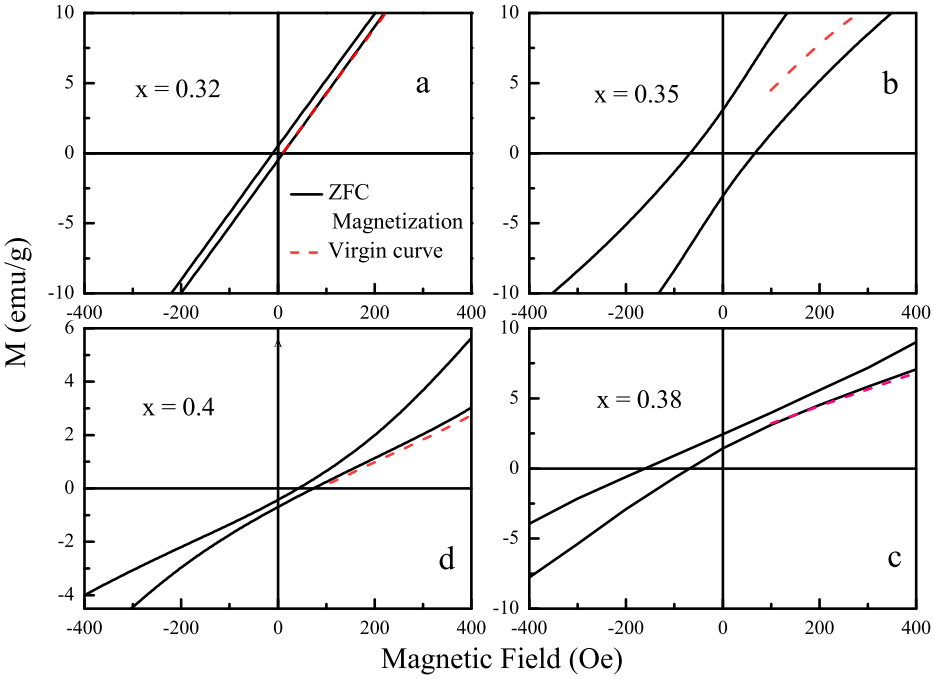

Figure 5.9: The expanded view of ZFC magnetization displaying the behavior of the hysteresis loop around zero field for the alloy compositions.

glass.

5.2.6 Local structure: EXAFS studies

In the $Ni_2Mn_{1+x}In_{1-x}$ alloys, the RKKY interactions between the Mn atoms in its own sublattice are responsible for the ferromagnetic interactions[16] while the exchange type interaction between Mn_Y (Mn in its sublattice) and Mn_Z (Mn at In site) atoms mediated via Ni atom give rise to antiferromagnetic correlations.[29] Interestingly, the Mn excess alloys exhibit local structural distortions even in the austenitic phase.[14] This propels careful study of the local structure for a better understanding of magneto-structural properties.

Hence, EXAFS data analysis was carried out in the temperature range of 50 K to 300 K for all the four alloy compositions at both Ni K and Mn K edges. EXAFS data at Ni

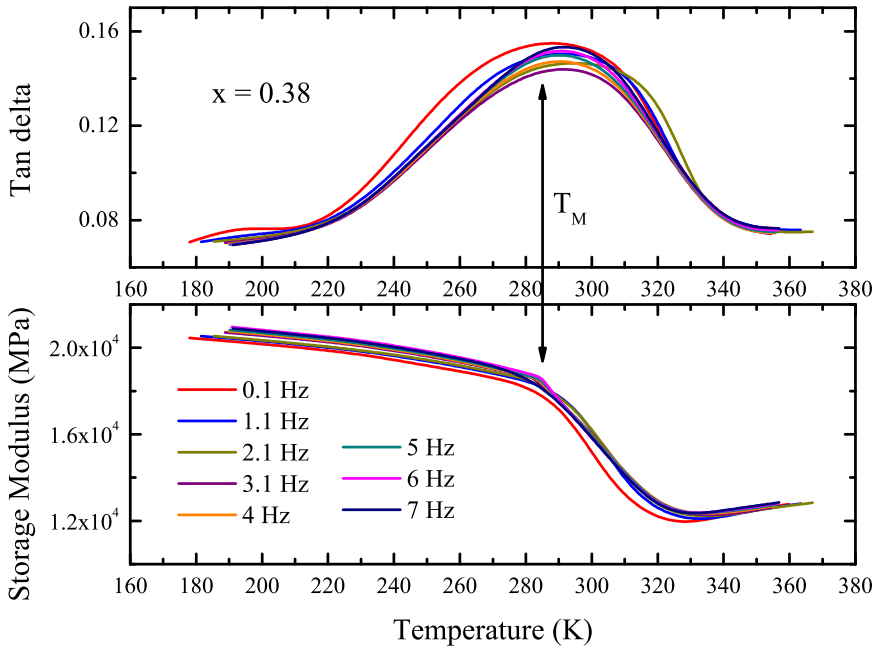

Figure 5.10: Temperature dependence of ac storage modulus and $tan\delta$ measurement in the alloy $x = 0.38$.

and Mn K edges were analyzed together using a common structural model. The analysis was performed using 14 independent parameters. The amplitude reduction factor (S_0^2) for the two data sets were obtained from the analysis of respective metal foils and were kept fixed during the analysis. Fig. 5.11 depicts the magnitude of Fourier transform (FT) of Ni K edge EXAFS spectra in all the alloy compositions at 50 K. It comprises of contribution from the nearest neighbours Mn and In atoms at $\sim$ 2.5 Å with their coordination number fixed as per the composition ratio and from the next nearest neighbour Ni atoms ($\sim$ 3.0 Å). Similarly, Fig. 5.12 displays the spectra at Mn edge, which are fitted considering the nearest neighbour, Ni ($\sim$ 2.5 Å), the next nearest neighbour, In and Mn_Z ($\sim$ 3.0 Å) and the third neighbour, Mn_Y at ($\sim$ 4.2 Å) as backscattered atoms. Best fits at all temperatures

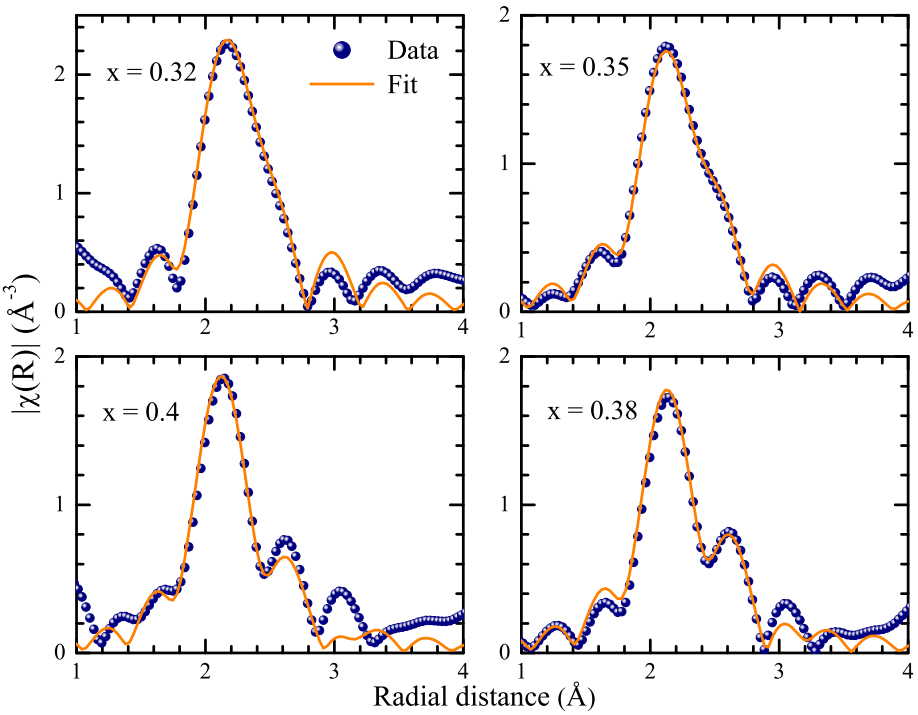

Figure 5.11: Magnitude of the Fourier transformed EXAFS spectra obtained at Ni K edge in the alloy compositions at 50 K

were obtained only after relaxing the constraints imposed by the cubic austenitic structure as described earlier.[12] Fig. 5.13 presents the variation of bond distances with temperature in the four alloy compositions. It can be seen that irrespective of excess Mn content, the nearest neighbour Ni–Mn distance is shorter than the Ni–In the bond distance. The bond distances, Mn_Y–In and Mn_Y–Mn_Z are almost equal in the alloys $x = 0.32$ and $x = 0.35$, which is in accordance with their cubic crystal structure. Here Mn_Y represents Mn in its sublattice while Mn_Z represents Mn in Z (In) sublattice of X_2YZ Heusler structure. These structural distortions emerge due to the replacement of In atoms by relatively smaller Mn atoms. The shorter Ni–Mn distance and the nearly equal Mn_Y–In and Mn_Y–Mn_Z distances indicate that these distortions are restricted only to nearest neighbour

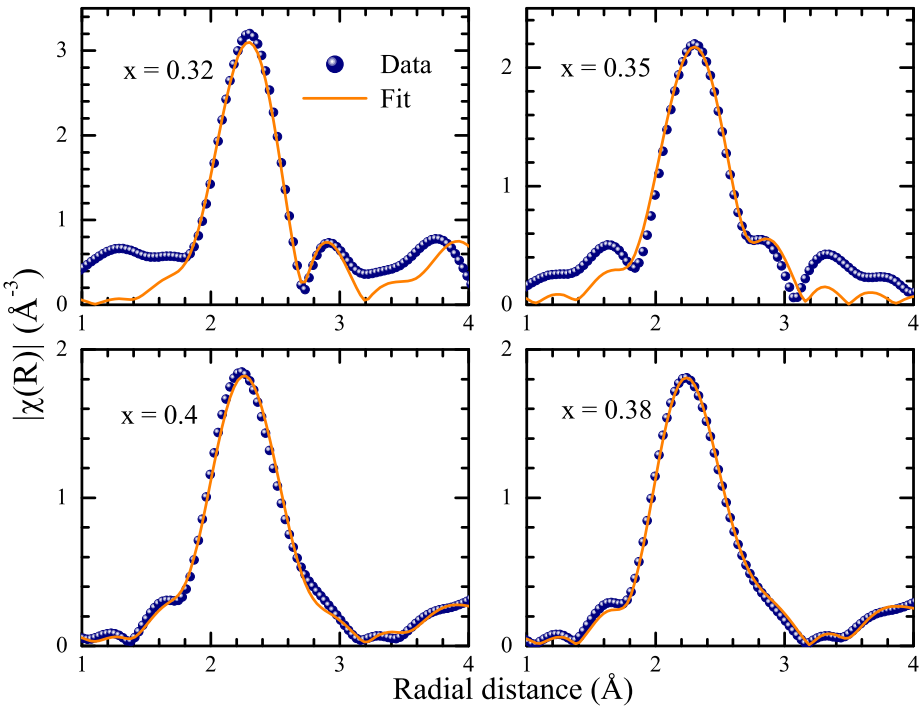

Figure 5.12: Magnitude of the Fourier transform of the Mn K edge EXAFS spectra in the alloy compositions at 50 K

correlations. With the increase in Mn excess concentration beyond $x = 0.35$, the Mn_Y–Mn_Z distance exceeds Mn_Y–In bond distance especially in the martensitic phase implying the release of structural strain along with the lowering of crystal symmetry. A comparison of the third neighbour distance Mn_Y–Mn_Y with the Mn_Y–Mn_Z at 50 K is presented in Fig. 5.14 in the wider range $0.3 \leq x \leq 0.5$, of excess Mn content. It can be seen that the Mn_Y–Mn_Y distance increases rapidly in the alloys undergoing martensitic transition while the Mn_Y–Mn_Z bond distance nearly remains constant throughout the concentration range.

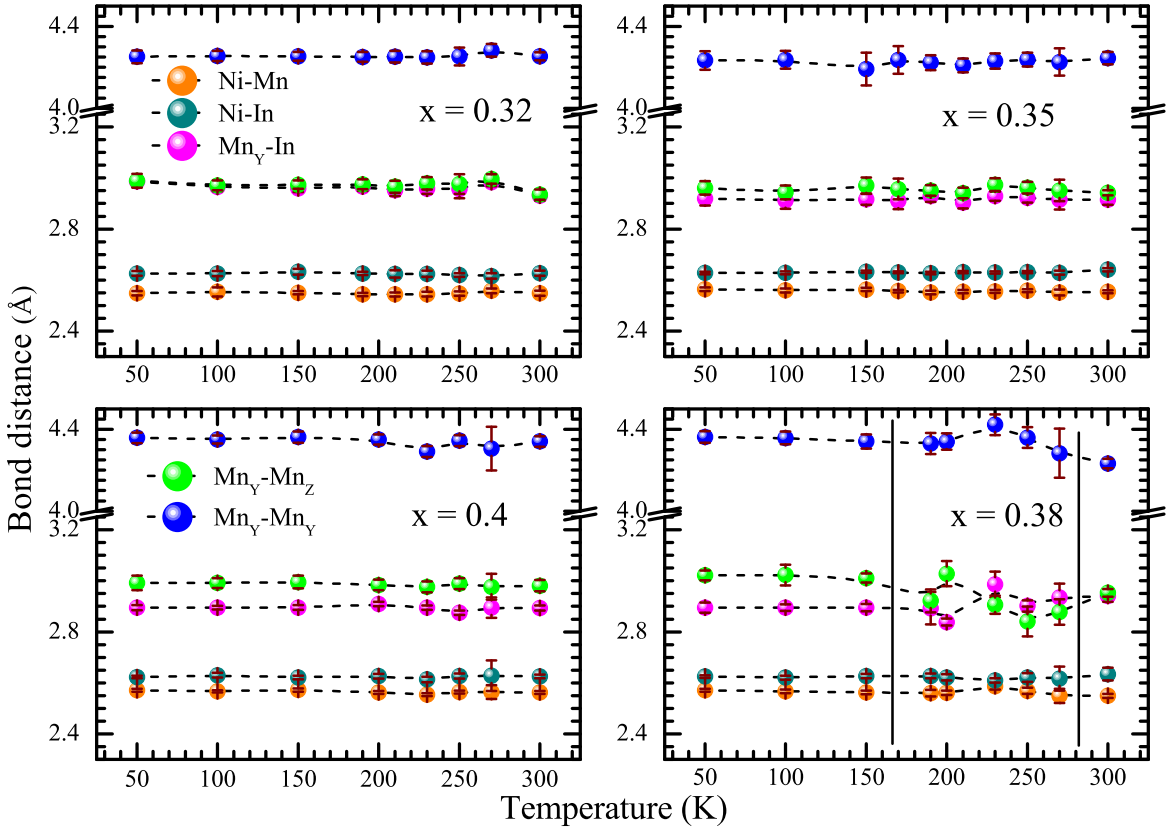

Figure 5.13: Variation of bond distances with temperature for the alloy compositions. The oscillations in bond distances seen in the alloy $x = 0.38$, within the region marked by two solid lines highlights the martensitic transformation.

5.3 Discussion

The present study illustrates the occurrence of martensitic transition in the alloys $Ni_2Mn_{1+x}In_{1-x}$ with the increase in Mn excess concentration at a critical value of $x = 0.35$. Although the alloy has only about 12% of its total phase fraction transforming to the martensitic state, alloys with slightly higher Mn concentration ($x \geq 0.38$) transform completely to the martensitic state. The martensitic structure evolves from 7M monoclinic structure to an incommensurate 7M structure with zig-zag modulations in $x = 0.4$ alloy. No signatures of any pre-transformation structural changes are noticed,

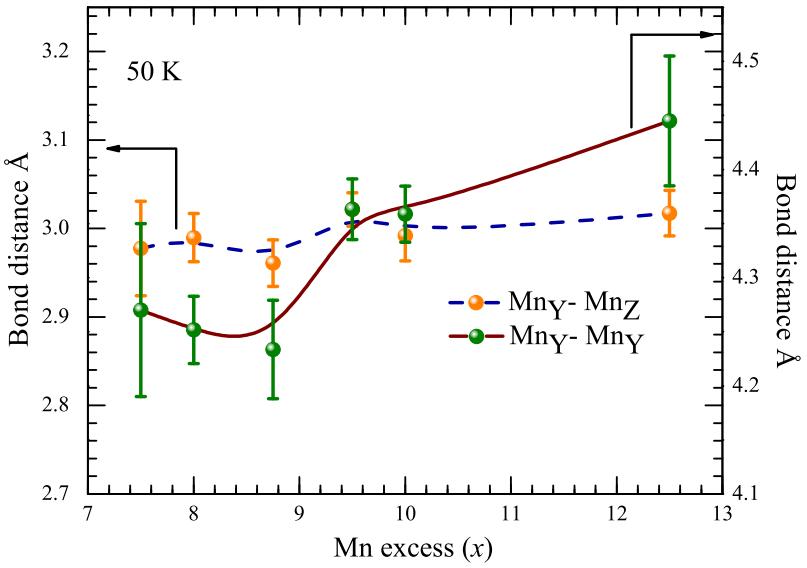

Figure 5.14: Variation of Mn-Mn bond distances with Mn excess concentration x at 50 K

either in the transforming alloys ($x \geq 0.35$) or in compositions with x just below the critical concentration.

Concomitant with this structural transition, there are drastic changes in the magnetic properties. In the alloy compositions undergoing martensitic transition ($x \geqslant 0.38$), the ZFC and FC curves exhibit an increase in magnetization followed by a reversal behaviour below the characteristic temperature T_{CM}. Further increase in Mn content results in the decrease in T_{CM} indicating a weakening of ferromagnetism which is unanimous with the magnetic moment values on Mn from $x = 0.35$ to $x = 0.4$ as seen from neutron diffraction measurements. However, there is a ground state transformation from an ordered ferromagnet to a glassy state with ferromagnetic and antiferromagnetic spin clusters. The exchange bias field is present in the alloys which increase with increasing Mn con-

tent. The decrease in T_{CM} and increasing exchange bias field suggests the growth of antiferromagnetic clusters at the expense of ferromagnetic clusters. It appears that these competing ferromagnetic and antiferromagnetic clusters further give rise to a super spin glassy ground state.

With the addition of Mn at the expense of In, there is a strain build up due to the size difference of Mn and In atoms occupying the Z site of the Heusler structure. The cubic symmetry of the austenitic Heusler structure demands Ni–Mn and Ni–In bond distances to be equal. However, the EXAFS analysis indicates Ni–Mn bond distance to be shorter than the Ni–In bond distance in all non-stoichiometric, $Ni_2Mn_{1+x}In_{1-x}$ alloys. The cubic austenitic order is preserved by nearly equal next nearest neighbor Mn_Y–In and Mn_Y–Mn_Z bond distances. Such a structural distortion develops a lattice strain which is relieved by an undergoing martensitic transformation beyond the critical concentration of Mn replacing In at the Z sites. With the onset of martensitic transition, the difference between Mn_Y–Mn_Z and Mn_Y–In bond distances is also visible. Beyond the critical concentration ($x = 0.35$), Mn_Y–Mn_Y bond distance exhibit a relatively rapid increase which reflects the strain relaxation above the critical value. It appears that the ability of the Heusler structure to adapt to the strain caused by the size difference between In and doped Mn atoms is perhaps the reason for the absence of any non ergodic structural pre-transition phases like strain glass in $Ni_2Mn_{1+x}In_{1-x}$ alloys.

Further, the magnetic measurements imply the growth of antiferromagnetic clusters at the expense of ferromagnetic clusters. Fig.5.14 suggests that with increasing Mn content,

the Mn_Y–Mn_Z bond distance nearly remains invariant while the Mn_Y–Mn_Y bond distance shows an abrupt increase beyond a critical value. The increasing Mn_Y–Mn_Y bond distance signifies weakening of ferromagnetism while the invariance in Mn_Y–Mn_Z bond distance imply that the interactions between Mn_Y and Mn_Z alone are not responsible for antiferromagnetic behaviour. In fact, Neutron diffraction measurements on Co doped Ni-Mn-Ga alloys have attributed the antiferromagnetic interactions to the Ni atoms at the X site of the X_2YZ Heusler structure.[15] XMCD studies also highlight the role of Ni in the emergence of antiferromagnetism in Mn rich Heusler alloys.[29] The role of Ni atoms in the antiferromagnetic interactions coupled with the observed Ni-Mn bond distance to be shorter than Ni-In distance hints towards the possibility of formation of two structural variants at the local level, the ferromagnetic Ni_2MnIn and the antiferromagnetic Ni_2Mn_2. Temper annealing of $Ni_2Mn_{1+x}In_{1-x}$ alloys have shown the disintegration of the modulated martensitic structure into Heusler $L2_1$ and tetragonal $L1_0$ phases.[30,31] The local segregation of different structural variants could be responsible for the observed ferromagnetic and antiferromagnetic clusters leading to a super spin glassy ground state. For a better understanding of these aspects, the $Ni_2Mn_{1+x}In_{1-x}$ alloys were temper annealed for a detailed structural and magnetic study which is described in chapter 6.

5.4 Conclusion

In conclusion, the cubic Heusler structure of $Ni_2Mn_{1+x}In_{1-x}$ has the ability to accommodate the lattice strain caused by the replacement of larger In atom with smaller Mn

atom up to a critical concentration. Beyond the critical value of x, the cubic structure relieves the strain by undergoing a martensitic transition. Along with this structural relaxation process, the magnetic ground state transits from a ferromagnetically ordered to a super spin glass state with antiferromagnetic and ferromagnetic clusters. Even though the increasing Mn content results in a non-ergodic magnetic ground state, the ferroelastic transition retains its ergodicity. This appears to be due to the ability of the Heusler structure to accommodate strain and retain ferromagnetism in $Ni_2Mn_{1+x}In_{1-x}$ alloys.

References

[1] E. Kren, E. Nagy, L. Pal, and P. Szabo. *J. Phys. Chem. Solids*, 29:101–108, 1968.

[2] Y. Sutou, Y. Imano, N. Koeda, T. Omori, R. Kainuma, K. Ishida, and K. Oikawa. *Appl. Phys. Lett.*, 85:4358, 2004.

[3] A. Planes, L. Mañosa, and M. Acet. *J.Phys.: Condens Matter*, 21:233201, 2009.

[4] S. Aksoy, T. Krenke, M. Acet, E. F. Wassermann, X. Moya, L. Mañosa, and A. Planes. *Appl. Phys. Lett.*, 91:241916, 2007.

[5] M. Siewert, M. E. Gruner, A. Hucht, H. C. Herper, A. Dannenberg, A. Chakrabarti, N. Singh, R. Arróyave, and P. Entel. *Advanced Engineering Materials*, 14:530–546, 2012.

[6] P. Entel, M. E. Gruner, D. Comtesse, and M. Wuttig. *JOM*, 65:1540–1549, 2013.

[7] M. Ye, A. Kimura, Y. Miura, M. Shirai, Y. T. Cui, K. Shimada, H. Namatame, M. Taniguchi, S. Ueda, K. Kobayashi, R. Kainuma, T. Shishido, K. Fukushima, and T. Kanomata. *Phys. Rev. Lett*, 104:176401, 2010.

[8] L. Righi, F. Albertini, L. Pareti, A Paoluzi, and G. Calestani. *Acta Mater*, 55:5237–5244, 2007.

[9] L. Righi, F. Albertini, E. Villa, A. Paoluzi, G. Calestini, V. Chernenko, S. Besseghini, C. Ritter, and F. Passaratti. *Acta Mater*, 56:4529–4535, 2008.

[10] H. Yan, Y. Zhang, N. Xu, A. Senyshyn, Heinz-Günter Brokmeier, C. Esling, X. Zhao, and L. Zuo. *Acta Mater*, 88:375–388, 2015.

[11] A. Çakir, L. Righi, F. Albertini, M. Acet, and M. Farle. *Acta Mater*, 99:140–149, 2015.

[12] P. A. Bhobe, K. R. Priolkar, and P. R. Sarode. *Phys. Rev. B*, 74:224425, 2006.

[13] P. A. Bhobe, K. R. Priolkar, and P. R. Sarode. *J. Phys.:Condens. Matter*, 20:015219, 2008.

[14] D. N. Lobo, K. R. Priolkar, P. A Bhobe, D. Krishnamurthy, and S. Emura. *Appl. Phys. Lett.*, 96:38006, 2010.

[15] F. Orlandi, S. Fabbrici, F. Albertini, P. Manuel, D. D. Khalyavin, and L. Righi. *Phys. Rev. B*, 94:140409, 2016.

[16] V. D. Buchelnikov, P. Entel, S. V. Taskaev, V. V. Sokolovsky, A. Hucht, M. Ogura, H. Akai, M. E. Gruner, and S. K. Nayak. *Phys. Rev. B*, 78:184427, 2008.

[17] G. Benacchio, I. Titov, A. Malyeyev, I. Peral, M. Bersweiler, P. Bender, D. Mettus, D. Honecker, E. P. Gilbert, M. Coduri, A. Heinemann, S. Mühlbauer, Aslı Çak ır, M. Acet, and A. Michels. *Phys. Rev. B*, 99:184422, 2019.

[18] W. Wu, C. Israel, S. Park N. Hur, S. W. Cheong, and A. de Lozanne. *Nat. Mater*, 5:881, 2006.

[19] C. A. M. Mulder, A. J. van Duyneveldt, and J. A. Mydosh. *Phys.Rev.B*, 25:515, 1982.

[20] J. A. Mydosh. *Spin glasses: An Experimental Introduction.* London Taylor and Francis, 1993.

[21] B. Pallab, K. Somesh, and P. Nath. *Journal of magnetism and magnetic materials*, 497:165977, 2020.

[22] C. Djurberg, P. Svedlindh, P. Nordblad, M. F. Hansen, F. Bødker, and S. Mørup. *Phys. Rev. Lett.*, 79:5154, 1997.

[23] D. Kumar and A. Banerjee. *J. Phys. Condens.Matter*, 25:216005, 2013.

[24] T. Chakrabarty, A. V. Mahajan, and S. Kundu. *J. Phys. Condens.Matter*, 26:405601, 2014.

[25] D. Y. Cong, S. Roth, and Y. D. Wang. *physica status solidi (b)*, 251:2126–2134, 2014.

[26] P. Liao, C. Jing, X. L. Wang, Y. J. Yang, D. Zheng, Z. Li, B. J. Kang, D. M. Deng, S. X. Cao, J. C. Zhang, and B.Lu. *Appl. Phys. Lett.*, 104:092410, 2014.

[27] B. M. Wang, Y. Liu, P. Ren, B. Xia, K. B. Ruan, J. B. Yi, J. Ding, X. G. Li, and L. Wang. *Phys. Rev. Lett.*, 106:077203, 2011.

[28] P. A. Bhobe, K. R. Priolkar, and A. K. Nigam. *J. Phys. D: Appl. Phys*, 41:235006, 2008.

[29] K. R. Priolkar, P. A. Bhobe, D. N. Lobo, S. W. D'Souza, S. R. Barman, Aparna Chakrabarti, and S. Emura. *Phys. Rev. B*, 87:144412, 2013.

[30] A. Çakir, M. Acet, U. Wiedwald, T. Krenke, and M. Farle. *Acta Materialia*, 127:117–123, 2017.

[31] L. Dincklage, F. Scheibel, A. Çakır, M. Farle, and M. Acet. *AIP Advances*, 8:025012, 2018.

Chapter 6

Random packing of Ni_2MnIn and NiMn structural units in off-stoichiometric Ni-Mn-In alloys.

6.1 Introduction

Substitution of Mn in place on In in the Heusler Ni_2MnIn to realize $Ni_2Mn_{1+x}In_{1-x}$ does not result in strain glassy phase. This is due to the ability of the Heusler structure to accommodate strain developed by substitution of Mn in place of In up to a critical concentration of the dopant Mn ($x = 0.35$). However, the magnetic ground state transforms into a super spin glass because of the competing ferromagnetic and antiferromagnetic spin clusters. This series can also be looked upon as In doped $(NiMn)_2$, wherein Ni_2Mn_2 is an antiferromagnet with a tetragonal $L1_0$ martensitic structure below 973 K.[1] Recent studies have shown that Z (Ga, In, Sn, Sb) doped Ni_2Mn_2 alloys, i.e. $Ni_2Mn_{2-y}Z_y$, are structurally metastable, and disintegrate into a dual phase composite alloy consisting of Heusler $L2_1$ and tetragonal $L1_0$ phases upon temper annealing.[2–5] One of the consequences of this metastable structure is the phenomenon of shell ferromagnetism which is observed when theses alloys are annealed in the external magnetic field. Depending

upon the time and temperature of annealing, all the off stoichiometric compositions of $Ni_2Mn_{2-y}Z_y$ ($0 < y < 1$) either completely decompose into the $L2_1$ (Ni_2MnZ) and $L1_0$ (NiMn) phases or supercells.[6] The alloys with lower Z element content disintegrate at a lower temperature and in a lesser time compared to those with higher Z content leading to time dependent effects such as strong atomic relaxation. The phase separation due to decomposition is reported to be lowest in energy and highlights the effect of structural disorder and the segregation of alloys close to martensitic transformation.[7] EXAFS analysis have shown the local structural distortions even in the cubic phase of the off stoichiometric $Ni_2Mn_{2-y}Z_y$ alloys. There is a possibility that these distortions might act as precursors to the observed decomposition on temper annealing. Further, despite local structural disorder and metastable crystal structure absence of a non-ergodic state like the strain glass remains intriguing.

The $L2_1$ structure of Ni_2MnZ (Z = Sn, In or Sb) with $a \sim 6.0$ Åand the $L1_0$ unit cell of NiMn ($a = 3.7$ Å, $c = 3.5$ Å) have significantly different near neighbor distances. Therefore, it should be possible to understand the structural disintegration of an off stoichiometric $Ni_2Mn_{2-y}Z_y$ alloys into Ni_2MnZ and NiMn phases. It is also equally important to understand the role of structural distortions present in the off stoichiometric alloys in facilitating their dissociation into the two end members with $L2_1$ and $L1_0$ structures. To understand these aspects, the alloys $Ni_2Mn_{2-y}In_y$ $0 \leq y \leq 1$ are prepared by rapid quenching and are further temper annealed to be compared with their rapidly quenched counterparts through a detailed structural and magnetic study. All the alloy compositions

were given exactly the same temper annealing treatment (427 °C for $\sim 10^5$ seconds) to understand the process of disintegration and the associated changes in their structure and properties.

6.2 Results

6.2.1 Structure : Xray diffraction studies

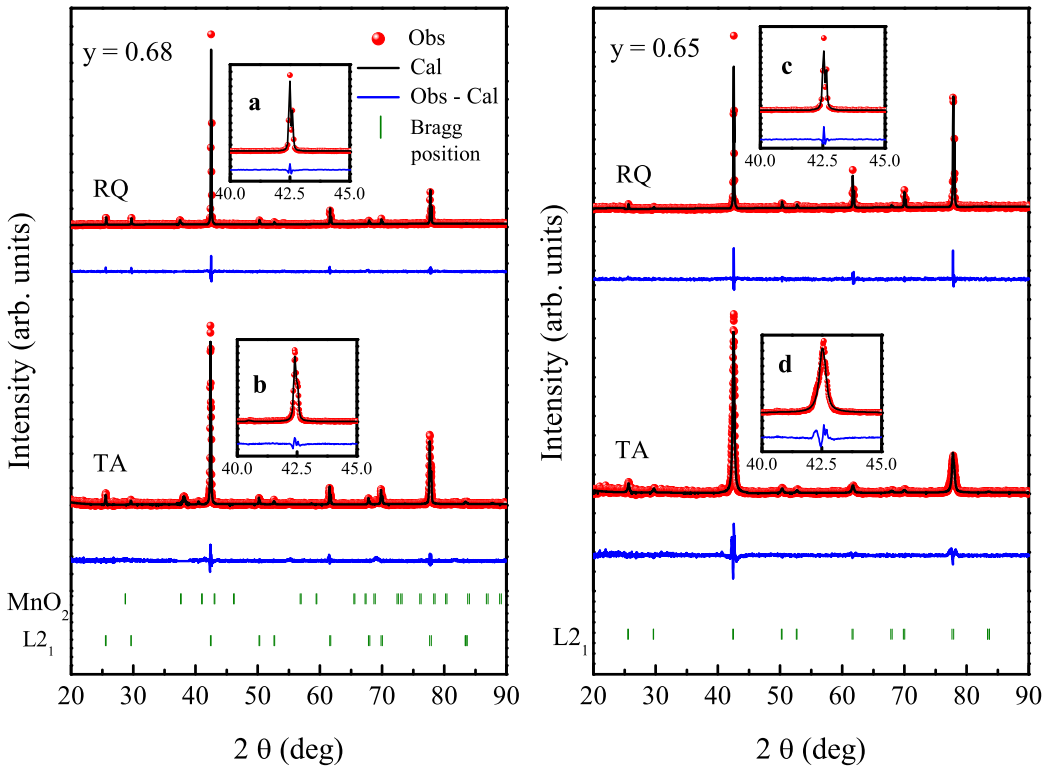

Figure 6.1: X-ray diffraction data for the alloys $y = 0.68$ and $y = 0.65$ at 300 K. The broadening of major 220 peak is highlighted in rapid quenched (RQ) as inset (a) and temper annealed (TA) as inset (b) in $y = 0.68$ and as insets (c) (RQ) and (d) (TA) in $y = 0.65$.

The x-ray diffraction measurements were performed at 300 K on the rapid quenched (RQ) and the temper annealed (TA) alloys and the phases were identified using the Lebail method. Fig. 6.1 displays the diffraction patterns of the alloys $y = 0.68$ and $y =$

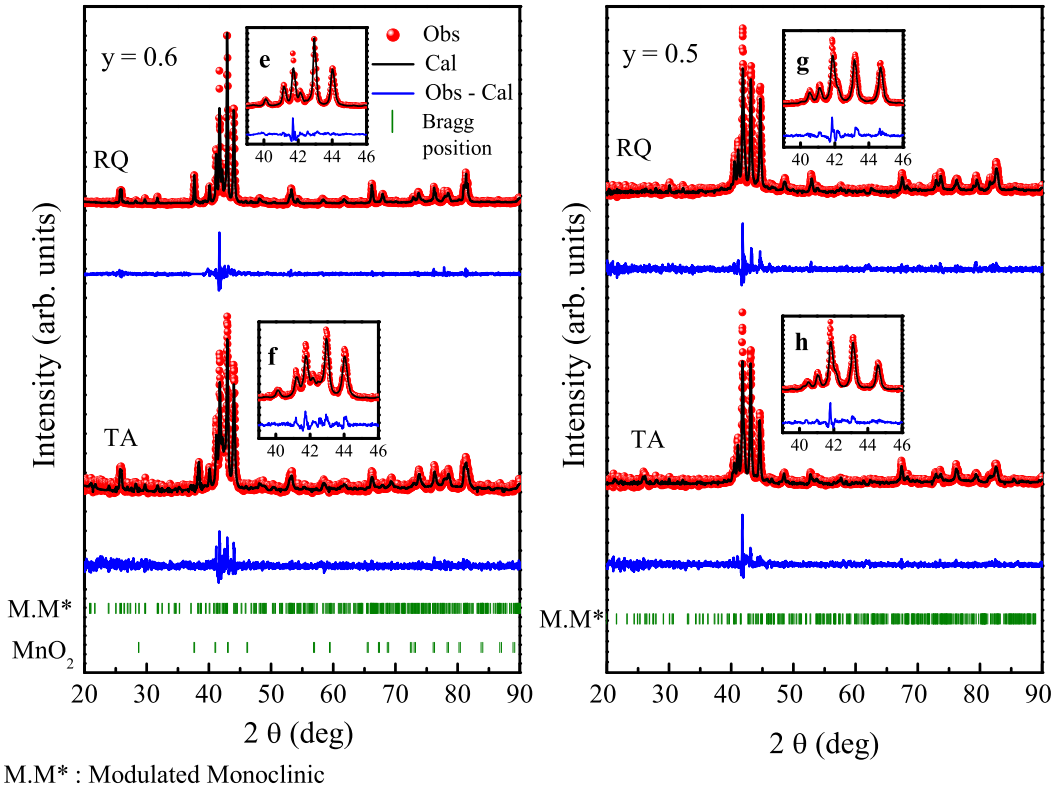

Figure 6.2: X-ray diffraction data for the alloys $y = 0.6$ and $y = 0.5$ at 300 K. The change in the intensity of the major and satellite peaks due to 7M modulations in rapidly quenched (RQ) and temper annealed (TA) $y = 0.6$ (insets (e) and (f) respectively) and as insets g (RQ) and h (TA) in $y = 0.5$.

0.65 wherein both the alloys exhibit cubic Heusler state. Upon temper annealing, even though there is no apparent change in the structure, broadening of the diffraction peaks is noticed. Insets (a) and (b) for $y = 0.68$ and insets (c) and (d) for $y = 0.65$ clearly show the broadening of 220 Bragg reflection in TA alloys. The alloys $y = 0.6$ and $y = 0.5$ presented in Fig. 6.2 show a 7M modulated martensitic structure, which appears to have been retained even after temper annealing. However, a difference in the intensity ratios between the main and satellite peaks is clearly noticed in both the alloys $y = 0.6$ (see insets (e) and (f)) and $y = 0.5$ (see insets (g) and (h)) after temper annealing indicating

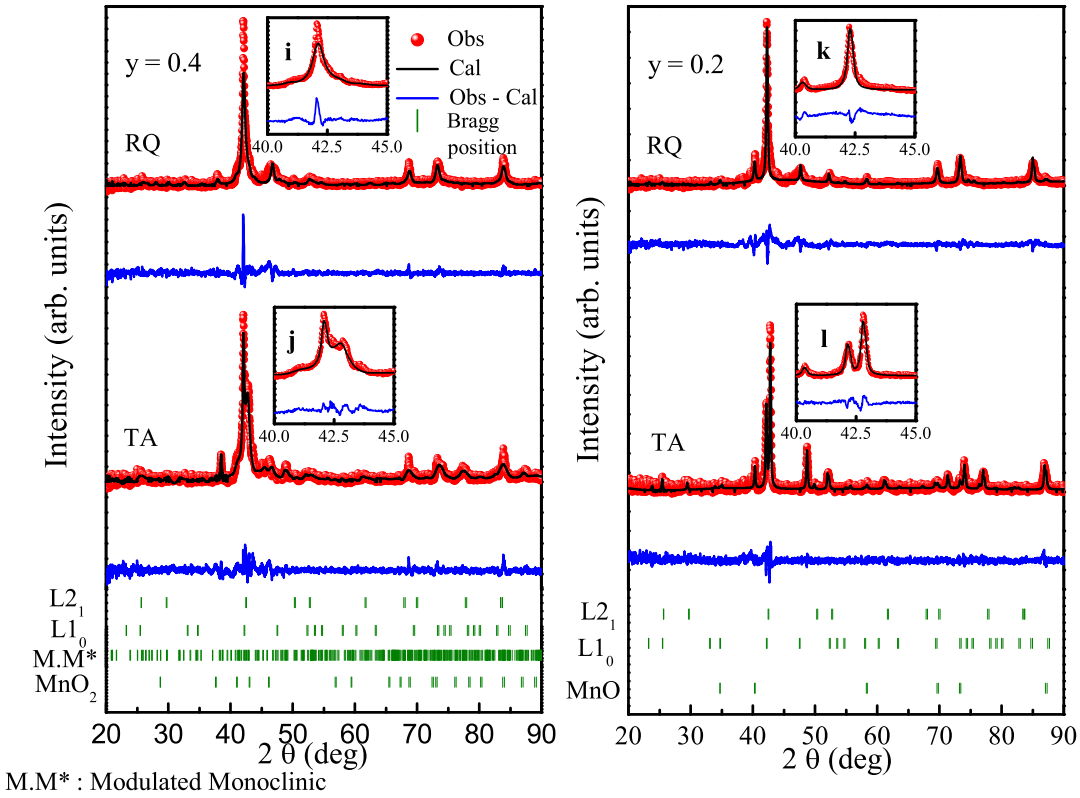

Figure 6.3: X-ray diffraction data for the rapid quenched (RQ) and temper annealed (TA) alloys $y = 0.4$ and $y = 0.2$ at 300 K. The insets features the evolution of phases from $L1_0$ (i) to mixture of $L1_0$, $L2_1$ and 7M phases (j) in the alloy $y = 0.4$ and the transformation of $L1_0$ (k) to mixture of $L1_0$ and $L2_1$ phases (l) in the alloy $y = 0.2$

a change in the modulation or partial disintegration of the alloys. Interestingly, the alloy $y = 0.4$ undergo a transition from the tetragonal $L1_0$ to a mixture of $L1_0$, Heusler $L2_1$, and modulated phases post temper annealing as seen in Fig. 6.3, insets (i) and (j). On the other hand, the alloy $y = 0.2$ completely disintegrates from a pure $L1_0$ phase into 22% Ni_2MnIn and 72% $NiMn_2$ along with a minor 6% MnO phase (Fig. 6.3, inset (l)) after temper annealing. The crystallographic information obtained from the refinement is summarized in Table 6.1.

Table 6.1: The crystallographic data for the rapid quenched (RQ) and temper annealed (TA) alloys in the series $Ni_2Mn_{2-y}In_y$. [a]The shortfall in the sum of percent phase fractions is made up by impurity phases, MnO and MnO_2.

Compositions	**Type**	**Phases**	**Space group**	**Lattice parameters**
$y = 0.68$	RQ[a]	Cubic (99)	$Fm\bar{3}m$	a = 6.01334(5) Å
	TA[a]	Cubic (98)	$Fm\bar{3}m$	a = 6.01925(8) Å
$y = 0.65$	RQ	Cubic (100)	$Fm\bar{3}m$	a = 6.00701(5) Å
	TA	Cubic (100)	$Fm\bar{3}m$	a = 6.0101(2) Å
$y = 0.6$	RQ	7M (100)	$I2/m(\alpha 0\gamma)00$	a = 4.3892(2) Å, b = 5.6424(2) Å, c = 4.3337(1) Å $\beta = 92.91(4)^\circ$, $q = 0.3321(4)$
	TA[a]	7M (99)	$I2/m(\alpha 0\gamma)00$	a = 4.3842(2) Å, b = 5.6414(4) Å, c = 4.3291(3) Å $\beta = 92.88(8)^\circ$, $q = 0.3319(3)$
$y = 0.5$	RQ	7M (100)	$I2/m(\alpha 0\gamma)00$	a = 4.4024(3) Å, b = 5.5470(4) Å, c = 4.3240(2) Å $\beta = 94.226(6)^\circ$, $q = 0.3101(3)$
	TA	7M (100)	$I2/m(\alpha 0\gamma)00$	a = 4.405(3) Å, b = 5.5538(4) Å, c = 4.3281(3) Å $\beta = 94.075(7)^\circ$, $q = 0.3021(2)$
$y = 0.4$	RQ	Tetragonal (100)	P4/mmm	a = 3.862(5) Å, c = 3.468(9) Å
	TA[a]	Tetragonal (54) Cubic (11) 7M (33)	P4/mmm $Fm\bar{3}m$ $I2/m(\alpha 0\gamma)00$	a = 3.736(1) Å, c = 3.514(1) Å a = 6.0694(7) Å a = 4.404(2) Å, b = 5.628(2) Å, c = 4.337(1) Å $\beta = 94.17(2)^\circ$, $q = 0.3347(6)$
$y = 0.2$	RQ	Tetragonal (100)	P4/mmm	a = 3.826(5) Å, c = 3.495(7) Å
	TA[a]	Tetragonal (72) Cubic (22)	P4/mmm $Fm\bar{3}m$	a = 3.7364(2) Å, c = 3.5135(4) Å a = 6.0602(4) Å

6.2.2 Thermal properties

The martensitic transition temperature T_M of the transforming alloy $0.2 \leq y \leq 0.6$ RQ and their TA counterparts were determined through Differential scanning calorimetry (DSC) (273 K $\leq T \leq$ 850 K) and Differential thermal analysis (DTA) (300 K $\leq T \leq$ 1100 K) measurements. The results are presented in Fig. 6.4. The inset shows the DTA plot of the alloy NiMn displaying martensitic transition at around 990 K and $L2_1$ to B_2 ordering transition at around 1032 K. With increase in In content, the expected decrease in the martensitic transition temperature is seen. from the alloy $y = 0$ to $y = 0.6$. Interestingly, none of the TA alloys, from $y = 0.4$ to the completely disintegrated $y = 0.2$, exhibit any significant change in the transformation temperature.

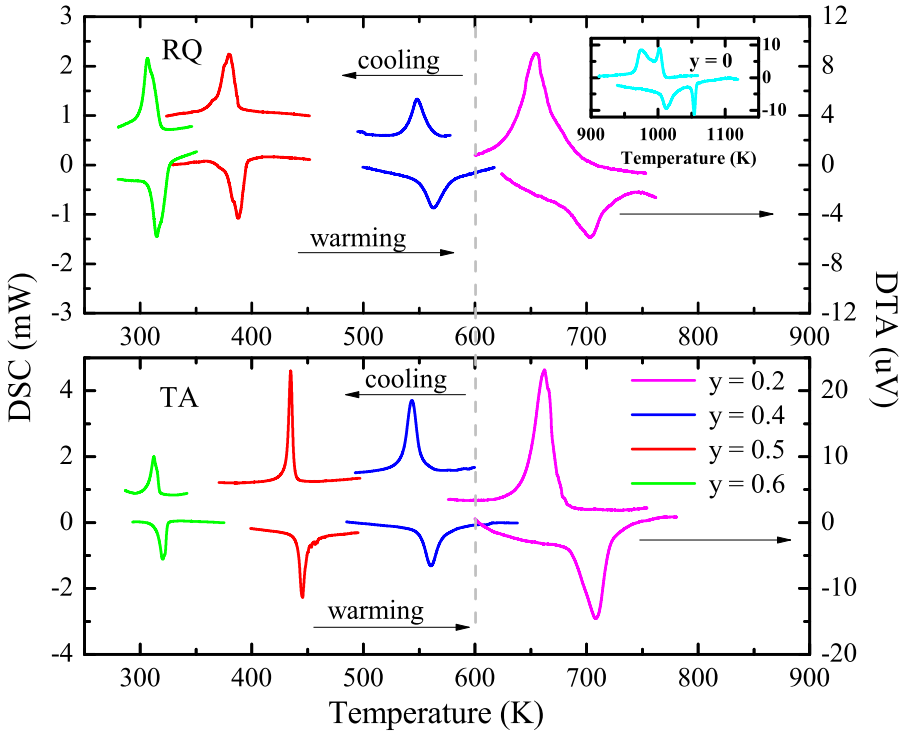

Figure 6.4: The thermo-analytical measurements for the rapid quenched (RQ) and temper annealed (TA) alloys showing DSC and DTA plots as a function of temperature for $0.6 \geq y \geq 0.4$ and $y = 0.2$ respectively. The DTA scan for the alloy $y = 0$ is shown as an inset.

6.2.3 Magnetic properties

Fig. 6.5 depicts the temperature dependent magnetization results for the RQ and TA alloys. Upon temper annealing, an increase in the magnetic moment seen in all the alloy compositions indicating an advancement in ferromagnetism. The RQ alloys $y = 0.68$ and $y = 0.65$ are ferromagnetic with an ordering temperature, $T_C = 310$ K. Post temper annealing, the T_C increases slightly to 320 K in the $y = 0.65$ alloy while it remains nearly constant in the alloy $y = 0.62$. The $y = 0.6$ alloy transforms below 333 K (inset (a) highlights the martensitic transition) with a magnetically glassy ground state comprising of ferromagnetic and antiferromagnetic clusters as observed in chapter 5. The alloy displays

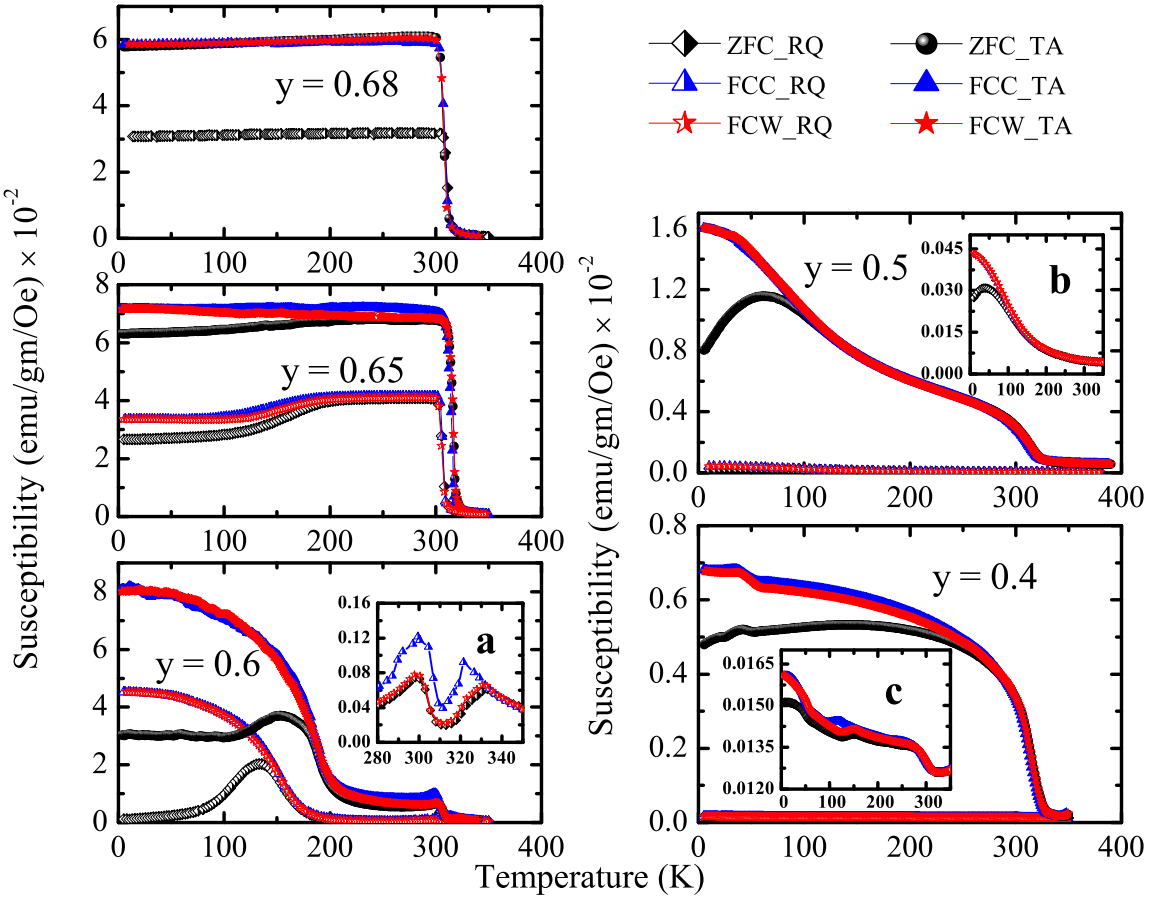

Figure 6.5: Susceptibility as a function of temperature for the rapid quenched (RQ) alloys $0.68 \geq y \geq 0.4$ and their temper annealed (TA) counterparts. Inset (a) features the martensitic transition in the RQ $y = 0.6$ while insets (b) and (c) present the susceptibility curves of RQ $y = 0.5$ and $y = 0.4$ alloys respectively in an amplified scale.

two ferromagnetic transitions at $T_C = 320$ K and $T_C = 200$ K after temper annealing. A complete change of magnetic character is seen in the case of $y = 0.5$ and 0.4. Both the RQ alloys, $y = 0.5$ and 0.4 transform from an antiferromagnetic state (insets (b) and (c) respectively) to a state with dominant ferromagnetic interactions illustrated by a $T_C \sim$ 320 K. An increase in ferromagnetic behavior is an indication of the growth of $L2_1$ phase, which seems apparent in all the TA alloys.

6.2.4 Local structure : EXAFS studies

The experiments so far have shown a varying degree of structural degradation ranging from total phase separation in $y = 0.2$ to only subtle structural changes like an increase in the width of the Bragg peaks ($y = 0.65$ and 0.68) post temper annealing. However, the martensitic transition temperatures remain nearly the same in all the transforming alloy compositions despite the varying degree of structural changes after temper annealing. While an upsurge in ferromagnetic behaviour is seen in all the alloy compositions as evidenced by the magnetization measurements. The strengthening of ferromagnetism could be a signature of the segregation of Ni_2MnIn Heusler phase. However, the nearly invariant martensitic transition temperature, even in a complete phase separated $Ni_2Mn_{1.8}In_{0.2}$ is puzzling. Such a scenario is possible if the decrease in martensitic transition temperature of $Ni_2Mn_{2-y}In_y$ with increasing y is ascribed to the dilution of NiMn entities by Heusler Ni_2MnIn structural units. The progressive replacement of Mn by In in $Ni_2Mn_{2-y}In_y$ results in the formation of Heusler structural entities in the NiMn matrix due to which, a randomly quenched off stoichiometric composition of $Ni_2Mn_{2-y}In_y$ should consist of a random distribution of $L2_1$ (Ni_2MnIn) and $L1_0$ (NiMn) structural units packed within a single crystal structure. Nonetheless, at a local structural level, the presence of two structural entities should be visible. To explore such a possibility, room temperature Ni K and Mn K EXAFS data were analyzed and compared for both RQ and TA alloys of $Ni_2Mn_{2-y}In_y$.

Fig. 6.8 presents the variation of Ni–Mn, Ni–In, Ni–Ni, Mn–In, and Mn–Mn_Z bond

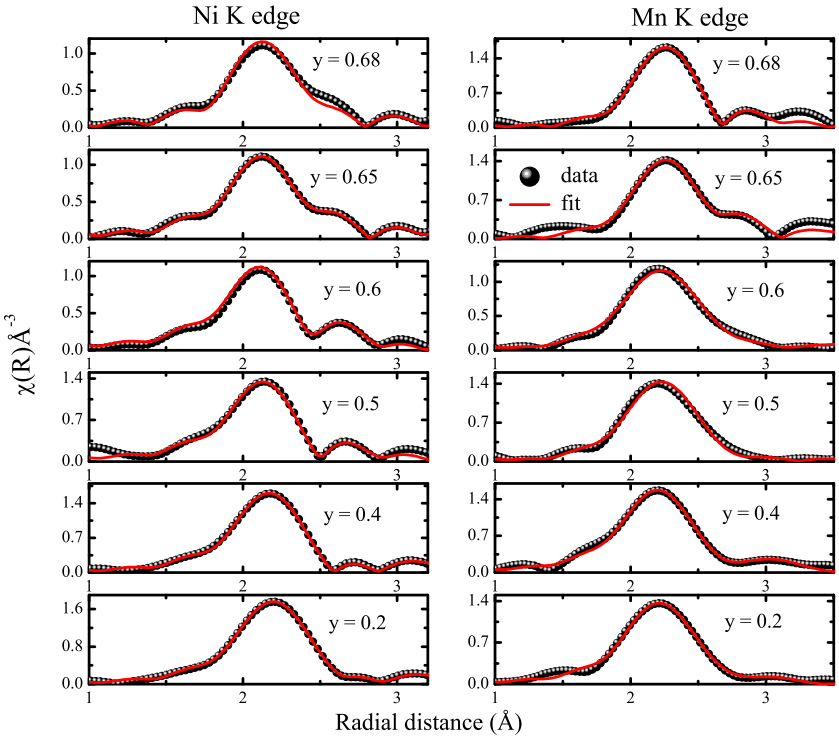

Figure 6.6: The magnitude of Fourier transform spectra at Ni K and Mn K edges in rapid quenched (RQ) alloy compositions in the series $Ni_2Mn_{2-y}In_y$ at 300 K.

distances as a function of In concentration in RQ alloys. With the decreasing In content y, the Ni–Mn and Ni–In bond distances which are otherwise equal in a cubic Heusler structure, deviate away from each other with Ni–Mn bond length being shorter than Ni–In. As y approaches zero, the Ni–Mn distance approaches a value of 2.51 Å , which is equal to Ni–Mn distance in tetragonal NiMn. Further, with the appearance of Mn–Mn_Z bond, the Ni–Ni and Mn–In bond lengths diverge away from their lattice calculated value of 3 Å while the Ni–Ni bond distance increases and eventually splits into two bonds at about $y = 0.5$. The longer Ni–Ni bond increases to 3.51 Å while the shorter Ni–Ni bond converges to 2.61 Å. Both these values of bond distances are equal to Ni–Ni bonds in the tetragonal phase of NiMn. Similar behavior is also exhibited by the Mn–Mn_Z distance.

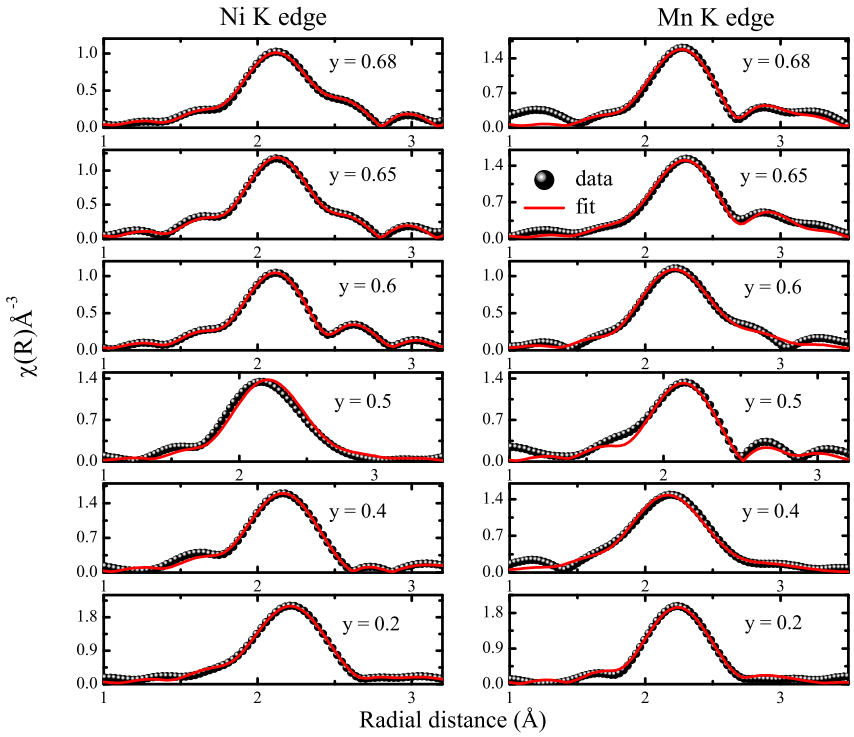

Figure 6.7: The magnitude of Fourier transform spectra at Ni K and Mn K edges in temper annealed (TA) alloy compositions in the series $Ni_2Mn_{2-y}In_y$ at 300 K.

On the other hand, the Mn–In bond distance decreases slowly and saturates at $\sim$ 2.8 Å for $y = 0.2$.

The variation of nearest neighbor Ni–Mn bond distances in the off stoichiometric TA and RQ alloys is compared in Fig. 6.9 (a). There are two Ni–Mn bond distances in TA alloys originating from Ni_2MnIn and NiMn structural units. Their values agree quite well with those calculated from their respective crystal structures. Further, it can be seen that the weighted average of these two Ni–Mn bond lengths nearly equals the Ni–Mn bond length in the RQ alloys. This is an indication of the formation of NiMn and Ni_2MnIn type structural entities in the rapidly quenched off stoichiometric $Ni_2Mn_{2-y}In_y$ alloys.

Fig. 6.9 (b) depicts the comparison of the second nearest neighbor Mn–Mn_Z distance

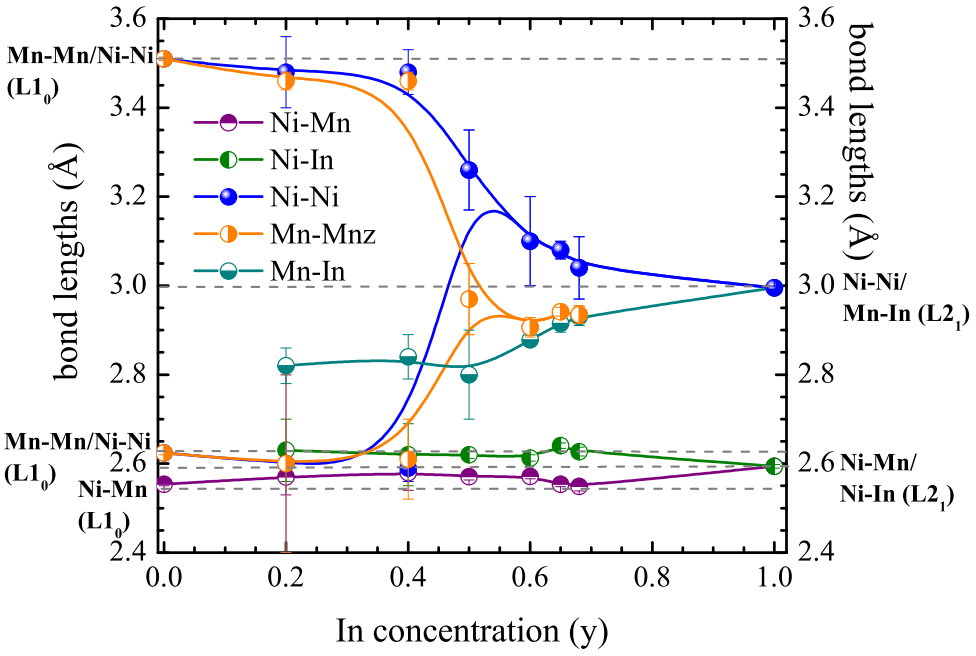

Figure 6.8: Variation of bond lengths with In concentration in rapid quenched (RQ) $Ni_2Mn_{2-y}In_y$.

in the RQ alloys and their TA counterparts. In the RQ alloys, $y \geq 0.65$ which are non-martensitic, Mn–Mn_Z as well as Mn–In and Ni–Ni (see Fig. 6.8) are equal to about 3 Å , which matches with the values obtained from the unit cell parameters. Therefore, in this range $1 > y \geq 0.65$, the structural distortions due to the formation of NiMn and Ni_2MnIn structural entities, are limited only up to the nearest neighbor. After temper annealing, the two Mn–Mn distances also appear to converge towards each other as y increases to 1. For the martensitic RQ alloys $0.6 \geq y > 0.4$ with modulated structure, the Mn–Mn_Z distance increases before splitting into two and eventually matches with Mn–Mn bond distances in the TA alloys for all $y \leq 0.4$. Similar behavior is also observed in the second neighbor Ni–Ni bonds. Interestingly, the average of the two Mn–Mn bond distances in

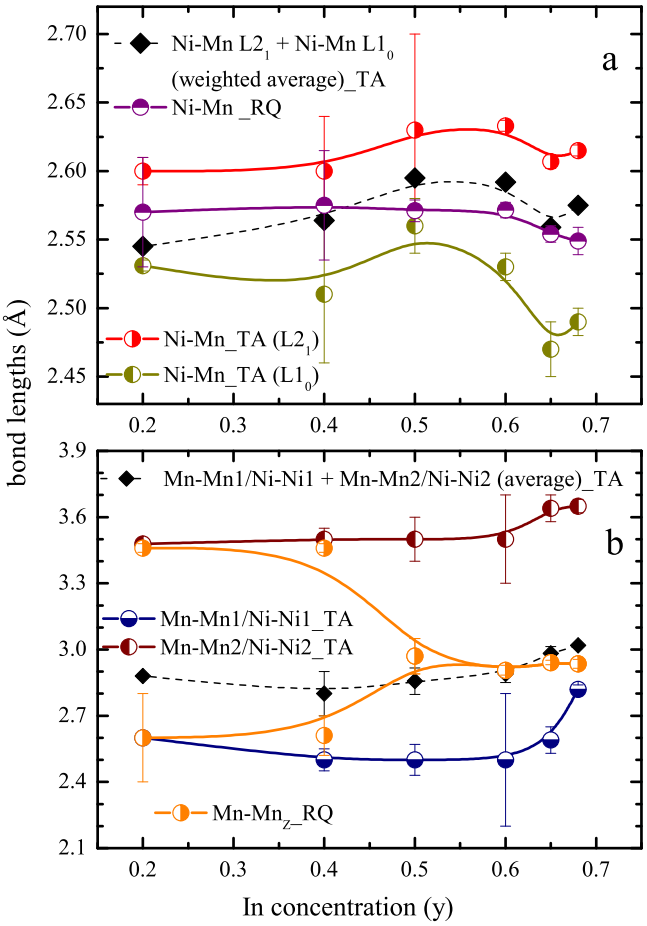

Figure 6.9: Variation of selected nearest neighbor and next nearest neighbor bond lengths with In concentration in rapid quenched (RQ) and temper annealed (TA) $Ni_2Mn_{2-y}In_y$.

the TA alloys is equal to the value of Mn–In distance obtained in RQ alloys right through the series.

6.3 Discussion

Doping of impurity In atoms in the binary NiMn alloy results in a transition from its martensitic $L1_0$ structure to austenitic cubic $L2_1$ Heusler structure. This is associated with the change in magnetic ground state from antiferromagnetic to ferromagnetic. The transformation is achieved beyond critical In concentration of $y = 0.65$ without the ap-

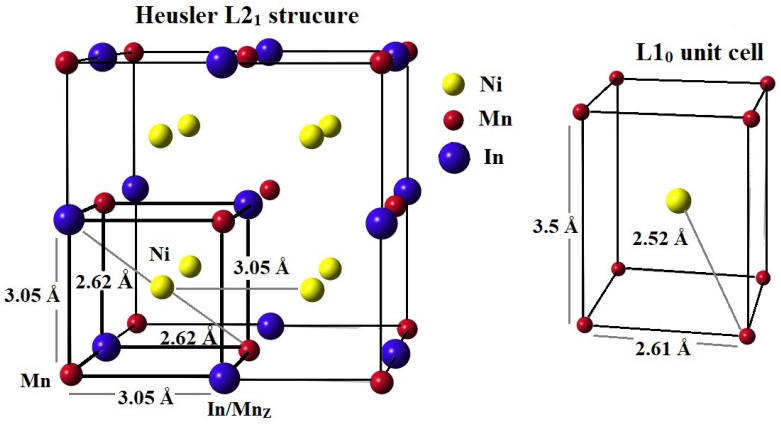

Figure 6.10: The crystallographic model for the $L2_1$ unit cell of Ni_2MnIn and $L1_0$ unit cell of NiMn. The Mn_Z represent the Mn atom in place of In site in the Heusler structure.

pearance of non-ergodic phases like strain glass. The structural transition from $L1_0$ to $L2_1$ occurs via a modulated monoclinic structure. Temper annealing of any of the off stoichiometric compositions of $Ni_2Mn_{2-y}In_y$ is reported to disintegrate into y[Ni_2MnIn] + (1-y)[$(NiMn)_2$].[6]

Fig.6.10 presents the schematic representation of the two structures. The tetragonal $L1_0$ structure consists of nearest neighbor Ni–Mn bond distance of 2.52 Å and next nearest neighbor Ni–Ni/Mn–Mn bond distances at 2.61 Å and 3.51 Å. While, the cubic $L2_1$ superstructure of Ni_2MnIn, formed due to rocksalt type ordering of Mn and In atoms, consists of equidistant Ni–Mn and Ni–In nearest neighbours at $\sim$ 2.6 Å and next nearest Ni–Ni and Mn–In bonds at about 3.0 Å. In $Ni_2Mn_{2-y}In_y$ additional Mn–Mn_Z bonds at about 3 Å develop due to partial occupation of Z sites by Mn and In atoms in X_2YZ Heusler structure.

EXAFS analysis indicate that in all the off-stoichiometric $Ni_2Mn_{2-y}In_y$ alloys, the

bond distance Ni–Mn is always shorter than Ni–In. Furthermore, a comparison of near neighbour bond distances in TA alloys with RQ alloys reveal an interesting trend. From Fig. 6.9 (a), it can be seen that the weighted average of nearest neighbor Ni–Mn distances obtained in the temper annealed alloys nearly equals the Ni–Mn bond distance in RQ alloys. Thus, the shorter Ni–Mn distance as compared to Ni–In the bond distance, observed in all rapidly quenched off stoichiometric compositions is a result of proportionate addition of Ni–Mn distance in Ni_2MnIn and Ni–Mn distance in NiMn. This implies the $L2_1$ and $L1_0$ structural entities develop in all the off stoichiometric RQ alloys. However, the structural distortion is limited to only the nearest neighbour in the RQ alloys $y \geq 0.65$. This is because in these compositions, the phase fraction of $L1_0$ (NiMn) type entities is negligibly small due to which the second neighbour bond distances, Ni–Ni, Mn–In and Mn–Mn_Z are nearly equal, thereby preserving the cubic symmetry of the major Heusler $L2_1$ (Ni_2MnIn) entities.

In the alloys undergoing martensitic transformation ($0.6 \geq y > 0.4$), the extension of structural distortions to the second neighbour bond distances is witnessed illustrating an increase in the amount of $L1_0$ entities. For instance, the bond distances, the Ni–Ni and Mn–Mn_Z deviate away from their crystallographic values and then split into two components, eventually becoming equal to the respective distances in the tetragonal $L1_0$ structure of NiMn. At the same time, the Mn–In bond distance, decreases to 2.8 Å and remains nearly constant with decreasing In content. Likewise, the rapid increase in the ferromagnetic Mn-Mn distance in this region as against in the compositions $y \geq 0.65$, is

associated with the relaxation of strain caused by the replacement of Mn by In in the $L2_1$ structure, thereby leading to the absence of non-ergodic structure like strain glass in these alloys.

Interestingly, the value of Mn–In bond distance tracks the average value of the two Mn–Mn distances obtained for TA alloys. Therefore, it appears that the modulated crystal structure of the martensitic $Ni_2Mn_{2-y}In_y$ alloys is made up of randomly arranged Ni_2MnIn and NiMn type structural entities at a local structural level. The Mn–In bonds act as the bridging bonds compensating for the difference in the near neighbor bond distances of cubic Ni_2MnIn and tetragonal NiMn. Such a random arrangement of Ni_2MnIn and NiMn type structural entities within the crystal structure of the rapidly quenched $Ni_2Mn_{2-y}In_y$ alloys prevents the segregation of a defect phase which supports the absence of the transition from the martensitic ground state to strain glass in these alloys. On the other hand, the same random arrangement of ferromagnetic Ni_2MnIn and antiferromagnetic NiMn structural entities in the rapidly quenched alloys facilitates strongly interacting non-ergodic magnetic ground states like super spin glass. The strong magnetoelastic coupling between the $L2_1$ and $L1_0$ units appears to persist in the temper annealed alloys and is responsible for the invariance of the martensitic transition temperature.

6.4 Conclusion

The present study on rapidly quenched and temper annealed $Ni_2Mn_{2-y}In_y$ alloys reveals the presence of randomly packed Ni_2MnIn and NiMn structural units in all off stoichiomet-

ric rapidly quenched alloys. These units segregate and phase separate into proportionate amounts of $L2_1$ and $L1_0$ phases upon temper annealing. The random arrangement of $L2_1$ and $L1_0$ structural entities within a single crystal structure precludes segregation of point defects and thus prevents the system from exhibiting non-ergodic elastic behavior like strain glass. The strong ferroelastic coupling between the Ni_2MnIn and NiMn structural entities in the rapidly quenched alloys persists even in the phase separated conditions and is responsible for the observed invariance of the martensitic transition temperature.

References

[1] E. Kren, E. Nagy, L. Pal, and P. Szabo. *J. Phys. Chem. Sol.*, 29:101–108, 1968.

[2] A. Çakir, M. Acet, and M. Farle. *Sci. Rep.*, 6:28931, 2016.

[3] T. Krenke, A. Çakir, F. Scheibel, M. Acet, and M. Farle. *J. Appl. Phys.*, 120:243904, 2016.

[4] A. Çakir and M. Acet. *J Magn Magn Mater*, 448:13–18, 2018.

[5] Z. Wanjiku, A. Çakir, F. Scheibel, U. Wiedwald, M. Farle, and M. Acet. *J. Appl. Phys.*, 125:043902, 2019.

[6] A. Çakir, M. Acet, U. Wiedwald, T. Krenke, and M. Farle. *Acta Mater*, 127:117–123, 2017.

[7] P. Entel, M. E. Gruner, S. Fähler, M. Acet, A. Çahır, R. Arróyave, S. Sahoo, T. C. Duong, A. Talapatra, L. Sandratskii, S. Mankowsky, T. Gottschall, O. Gutfleisch, P. Lázpita, V. A. Chernenko, J. M. Barandiaran, V. V. Sokolovskiy, and V. D. Buchelnikov. *Physica Status Solidi (b)*, 255(2):1700296, 2018.

Chapter 7

Summary and Future prospects

7.1 Summary

The present study is aspired with the primary objective of understanding the effect of impurity doping and its implication on the local structure in shape memory alloys. In particular the occurrence of strain phase is investigated in impurity doped martensitic alloys.

To begin with, Ni rich NiTi alloy system is considered to probe the nature of structural defects that are responsible for suppressing the long-range ordering of the elastic strain vector leading to a strain glassy phase. A detail local structural study through EXAFS, suggests the formation and segregation of Ni BCC clusters in Ni rich NiTi alloys within the B19' phase of NiTi. The Ni BCC phase obstructs the propagation of elastic strain vector resulting in glassy ground state. An increase in Ni impurity results in structural change in defect phase from Ni BCC to Ni FCC while the parent NiTi phase retains B19' structure.

Further, the strain glass phase is explored in NiMn based magnetic shape memory alloys. To this effect, two martensitic alloy systems $Ni_2Mn_{1.5}In_{0.5}$ and Ni_2Mn_2 are consid-

ered. In $Ni_2Mn_{1.5}In_{0.5}$, Fe impurity, which is a known suppressant of martensitic transition is doped at the expense of Mn and Ni. Addition of Fe in place of Mn results in the segregation of major Heusler phase and a minor γ (Fe-Ni) phase which acts as an impendent for the long-range ordering of the elastic strain vector there by promoting glassy ground state. Contrary to this, when Fe is substituted for Ni, it replaces Mn in the Y/Z Heusler sublattices forcing Mn to occupy the X sublattice together with Ni. This creates an $A2$ disorder which suppresses the martensitic transition by promoting a ferromagnetic ground state. Thus, strain glass phase appears if the Fe addition facilitates the segregation of an impurity phase. However, if the dopant Fe accommodates in Heusler phase through an antisite disorder, the ferromagnetic interactions become stronger thereby inhibiting the martensitic transition. In Ni_2Mn_2, addition of In atoms at the expense of Mn to realize $Ni_2Mn_{2-y}In_y$ also results in the disappearance of martensitic transition at the critical y concentration of 0.65. With the increase in In content, there is a structural transition from tetragonal $L1_0$ phase to cubic Heusler $L2_1$ phase mediated by modulated monoclinic phase. This is associated with the magnetic ground state transition from antiferromagnetic to a super spin glassy phase with competing ferromagnetic and antiferromagnetic clusters, and finally displaying strong ferromagnetic interactions with the emergence of Heusler phase. The study suggests presence of randomly packed $L2_1$ Ni_2MnIn ($y = 1$) and $L1_0$ Ni_2Mn_2 ($y = 0$) structural units in all off stoichiometric $Ni_2Mn_{2-y}In_y$ alloys. The random arrangement of $L2_1$ and $L1_0$ structural entities within a single crystal structure prevents segregation of point defects which forbids the system from exhibiting non-ergodic

elastic behavior like strain glass.

The present study implies that in a impurity doped martensite, the appearance of strain glass is associated with the presence of defect phase. This is witnessed in $Ni_{50+x}Ti_{50-x}$ wherein Ni BCC phase segregates and in $Ni_2Mn_{1.5-x}Fe_xIn_{0.5}$, it is the $\gamma-$(FeNi) phase appearing as a defect phase. Both these defect phases hinder the propagation of long range ordering of the elastic strain vector thereby achieving a non-ergodic ground state. On the other hand, if the impurity is accommodated in the Heusler structure, point defects are not created and the system does not undergo a glassy dynamics. In $Ni_{2-x}Fe_xMn_{1.5}In_{0.5}$, the Fe atoms are accommodated within the parent structure via an $A2$ type antisite disorder resulting in long-range ferromagnetic interactions. While in the off-stoichiometric $Ni_2Mn_{2-y}In_y$ alloys, the structural entities NiMn and Ni_2MnIn are packed in a single crystal structure, preventing a transition to a non-ergodic state despite impurity addition.

7.2 Future directions

The study concludes that the strain glass appears when impurity segregates as a defect phase. However, the criteria for the impurity to segregate as a defect phase or accommodate within the structure in martensitic alloys still needs to be understood. This could be related to the lattice constant or the symmetry of both the parent and the defect phase. For instance, the defect phase Ni BCC has a lattice constant of 2.82 Åwhich is quite close to its counterpart 2.84 Åof the parent B19' structure. Also, the defect phase is body

centered cubic similar to the austenitic phase of NiTi. However, these observations need further investigation for a more conclusive explanation. Furthermore, the study can be extended to other ferroic glasses. Identification of probable defect phases particularly in spin clusters or relaxor ferroelectrics can be carried out for a more general understanding. Conversely, the possibility of the existence of glass in phase separated ferroic systems can be explored.

Additionally, the doping of Fe in the martensitic $Ni_2Mn_{1.5}In_{0.5}$ needs a further probe. In chapter 4 of this thesis it has been shown that, if Fe is substituted for Mn (Y/Z site of the Heusler), it segregates into a defect $\gamma-$(Fe,Ni) phase. The presence of this defect phase results in the conversion of the martensitic ground state of $Ni_2Mn_{1.5}In_{0.5}$ into a strain glass. Surprisingly, if Fe is doped for Ni (X site of the Heusler), it seems to preferentially occupy the Y/Z sublattice forcing an austenitic ferromagnetic ground state via antisite disorder. Such a paradoxical situation needs further investigation. Substituting Fe for In in $Ni_2Mn_{1+x}In_{1-x}$ also results in an austenitic ferromagnetic ground state.[1] However, when Fe is substituted in the ferromagnetic Ni_2MnIn to realize $Ni_2MnIn_{1-y}Fe_y$, phase separation is noticed. The two separated phases were identified as cubic Heusler and tetragonal D022.[1] These two phases are slightly different from the Heusler and $\gamma-$(Fe,Ni) phases seen in $Ni_2Mn_{1.4}Fe_{0.1}In_{0.5}$. However subtle differences are seen in the x-ray diffraction patterns of tetragonal D022 and FCC $\gamma-$(Fe,Ni) phases, given the fact that the constituent atoms have similar x-ray scattering amplitudes. Hence, a thorough investigation is required in analyzing the two phases in $Ni_2MnIn_{1-y}Fe_y$ while compar-

ing the properties with $Ni_2Mn_{1.5-x}Fe_xIn_{0.5}$. Further, the conditions responsible for phase separation and conversion to ferromagnetic austenitic ground state need to be identified.

In the present study, the effects of impurity doping in Mn rich Ni_2MnZ type Heusler alloys are inspected. Nonetheless, a similar probe on Mn rich Mn_2NiZ type shape memory alloys known as good candidates for spin-torque transfer devices would be intriguing.[2–5] These alloys usually exhibit in stable cubic or tetragonal structure with relatively high Curie temperature with ferrimagnetic ordering.[6] The alloys have inherent antisite disorder due to site preferences of transition metal elements. Studies have shown exchange bias behaviour most likely originating from the glassy nature of the magnetic state at lower temperatures.[7] These aspects can be further investigated by carefully doping impurities and studying the consequences in such alloys.

References

[1] D. N. Lobo, K.R. Priolkar, S. Emura, and A. K. Nigam. *J. Appl. Phys.*, 116:183903, 2014.

[2] T. Graf, C. Felser, and S. S. P. Parkin. *Progress in Solid State Chemistry*, 39:1–50, 2011.

[3] S. Mizukami, A. Sakuma F. Wu, J. Walowski, D. Watanabe, T. Kubota, X. Zhang, H. Naganuma, M. Oogane, Y. Ando, and T. Miyazaki. *Phys. Rev. Lett.*, 106:117201, 2011.

[4] J. Winterlik, B. Balke, G. H. Fecher, C. Felser, M. C. M. Alves, F. Bernardi, and J. Morais. *Phys. Rev. B*, 77:054406, 2008.

[5] H. Kurt, K. Rode, M. Venkatesan, P. S. Stamenov, and J. M. D. Coey. *Phys. Rev. B*, 83:020405, 2011.

[6] B. Balke, G. H. Fecher, J. Winterlik, and C. Felser. *Appl.Phys. Lett.*, 90:152504, 2007.

[7] A. K. Nayak, C. Shekhar, J. Winterlik, A. Gupta, and C. Felser. *Appl. Phys. Lett.*, 100:152404, 2012.

Publications

Journals

1. R. Nevgi and K. R. Priolkar, *Appl. Phy. Lett* 112, 022409 (2018), Unusual strain glassy phase in Fe doped $Ni_2Mn_{1.5}In_{0.5}$

2. R. Nevgi, K. R. Priolkar, Gangadhar Das and M. Acet, *J. Alloys Compd* 797 995-1001 (2019), Importance of site occupancy and absence of strain glassy phase in $Ni_{2-x}Fe_xMn_{1.5}In_{0.5}$

3. R. Nevgi, K. R. Priolkar, L. Righi, M. Solzi, F. Cugini, E. T. Dias and A. K. Nigam, *J. Phys:Condens. Matter*, 32, 505801, (2020), Lattice strain accommodation and absence of pre-transition phases in $Ni_{50}Mn_{25+x}In_{25-x}$

4. R. Nevgi, K. R. Priolkar, Simone Pollastri and Giuliana Aquilanti, *Phys. Rev. B*, 103, 064108 (2021),Structural defects responsible for strain glassy transition in $Ni_{50+x}Ti_{50-x}$

5. R. Nevgi, K. R. Priolkar and M. Acet, *J Phys D: Appl Phys*, 54, 185002 (2021), Strain glass versus antisite disorder induced ferromagnetic state in Fe doped Ni-Mn-In Heusler martensites

6. R. Nevgi, E. T. Dias and K. R. Priolkar, *Phys. Rev. B*, 104,054101 (2021), Randomly packed Ni_2MnIn and NiMn structural units in off-stoichiometric $Ni_2Mn_{2-y}In_y$ alloys

7. K. R. Priolkar, R. Nevgi, E. T. Dias and A. K. Nigam, *Sci. Rep.*, 11, 19588 (2021), Kinetic arrest of the ferromagnetic state in Mn_3GaC and Ni_2MnGa composite mixtures

Conference Proceedings

1. R. Nevgi, K. R, Priolkar, and L. Righi, *AIP Conf Proc.* 1942, 030016, (2018), Investigation of route to martensitic transition in Ni-Mn-In shape memory alloys

Conferences/Workshops attended

1. 62^{nd} Department of Atomic Energy (DAE) Solid State Physics Symposium, BARC-Mumbai, 2017, Investigation of route to martensitic transition in Ni-Mn-In shape memory alloys (poster presentation).

2. National Conference On Electronic Structure (NCES), SRM Institute - Chennai, 2018, Unusual ground states in Fe doped Ni-Mn-In magnetic Shape Memory alloys (poster presentation).

3. Indo-Italian workshop on 'Accelerator based photon sources as a versatile tool to probe matter: Present scope and outlook' , IISc– Bengaluru, 2018.

4. Indo – Portuguese two day workshop on Material Science , Goa University, 2019, Is strain glass phase a requisite in martensite ? (poster presentation).

5. Symposium on 'Recent Trends in Condensed Matter Physics and Materials Science' , Goa University, 2020, Lattice strain accommodation and absence of pre-transition

phases in Mn doped Ni_2MnIn (poster presentation).